# Atomic Force Microscopy investigations of fiber-fiber bonds in paper

by
Dipl.-Ing. Franz J. Schmied
submitted in fulfillment of the requirements for the degree of
**Doktor der montanistischen Wissenschaften**
at the Institute of Physics
University of Leoben, Austria

under supervision of
Ao. Univ. Prof. Dr. Christian Teichert

refereed by
Ao. Univ. Prof. Dr. Christian Teichert
and
Ao. Univ. Prof. Dr. Robert Schennach

Leoben, March 2011

*dedicated to my family*

# Eidesstattliche Erklärung

The author attests that permission has been obtained for the use of any copyrighted material appearing in this thesis (other than brief excerpts requiring only proper acknowledgment in scholarly writing) and that all such use is clearly acknowledged.

Ich erkläre hiermit, dass ich die vorliegende Arbeit selbst verfasst habe. Außer den angeführten wurden keine Hilfsmittel und Quellen verwendet. Stellen, die aus anderen Arbeiten übernommen wurden, sind als solche gekennzeichnet.

*Dipl.-Ing. Franz J. Schmied*
Leoben, March 2011

# Abstract

Paper is one of the most versatile materials accompanying mankind during history, either used for delivering and storing of information as well as to protect food and other goods from the environment. In this thesis, the main focus was put on the investigation of cellulose fibers for kraft paper. Cement bags, for instance, need a high tear strength and a high porosity simultaneously to allow a quick filling in the production line.

A comprehensive surface morphology analysis based on atomic force microscopy (AFM) was performed to characterize the individual surface features of single fibers. High-resolution phase images were recorded which revealed the microfibrilliar structure of the fibers. Depending on the cell wall layer, different orientation and ordering of the microfibrils - having diameters of 25 to 35 nm - was visualized. Additionally, a detailed analysis of lignin precipitates based on a watershed algorithm as a function of the so called $\kappa$-number was performed.

To gain further insight into the contact area of two bonded single fibers, cross-sectional samples were investigated. Here, single fibers, fiber-fiber bonds and embedded paper sheets are explored in detail. The individual cell wall layers (P, S1-S3) are visualized and their thickness was determined. Further, the change in orientation of the microfibrils with respect to the main fiber axis from perpendicular to parallel is demonstrated.

The main part of the thesis is focused on the development of a method to measure the joint strength of two bonded single fibers based on AFM. Here, a calibrated cantilever was used to apply defined loads into the bonded area. To determine the energy contributions, experiments were performed in a load and a displacement controlled fashion. That allows the determination of elastic (90%) and visco-elastic (1%) energy parts of the total energy input ($10^{-11} - 10^{-12} kJ$). The resulting bonding energy is about $10^{-12} - 10^{-13} kJ$. Additionally to the bonding energy, the breaking behavior prior to the failure based on different bonding mechanisms was analyzed in detail. Here, force discontinuities are strong hints for mechanical interlocking or fibril bridges. Analysis of the force drops revealed different force regimes for rupturing of single cellulose fibrils, fiber wall delamination, and breaking of microfibril bundles.

Besides the measurement of the joint strength, stitched AFM topography reconstructions of the formerly bonded area (FBA) were analyzed. A clear difference between the formerly bonded and unbonded region is recognizable. The formerly bonded area is smoother (Wenzel ratio: 1.07) in comparison to the unbonded area (Wenzel ratio: 1.20). In addition to the roughness difference, dangling fibrils are detected in the FBA, especially localized close to the transition between formerly bonded and unbonded regions. This unique combination of joint strength measurement and AFM based inspection of the FBA further supports the assumption that mechanical interlocks and fibrillar bridges are important contributions to the bonding strength.

# Kurzfassung

Papier ist eines der vielfältigsten Materialien, die die Menschheit begleiten, sei es als Schreib- oder Verpackungsmaterial. Im Rahmen dieser Dissertation wurde der Schwerpunkt der Untersuchung auf Zellulosefasern für Kraftpapier gelegt. Zementsäcke, als Beispiel, sollen einerseits eine hohe Reißfestigkeit besitzen und andererseits eine hohe Porosität aufweisen, um eine schnelle Befüllung zu ermöglichen.

Zunächst wurde eine umfassende Morphologieanalyse von Einzelfaseroberflächen mit Hilfe der Rasterkraftmikroskopie (AFM) durchgeführt und die einzelnen Oberflächenmerkmale charakterisiert. Es ist gelungen, hochauflösende Phasenbilder zu messen und die Mikrofibrillenstruktur abzubilden. Je nach Zellwand zeigt sich eine eindeutige Orientierung und Ordnung mit einem mittleren Fibrillendurchmesser zwischen 25 und 35 nm. Zusätzlich wurde eine detailierte Analyse von Ligninpräzipitaten mit Hilfe eines Watershed-Algorithmus, in Abhängigkeit der sogenannten Kappa-Zahl, durchgeführt.

Um mehr über die Kontaktfläche zwischen zwei gebundenen Einzelfasern in Erfahrung zu bringen, wurden Querschnittsproben genauer untersucht. Hier wurden neben Einzelfaserquerschnitten, eingebettete Faserbindungen und Papier untersucht. Die einzelnen Zellwände (P, S1-S3) konnten aufgelöst und deren Dicke vermessen werden. Auch die Änderung des Fibrillenwinkels von normal auf parallel zur Faserachse wurde visualisiert.

Das Hauptaugenmerk dieser Arbeit lag auf der Entwicklung einer Methode zur Messung der Bindekraft zwischen zwei gebundenen Einzelfasern auf Basis der AFM-Methode. Hierfür wurde ein kalibrierter Biegebalken verwendet, um definiert Last in die Bindefläche bis zum Bruch einzubringen. Um die Energieanteile näher zu bestimmen, wurden sowohl weg- als auch kraftkontrollierte Experimente durchgeführt. Dies erlaubte die Bestimmung des elastischen (90%) als auch des visko-elastischen (1%) Energieanteils der gesamten eingebrachten Energie ($10^{-11} - 10^{-12} kJ$) und liefert eine Bindungsenergie von $10^{-12} - 10^{-13} kJ$. Zusätzlich zur Bindungsenergie wurde das Bruchverhalten bezüglich der Bindungsmechanismen analysiert. Auffällig waren hier vor allem Kraftdiskontinuitäten, die auf mechanische Verhakungen oder fibrilare Brücken hinweisen. Eine Analyse der Kraftsprünge zeigte für den Bruch von Einzelfibrillen, die Zellwanddelamination und den Bruch von Mikrofibrillenbündeln unterschiedliche Kraftbereiche.

Neben der Kraftmessung wurde die mit AFM vermessene Rekonstruktion der Bruchfläche näher analysiert. Hier zeigte sich ein deutlicher Unterschied zwischen der vormals gebundenen Fläche und dem ungebundenen Bereich. Der vormals gebundene Bereich ist glatter (Wenzelverhältnis: 1.07) als der ungebundene Bereich (Wenzelverhältnis: 1.20). Neben den Rauhigkeitsunterschieden befinden sich in der formals gebundenen Fläche freistehende Mikrofibrillen, die besonders im Übergangsbereich zwischen vormals gebunden und ungebunden Bereichen lokalisiert sind. Diese einzigartige Kombination von

Bindekraftmessung und AFM-gestützte Inspektion der Bindefläche stärkt weiters die Annahme, das mechanische Verhakungen und fibrilare Brücken einen wichtigen Beitrag zur Bindung liefern.

# Acronyms

| | |
|---|---|
| κ-number | Kappa number |
| AFM | Atomic Force Microscopy |
| CPD | Contact Potential Difference |
| CSF | Canadian Standard Freeness |
| DeflInvOLS | Deflection Invers Optical Lever Sensitivity |
| DP | Degree of polymerisation |
| ESCA | Electron Spectroscopy for Chemical Analysis |
| ESEM | Environmental Scanning Electron Microscopy |
| FBA | Formerly bonded area |
| FFT | Fast-Fourier Transformation |
| FTIR | Fourier Transform Infrared Spectroscopy |
| Fx | Force-versus-distance |
| KPFM | Kelvin Probe Force Microscopy |
| L | Lumen |
| MFA | Microfibrillar angle |
| OM | Optical Microscopy |
| P | Primary wall |
| PLM | Polarized Light Microscopy |
| PTFE | Polytetrafluoroethylene |
| S1 | Secondary wall number one |
| S2 | Secondary wall number two |
| S3 | Secondary wall number three |

| | |
|---|---|
| SEM | Scanning Electron Microscopy |
| SR | Schopper-Riegler |
| TERS | Tip-Enhanced Raman Spectroscopy |
| ToF-SIMS | Time-of-Flight Secondary Ion Mass-Spectroscopy |
| WR | Wenzel ratio |
| WRV | Water Retention Value |
| XPS | X-ray Photoelectron Spectroscopy |

# Contents

# 1 Motivation

## 1.1 Christian Doppler Laboratory

The scientific investigations of this thesis have been performed within the Christian Doppler Laboratory (CDL) for *Surface Chemical and Physical Fundamentals of Paper Strength* which started in 2007 as a collaboration between three university institutes: (i) Institute of Solid State Physics **(Graz University of Technology)**, (ii) Institute for Paper, Pulp and Fiber Productions **(Graz University of Technology)**, and (iii) Institute of Physics **(Montanuniversität Leoben)** and the industrial partner Mondi **(Frantschach)**. Figure 1.1 visualizes the individual tasks of the participating groups and their joint synergy to investigate the fiber-fiber bond strength.

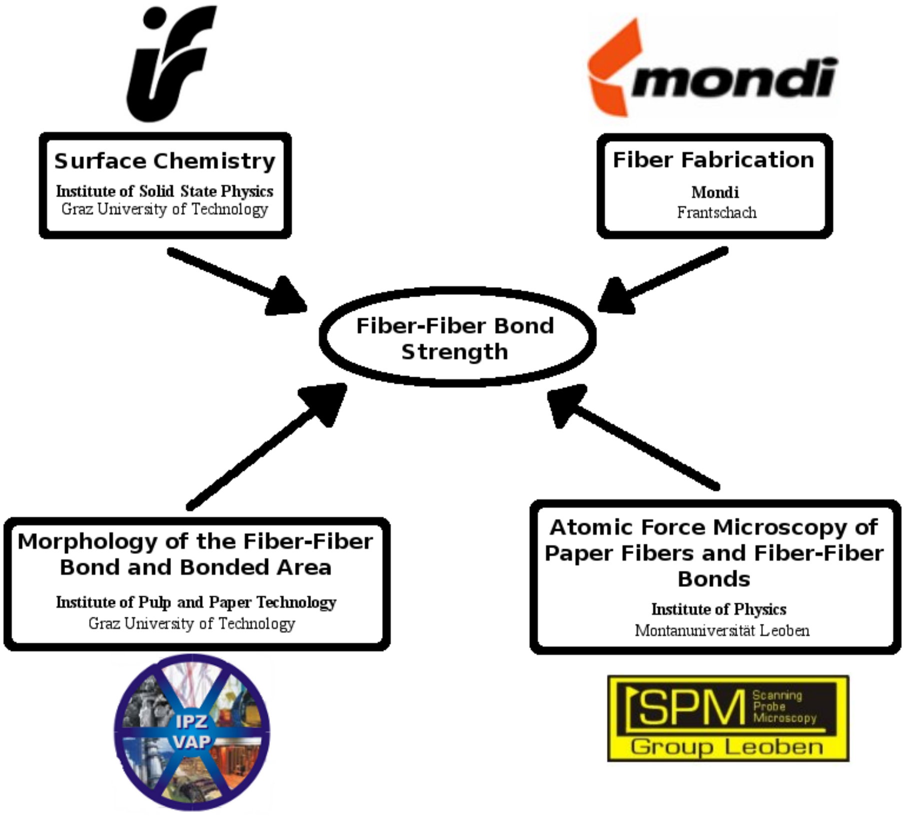

**Figure 1.1:** Distribution of responsibilities within the Christian Doppler Laboratory for *Surface Chemical and Physical Fundamentals of Paper Strength.*

The Institute of Solid State Physics is responsible for chemical analysis of paper fibers using Fourier Transform Infrared Spectroscopy (FTIR). Long term knowledge on paper fabrication and on performing standard paper tests and determination of bonded areas with different techniques - Ultramicrotomy and Polarized Light Microscopy (PLM) are provided by the Institute for Paper, Pulp and Fiber Productions. Beside these two institutes situated in Graz, the Scanning Probe Microscopy group of the Institute of Physics in Leoben is responsible for comprehensive Atomic Force Microscopy (AFM) analysis. Here, the morphology of individual pulp fibers and the difference to the bonded area are investigated as a function of fiber fabrication. Further, an AFM based technique has been developed to quantify the force to separate two bonded fibers. A great advantage of the CDL is the broad approach towards the topic from different points of view and the knowledge flow between the individual institutes. Mondi as industrial partner and initiator of the CDL took responsibility of the applied research part and provided the pulp under investigation.

## 1.2 Why investigating paper on the nanometer scale?

Paper is one of the most versatile materials in human society. It is used for delivering and storing information as well as to protect food and other goods from environmental hazards. Although paper has already been known for more than 2000 years, there are still issues to be solved.

**Figure 1.2:** Collection of different packaging paper products.

Nowadays, paper is made up of wood fibers. These natural fibers consist of three main constituents: cellulose, hemicellulose, and lignin. In natural fibers, the cellulose configuration is cellulose type I, whereas in regenerated fibers a cellulose type II configuration is present. Cellulose microfibrils in a hemicellulose matrix build up a hierarchical structure in different layers to form a single pulp fiber. During the production cycle of a paper machine, these single pulp fibers need to approach close enough, to form a bond between each other and to build finally a complete fiber network. To form a strong sheet of paper it is possible to increase the amount of bonds, which leads to a less porous sheet. For example, cement bags, as they are fabricated by the industrial partner (see figure 1.2), need on the one hand strong sheets with - on the other hand - a high porosity to fill them fast in the factory. Therefore, it is necessary to increase the strength of the fiber-fiber bond itself. A closer look into the fundamentals is desirable in order to understand the basic principles behind paper strength. Until today it is not fully clear what are the dominating mechanisms that lead to fiber-fiber bonding in paper or if the interplay of several mechanisms is important. Here, nanometer scale investigations, like AFM and its derivatives, provide new insights into the problematic to find new approaches.

## 1.3 Outline of this thesis

The thesis will start with an introduction to native cellulose fibers and the difference between wood and pulp fibers. Further, different paper tests and index numbers important for the presented work will be introduced. Then, bond formation, embedding for cross-sectional investigation and mounting on the sample holder for force measurements will be discussed. Right after, the AFM principle is explained, followed by a description of the developed AFM based technique to measure fiber-fiber bond strength and image analytical evaluation.

In the main part, first, the results of fiber surface morphology and the evaluation of the true surface area will be described. Second, cross-sectional investigations with various AFM techniques on single fibers, fiber-fiber bonds, and embedded sheets are presented. Third, results of the fiber-fiber bond strength measurements are discussed. The versatile tool allows statically and dynamically loading of the fiber-fiber bond to separate elastical and visco-elastical energy contributions. The determination of the failure behavior and the necessary load are recorded and correlated to reconstructions of the formerly bonded area. The unique combination of this comprehensive study revealed new insights into the binding mechanisms of a single fiber-fiber bond.

# 2 Background

## 2.1 Paper fibers

The main components of a paper fiber are cellulose, hemicellulose and lignin. Cellulose is a hydrophilic organic compound with the formula $(C_6H_{10}O_5)_n$, a polysaccharide of a linear chain of several thousand linked $\beta$-D-glucose units [1, 2]. A combination of two cellulose molecules - the repeating unit - cellobiose is presented in Figure 2.1 with a length of 1.04 nm [3]. Wood cellulose has an average degree of polymerisation (DP) of approximately 10000, which would correspond to a linear chain length of 5 $\mu$m.

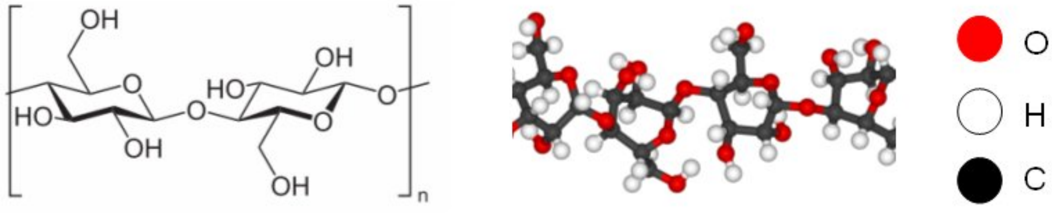

**Figure 2.1:** Cellobiose unit (left) and 3D view of a fraction of a cellulose chain (right). (From [4].)

Hemicellulose (HC) is a slightly branched heteropolysaccharide with a DP of 100-200. Due to a higher amount of -OH groups the molecule is more hydrophilic than cellulose. Important HCs in softwood are galactoglucomannan, arabinoglucuronoxylan, and arabinogalactan [2].

Lignin is an amorphous, highly complex, mainly aromatic polymer of phenyl-propane units. A mechanical pulp contains quite a high amount of lignin, whereas in a chemical pulp the lignin is dissolved from the pulp. Lignin is also the reason why a newspaper is yellowing in the sun whereas a book page does not. Table 2.1 collects an overview of important material properties of these main constituents.

The cellulose chains are glued together in a hemicellulose matrix and form cellulose microfibrils. Together, they build up the fiber wall structure [5]. Figure 2.2 illustrates an overview of the individual cell wall layers in a pulp fiber. In a living plant, the single cellulose fibers are connected with a lignin rich lamella - the middle lamella (M). Next to this lamella is the primary wall (P) with microfibrils randomly oriented. The next

| | degree of polymerization | hydrophilicity |
|---|---|---|
| Cellulose | 10000 | + |
| Hemicellulose | 100 | ++ |
| Lignin | - | - |

**Table 2.1:** Material's properties of the constituents of paper. (From [2].)

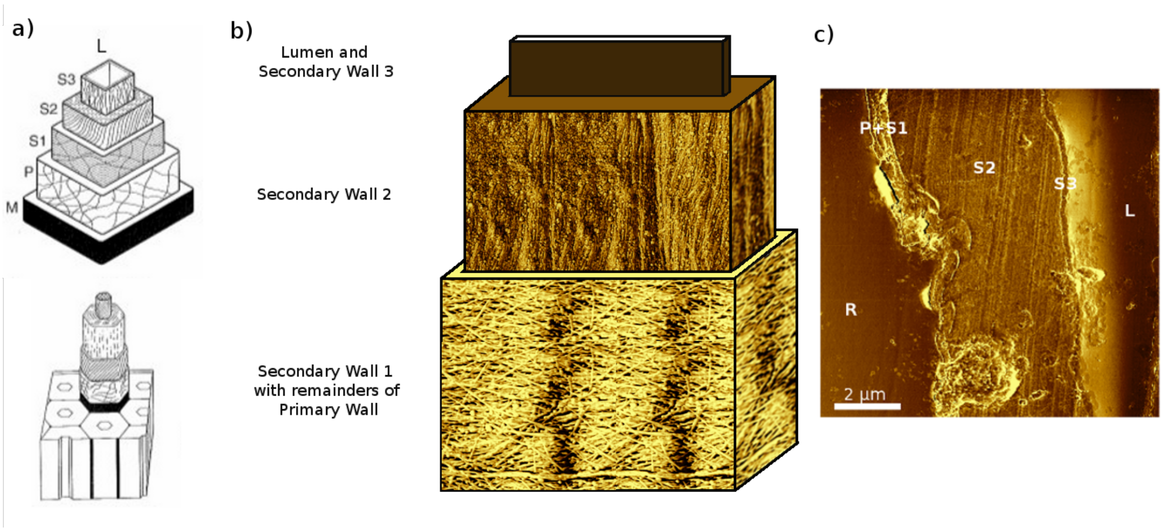

**Figure 2.2:** Different cell wall layers of native cellulose fibers, M - middle lamella, P - primary wall, S1 - secondary wall 1, S2 - secondary wall 2, S3 - secondary wall 3, L - lumen, R - resin. a) Scheme of a wood fiber, b) structure obtained from AFM images, and c) cross-sectional AFM image of an individual pulp fiber.

layer is the secondary wall (S). This layer is sectioned in three sublayers depending on the angle of the cellulose fibrils towards the main fiber axis - the microfibrillar angle (MFA) - and on the fibrils' ordering. The secondary wall number one (S1) reveals fibrils mainly oriented perpendicular to the fiber axis. In the secondary wall number two (S2), the ordering of the fibrils is increasing and the orientation is almost parallel to the fiber axis. The secondary wall number three (S3) is identical to the S1 layer, it represents the finishing to the lumen. The lumen is necessary for the water and nutrients transport in the living cell. Figure 2.2a represents the scheme of this well accepted composition of a wood fiber. In figure 2.2b the true structure of S1 and S2 is indicated by AFM phase images, recorded by the author in the course of the thesis. Figure 2.2c finally visualizes the layer structure by an AFM phase image recorded from a cross-sectional sample of an industrial pulp fiber.

Due to the fact that wood is the raw material for pulp, the cell wall chemistry and assembly is similar for both materials. In a wood cell, the individual fibers are held together with the lignin rich middle lamella and the lumen is intact. For an ideal pulp fiber, the lignin is removed to a minimum without already dissolving the hemicellulose. In contrast to a wood cellulose fiber, the lumen of the pulp fiber is collapsed after the pulping process and forms a flat tube. The exchange of nutrients and water from one fiber to another is realized via joints - called pits - connecting two fibers.

Figure 2.3 presents the chemical composition of the fiber cell wall. Here, the distribution of the main constituents within the individual layers is described and represents the decrease of lignin from the middle lamella to the S3, whereas the amount of cellulose and hemicellulose increases.

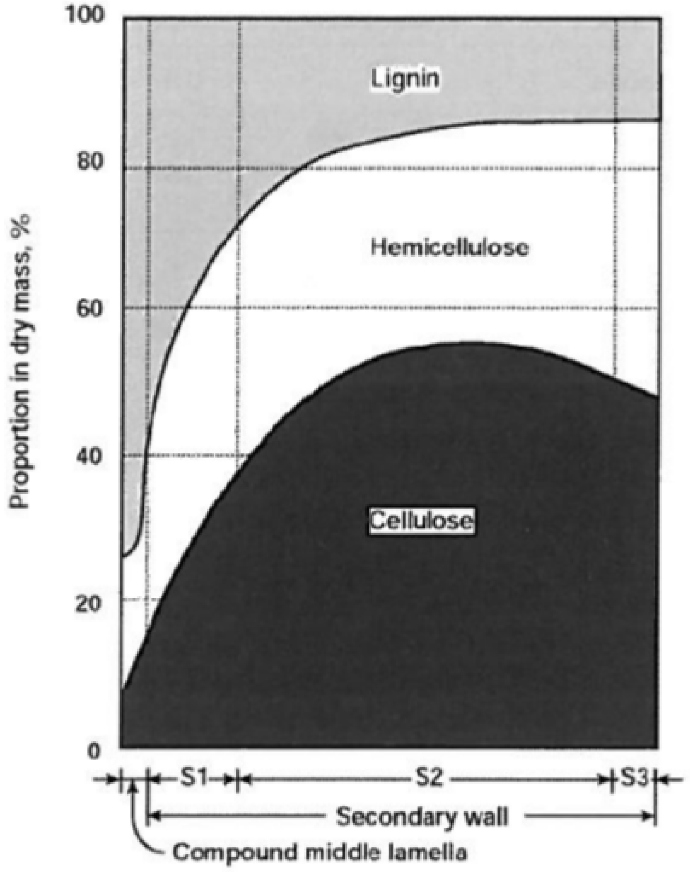

**Figure 2.3:** Material's distribution within the individual cell wall layers. (From [6].)

## 2.2 Fiber-fiber bonding

A key issue in paper production is the mechanism of fiber-fiber bonding. There have been several mechanisms suggested to play a significant role in forming fiber-fiber bonds which finally lead to a fiber network which is called paper. As a prerequisite for paper formation during drying, two fibers need to approach each other close enough to form a bond between them. In this first state, water binds the fibers together by pure surface tension [7]. After removal of the water, other mechanisms are necessary to hold these two fibers further together. Nanko and Ohsawa investigated bonded areas with Scanning Electron Microscopy (SEM) and formulated the following structural mechanisms [8]: (i) bonding layer, (ii) wrinkles, (iii) skirt, and (iv) covering layer, which are illustrated in figure 2.4. Lindström et al. proposed the following five bonding mechanisms [9]: (i) mechanical interlocking, (ii) hydrogen bonding, (iii) electrostatic interactions, (iv) interdiffusion, and (v) induced dipoles. Figure 2.5 presents a schematic overview on these bonding mechanisms.

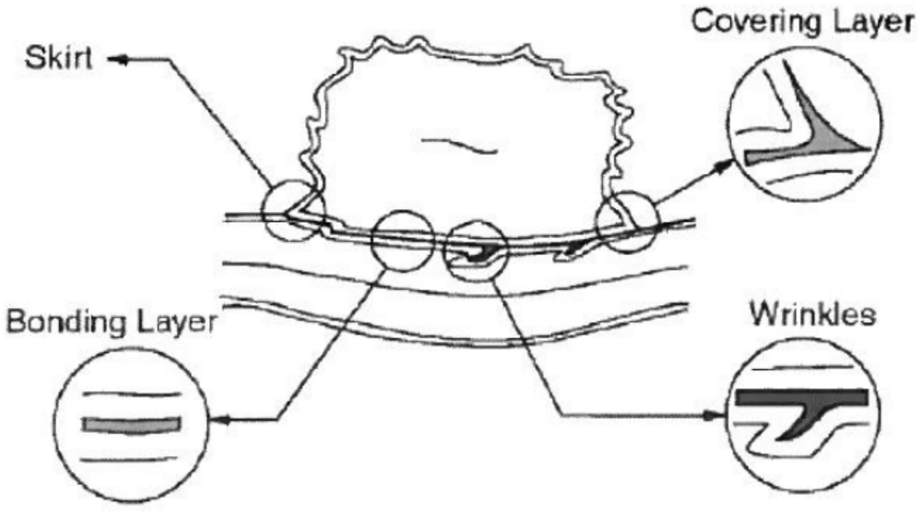

**Figure 2.4:** Structural features of fiber-fiber bonds. (From [8].)

To gain further insight into bonding mechanisms, methods are required to determine the bond strength of fiber-fiber bonds. With these data an attempt can be made to estimate which of the above mentioned bonding mechanisms is the most important. Most of the measurements of fiber-fiber bond strength deal with a setup similar to the one described by Stratton et al. [10], presented in figure 2.6. Here, a fiber-fiber bond is mounted with glue on a support with a slot not completely opened. After curing of the glue, the slot is completely opened, the two fibers are separated, and the force is measured.

Several investigations on differently treated pulp dealt with such a basic setup [11–14]. Table 2.4 provides an overview on joint strength measurements of unbleached, unrefined pulp. So far fiber-fiber bond investigations (see table 2.4) dealt with shear stresses. This approach is considered to be a mode II (in-plane sliding mode) load (see figure 2.7 [15]). A test procedure to investigate fiber-fiber bond failure close to a mode I (tensile opening mode) load would be desirable to gain access to new data. Beside new insights, a comparison with a macroscopical z-direction strength test (see section 2.4.4) is possible. Therefore, the z-direction strength and the amount of bonds need to be known in order to calculate a specific bond strength.

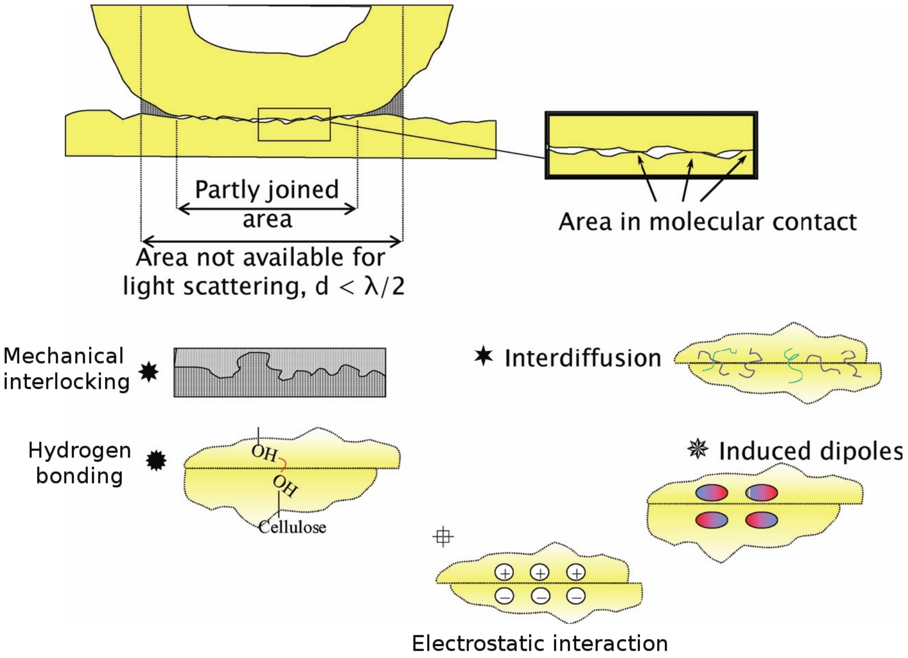

**Figure 2.5:** Suggested bonding mechanisms. (After [9].)

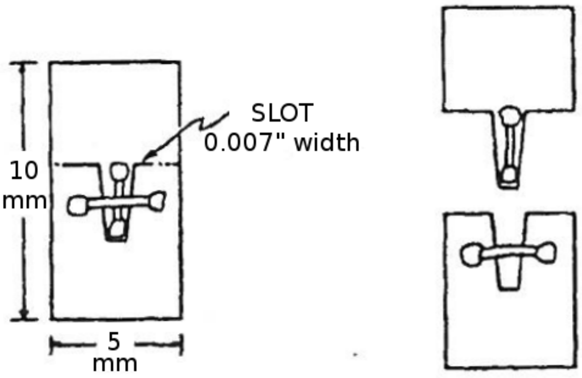

**Figure 2.6:** Mylar bonded fiber mount. (From [10].)

## 2.3 Paper production

This section describes roughly the individual stages in a paper machine, starting from the wet pulp to the final product - a dry sheet of paper. First of all, the wet pulp is placed on a wire mesh through a slicer - a rectangular opening with varying height. The speed between the jet and the wire is called jet-to-wire speed and has influence on several paper properties and determines the anisotropy of the paper. On the mesh, the paper sheet is formed and due to different drainage conditions, a self-regulation for a uniform paper is present. After this forming section, a wet press section follows,

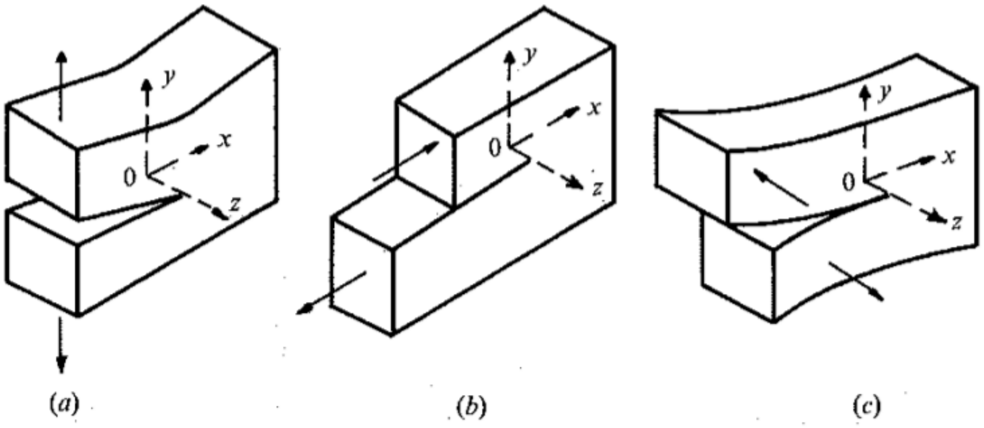

**Figure 2.7:** The three basic modes of fracture of cracked bodies. a) Tensile opening (mode I). b) In-plane sliding (mode II). (c) Anti-plane shear (mode III). (From [15].)

applying a load to the fiber-fiber bonds with several rollers and further removing of the water from the paper sheet. Finally, the paper is dried in a dryer section and the desired paper is obtained. The sequence of these stages is illustrated in figure 2.8.

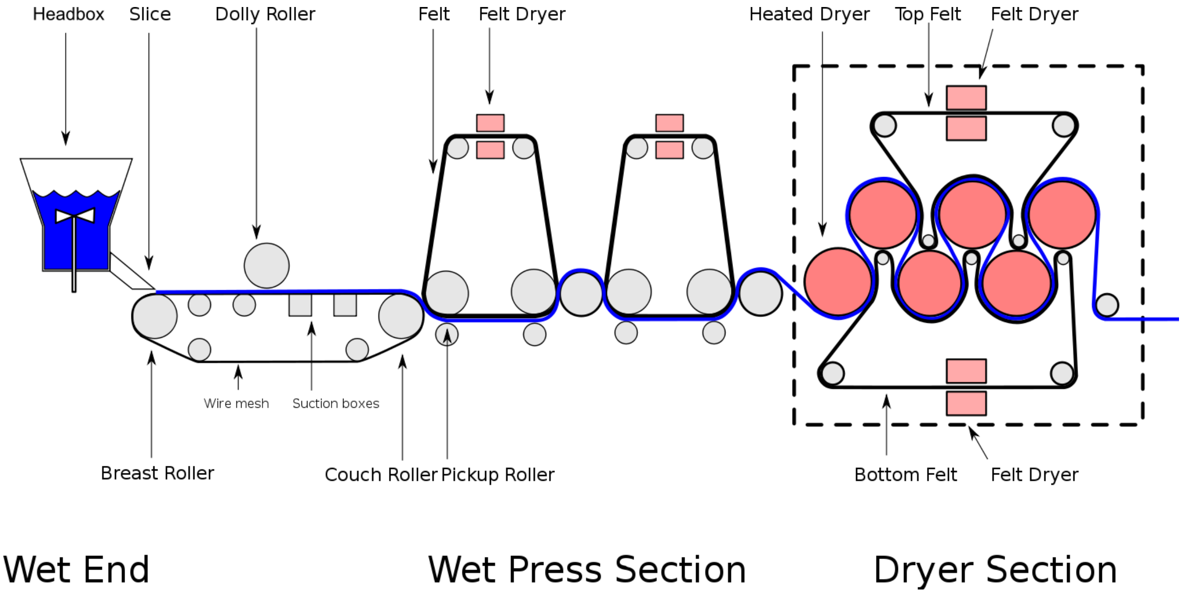

**Figure 2.8:** Scheme of a paper machine. (After [16].)

## 2.4 Important paper tests and index numbers

According to different treated pulps, it is necessary to know the most important paper tests and index numbers. These are beating, delignification, and dewatering. The following section deals with the description of these parameters and their influence on the paper pulp properties. Most of these values just represent an empirical description of the pulp and are easy to use within the production line [17]. Further, a simple macroscopic test is introduced to measure the paper strength in z-direction.

### 2.4.1 Beating

Beating is one of the most influencing processes on the tensile strength of pulp fibers. It increases the fiber-fiber bond strength itself, due to an increase of the bonding area and making the fibers more flexible. This facilitates fiber swelling and the possibility that two fibers can approach each other close enough. Figure 2.9 provides an overview of the effect of beating on different pulp properties. Here, tensile and fracture energy index are increasing dramatically, whereas the opacity is slightly decreased. Further, moderate beating has positive effect on the tear index, whereas highly beating reduces the tear index.

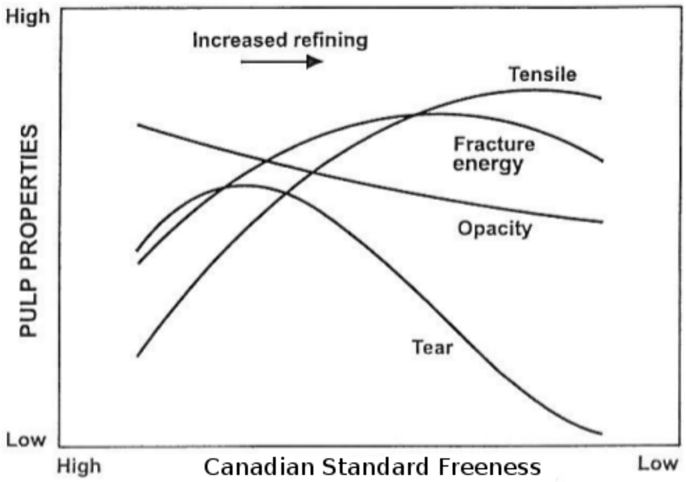

**Figure 2.9:** Influence of beating on several pulp properties. (From [17].)

The most common laboratory beater is the PFI mill which is represented in a schematic illustration in figure 2.10a. Here, the beating occurs between a bar roll and a smooth beater. Both parts are rotating in the same direction but with a different speed. The advantage of the PFI mill is the small amount of pulp that is needed (normally 30 g of demanded pulp per beating). The degree of beating depends on the revolutions inside the mill. Other laboratory beaters are Valley beater or Jokro mill. The Jokro mill is very similar to a PFI mill. Here, the beating occurs between bar surfaces and a smooth housing. The Valley beater is the setup which mimics best an industrial refiner and is described in figure 2.10b. However, it is more difficult in calibration and maintenance than a PFI mill. In a Valley beater, the beating occurs between a beater roll and a bed plate. Here, a larger amount of pulp (∼ 10 times more than in a PFI mill) can be tested. In a Valley beater, the removal of the outer cell walls is more efficient than for the other. The PFI and Jokro mill are producing stronger fibrillation on the other hand [17].

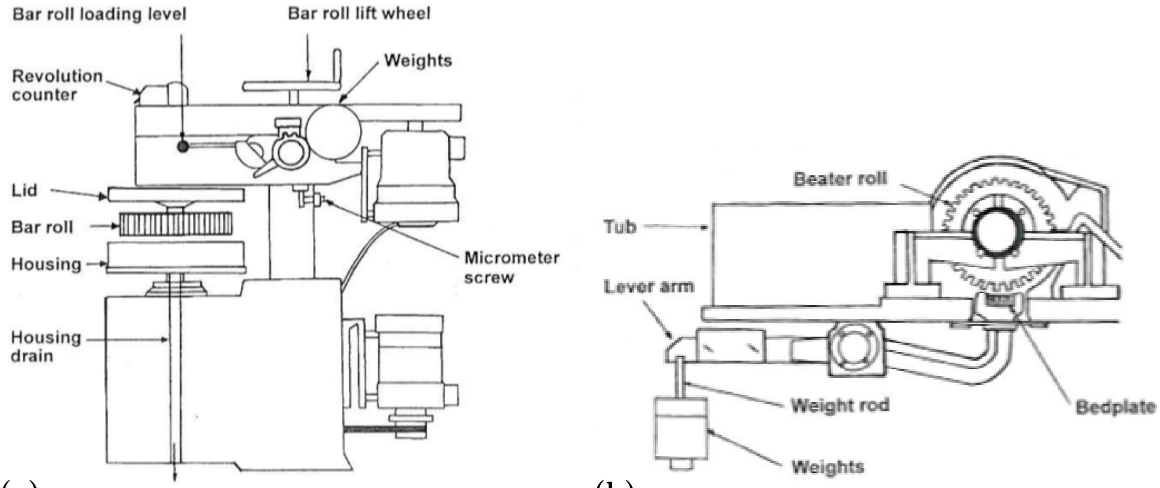

**(a)** **(b)**

**Figure 2.10:** Schematic illustration of various beater. a) PFI mill and b) Valley beater. (From [17].)

## 2.4.2 Dewatering

Another important parameter is the drainage resistance. The most common methods to determine the drainage resistance are the Canadian Standard Freeness (CSF), the Schopper-Riegler (SR), and the Water Retention Value (WRV). CSF and SR follow the same basic principle. One liter of diluted pulp solution filters through a screen plate of a testing device (see figure 2.11). For CSF the consistency is 3 $\frac{g}{L}$ whereas for SR the consistency is 2 $\frac{g}{L}$. Faster slowing of drainage due to fiber mat accumulation on the screen plate results in a smaller CSF number, measured by the amount of water passing through the side orifice. In SR, a faster slowing of drainage provides a higher SR number. That means, that the SR number is proportional to the fiber drainage, whereas the CSF number is indirectly proportional. Table 2.2 compares both techniques with respect to consistency and drainage resistance. Both methods depend strongly on the fines content and the compressibility of the pulp. The resulting CSF and SR numbers are empirical findings and they poorly describe the fibrillation of fibers during beating.

The WRV describes the amount of water remaining in a wet pulp after centrifugation. It is defined as the ratio between water and the dry fiber weight and is a measure of how tightly the fiber structure holds free water. The WRV provides better information

| Method | consistency $[\frac{g}{L}]$ | drainage resistance |
|---|---|---|
| CSF | 3 | ↓ |
| SR | 2 | ↑ |

**Table 2.2:** Comparison of Canadian Standard Freeness and Schopper-Riegler. (From [17].)

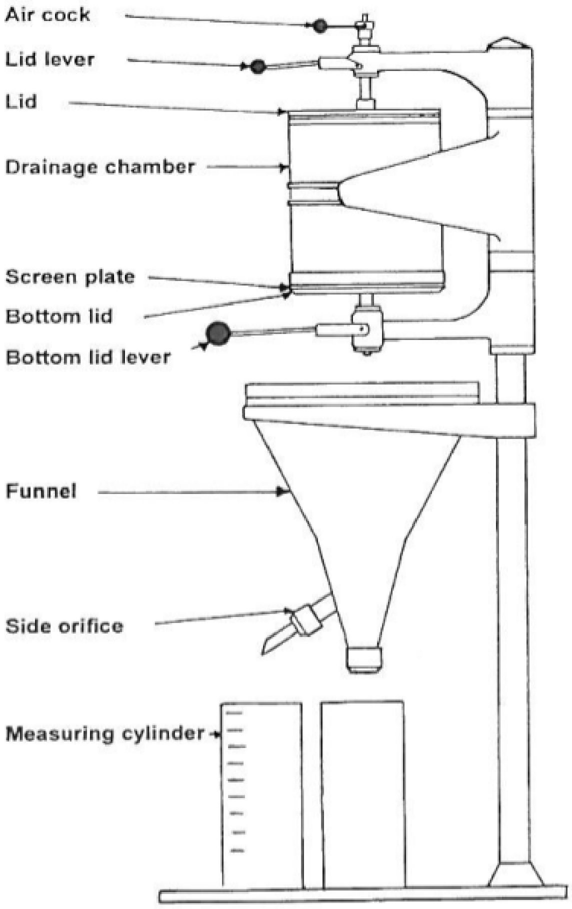

**Figure 2.11:** Schematic illustration of a Canadian Standard Freeness and a Schopper-Riegler tester. (From [17].)

about the refining response of fibers and the water removal during the press section than CSF and SR.

## 2.4.3 Delignification

To determine the degree of delignification, several methods have been developed based on reacting lignin with permanganate or a halogen. The Roe number [18] was an early standard obtained by reacting the moist pulp sample with chlorine gas. Nowadays, the most common index is the $\kappa$-number [19]. This number is defined as milliliter of 0.02M potassium permanganate ($KMnO_4$) solution consumed by 1 g of dry pulp in 10 min during treatment with potassium permanganate in sulfuric acid solution and converted to correspond with consumption of 50% permanganate. It should be mentioned that there is no general relationship between the $\kappa$-number and lignin content of the pulp.

Beside the oxidation of lignin also other compounds can be oxidized which increases the consumption of permanganate which raises the $\kappa$-number [20]. Further, one has to keep in mind that the $\kappa$-number depends on the wood species. The above described method is applied to all chemical pulps with a $\kappa$-number between 1 and 100. The amount of lignin in the pulp is estimated by multiplying the $\kappa$-number with 0.15.

$$\%\text{lignin} = \kappa\text{-number} \cdot 0.15\% \tag{2.1}$$

### 2.4.4 Z-strength

The z-directional strength is the ability of a paper sheet to resist a tensile loading perpendicular to the paper plane (z-direction). This strength is measured with a paper sample mounted between two metal pieces with adhesive tape or glue. This sandwich is pressed together to ensure a sufficient contact between the paper and the metal parts. There are many ways, to measure the z-strength and some methods are standardized, TAPPI UM 584, TAPPI UM 403, TAPPI UM 527, and TAPPI UM 528. The most common apparatus for testing z-strength is a Scott bond tester which is illustrated in figure 2.12. Here, the loss of kinetic energy is measured with a pendulum and indicates the strength of a paper. The simplicity of implementing this test has resulted in a large use in the paper industry.

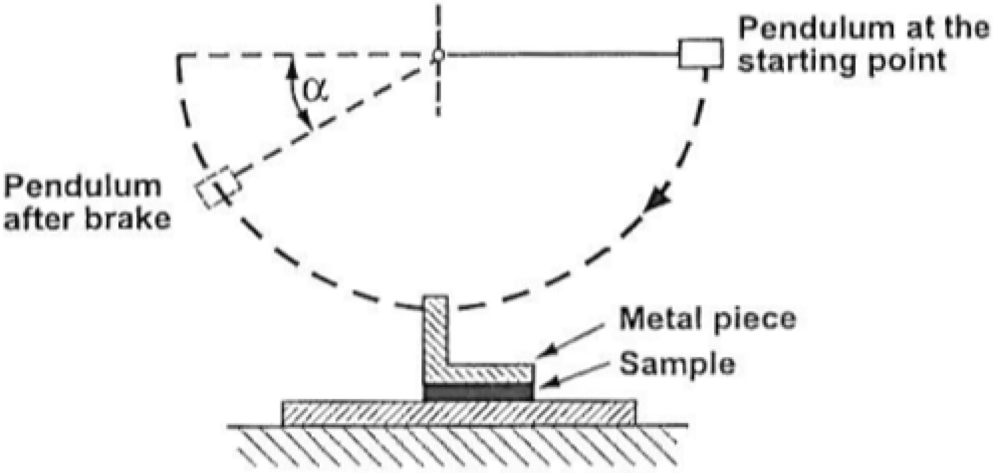

**Figure 2.12:** Illustration of the Scott bond tester. (From [17].)

## 2.5 State of the art

### 2.5.1 Surface characterization

In recent years, several surface-sensitive methods have been applied to paper fibers, e. g. Raman spectroscopy, Electron Spectroscopy for Chemical Analysis (ESCA) [21], X-ray Photoelectron Spectroscopy (XPS) [22, 23], Time-of-Flight Secondary Ion Mass-Spectroscopy (ToF-SIMS) [23], SEM [24] and AFM [25, 26]. For instance, bleaching of spruce kraft pulps was investigated by AFM and XPS [22] and was found to result in an increase of both - the O/C atomic ratio (measure for lignin content) and the amount of fibrillar surface structure. Different mechanical pulps were analyzed by ESCA and AFM [21] revealing that the surface composition of pulp fibers cannot be predicted from bulk values. Furthermore, a good agreement between the two techniques was stated. But for peroxide bleaching, AFM revealed changes that are not observed with ESCA. Based on AFM images, an enhanced data analysis of lignin was performed on different treated kraft pulp fibers [27] revealing phase imaging as suitable method to study delignification of pulp fibers.

### 2.5.2 Young's Modulus

To estimate bending and torsion of single pulp fibers, their Young's modulus E has to be known. Values for E are hard to access for such a complex hierarchical structure like a pulp fiber. Measurements on regenerated cellulose are reporting a large anisotropy of E in fiber axis direction and transverse to the fiber axis [28]. Especially the microfibrillar angle (MFA) has a tremendous effect on the Young's modulus [29, 30]. Table 2.3 provides an overview on measured Young's moduli of different cellulose fibers measured with nanoindentation on embedded samples [31, 32], tensile tests on single fibers [30, 33], and calculations from theoretical considerations [34].

| Fiber | E [GPa] | Method | Reference |
|---|---|---|---|
| Bocell | 46.6 | N | [28] |
| Earlywood | 13.5 | N | [29] |
| Latewood | 21 | N | [29] |
| Kraft Spruce | 20-80 | TT | [30] |
| Viscose | 11.6 | N | [31] |
| Lyocell | 22.3 | N | [31] |
| Northern Spruce | 10-20 | N | [32] |
| Spruce fiber | 10 | TT | [33] |
| Cellulose | 27.2 | Th | [34] |

**Table 2.3:** Literature data for the Youngs modulus E for several types of cellulose fibers. N - Nanoindentation, Th - Theory, TT - Tensile test.

### 2.5.3 Fiber-fiber bond testing

A very important step to get a deeper insight into bonding mechanisms of single fiber-fiber bonds are experimental data. So far, only bond strength data obtained by tensile testers [14, 35] are available in the literature. This approach has the disadvantage of representing a mode II (in-plane sliding) loading. Thus, these experiments deal with shear forces and have no access to a tensile opening mode. For instance, reference [10–12] report bonding strength for unbleached kraft pulp ranging from 1 to 6 mN (see table 2.4). Here in this thesis, a new technique based on AFM is used to apply a load on fiber-fiber bonds like it was similar utilized for carbon nanotubes [36–38], nanowires [39], nanofibers [40], collagen fibrils [41] and single cellulose fibrils [42].

| | Load [g] | Force [mN] | Bond strength [MPa] | Reference |
|---|---|---|---|---|
| Earlywood | 0.47 (0.48) | 4.6 | 2.1 (2.1) | [10] |
| Latewood | 0.87 (0.56) | 8.5 | 6.6 (4.2) | [10] |
| Kraft-mixed spruce and pine | 0.6 (0.3) | 5.8 | 2.9 (1.5) | [11] |
| Softwood kraft pulp | - (-) | 1-3 | - | [12] |
| Unbleached kraft pulp | - (-) | 1-2 | - | [13] |
| Dried kraft pulp Springwood | 0.11 (-) | 1.1 | 0.4 (0.2) | [14] |
| Dried kraft pulp Latewood | 0.14 (-) | 1.4 | 0.8 (1.0) | [14] |

**Table 2.4:** Fiber-fiber bond properties determined by shear bond strength measurements.

# 3 Experimental

## 3.1 Sample preparation

This section deals with the preparation of the individual pulp samples, including single fibers for surface investigation, as well as fiber cross-sections and fiber-fiber bonds. Beside standard AFM morphology investigations also the sample preparation for electrical characterization is briefly discussed. The main part of this chapter will deal with the formation, selection, and preparation of single fiber-fiber bonds for bond strength measurements using the developed AFM based setup.

### 3.1.1 Surface investigation

To extract single fibers from the pulp, a small amount of bulk pulp material is rewetted with a droplet of distilled water. This solution is put under an Optical Microscope (OM) to search for adequate fibers which are long enough and easy to handle in the further measurement procedure. Due to the high surface roughness of paper fibers, it is necessary to strain the single fiber to reduce additional buckling and twisting for high-resolution AFM imaging. Therefore, the fiber is strained over a silicon support which is marked by a diamond scribe. These scratches lead to an identification of depicted positions on the fiber and help refinding the same position in other microscopes like an SEM. Fiber mounting is performed with small pieces of adhesive tape. For measurements under liquid conditions - e.g. water - the adhesive tape is replaced by nail polish. Dried nail polish is unsolvable in water but can be removed with acetone ($(CH_3)_2CO$). The silicon support is fixated with double-sided adhesive Scotch tape on a commercial sample holder disc made of steel, which allows magnetical mounting to the AFM measurement system. Figure 3.1 is a photograph of a sample prepared by the above mentioned procedure.

### 3.1.2 Cross-sectional observation

For cross-sectional investigations, the samples have to be embedded into a resin (Technovit7100 [43]) and cut with an ultramicrotome (Leica RM2155 [44] using a diamond knife [45]). This preparation method - performed by colleagues of the Institute for Paper, Pulp and Fiber Productions at Graz University of Technology - allows to prepare single fiber cross-sections and longitudinal cross-sections, cross-sections of paper sheets and fiber-fiber bondings. Depending on the sample, prerequisiting steps are necessary. For the preparation of single fibers, the fibers are placed upright standing in a gelatin capsule and filled with the resin. The same procedure is used for paper sheets.

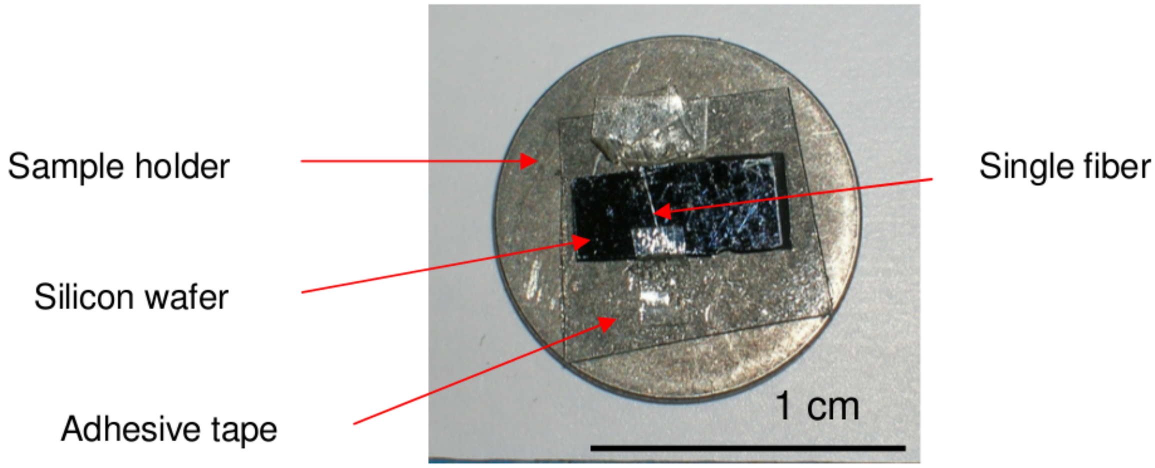

**Figure 3.1:** Single fiber sample on a silicon wafer. (From [1].)

Preparing fiber-fiber cross-sections needs more efforts. Here, the fiber-fiber bond (formation see section 3.1.3) is glued over a hole within a paper strip. For further investigation in the paper research group, this strip of paper is attached to a coated paper as an identification mark to stitch image sequences together. This sandwich sample is now embedded in the capsule with resin. Figure 3.2 represents schemes of the individual embedded fibers. After resin curing, the embedded sample is cut using an ultramicrotome with a diamond knife. A diamond knife is necessary to obtain smooth sample surfaces which are appropriate for high-resolution AFM imaging. The embedded samples are mounted in a homemade sample holder with plasticine for the AFM measurements (see figure 3.3).

For electrical characterization of paper fibers by AFM based techniques it is necessary to bias or ground the sample. Therefore, the Technovit7100 resin was replaced by a mixture of Demotec70 and Demotec20 which is a conductive polymer (see inset in figure 3.3). The sample showed a sufficient conductivity but reduced contrast in OM which made it harder to approach the tip at the desired measurement position.

### 3.1.3 Fiber-fiber bond

#### Sample holder for AFM based measurements of bond strength

For bond strength measurements using an AFM, a special sample holder was designed and improved in several steps of repetition. The basic principle of the device is a bench vise, where the two benches are approached and retracted by a screw. Figure 3.4 is a photograph of this homebuilt sample holder. Figure 3.4a shows the first prototype of the sample holder. Here, springs are pressing the benches together, and two screws were used to approach and separate the benches. Figure 3.4b represents the modified setup where only one spring is opening the gap and one screw is used to move the benches

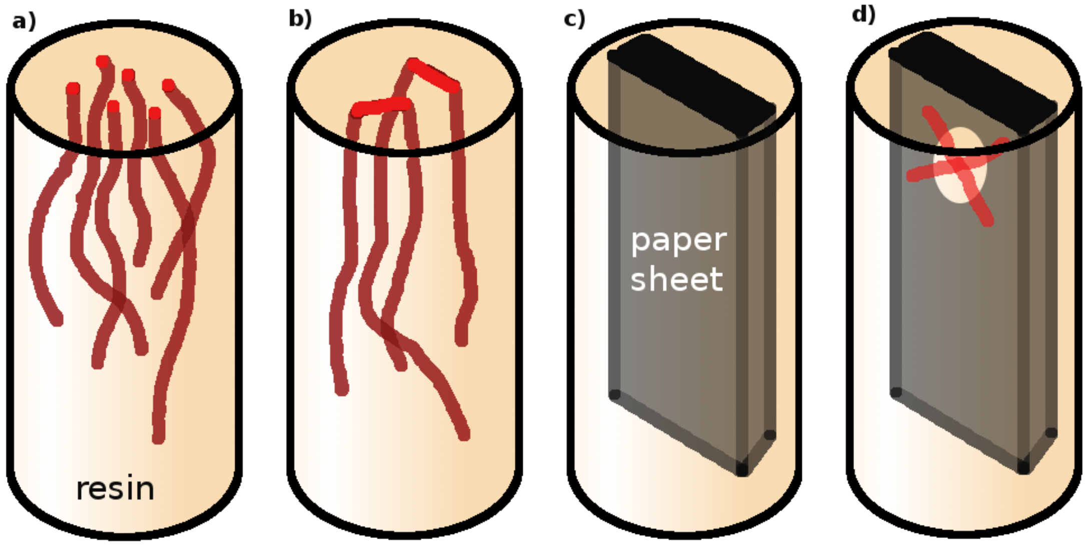

**Figure 3.2:** Scheme of different cross-sectional samples. a) Fiber cross-section, b) fiber longitudinal cross-section, c) paper sheet, d) fiber-fiber bond.

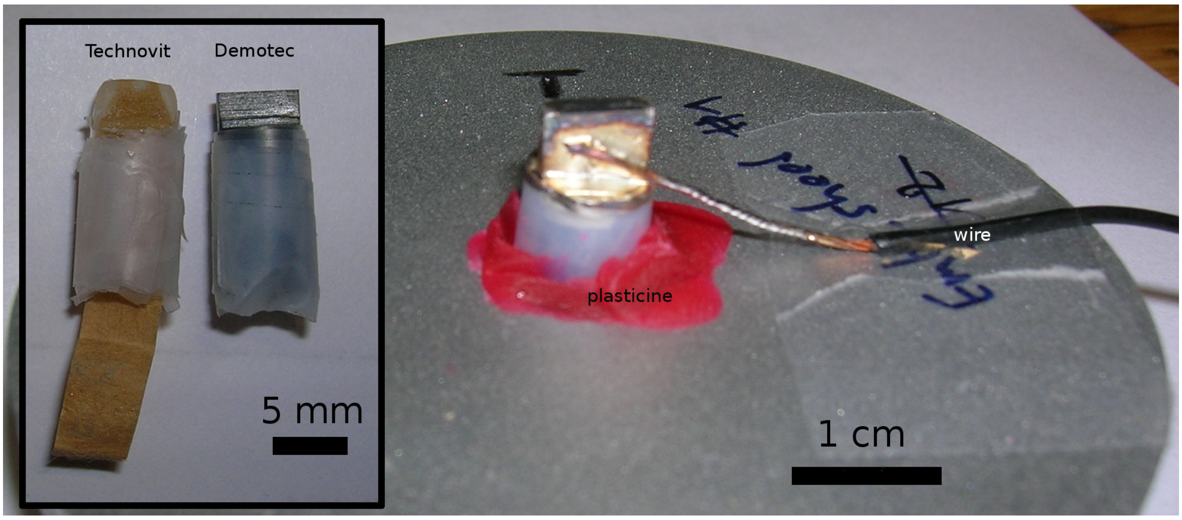

**Figure 3.3:** Embedded sample on sample holder grounded with a wire. The inset on the left shows the different embedding materials (Technovit and Demotec).

simultaneously. Further, two channels were implemented to reduce the amount of excess nail polish and keep the whole experimental setup in one single plane. To avoid high loading of the AFM xy-piezo scanner, the sample holder is made of aluminum. Mounting of the samples is performed with nail polish and will be described later.

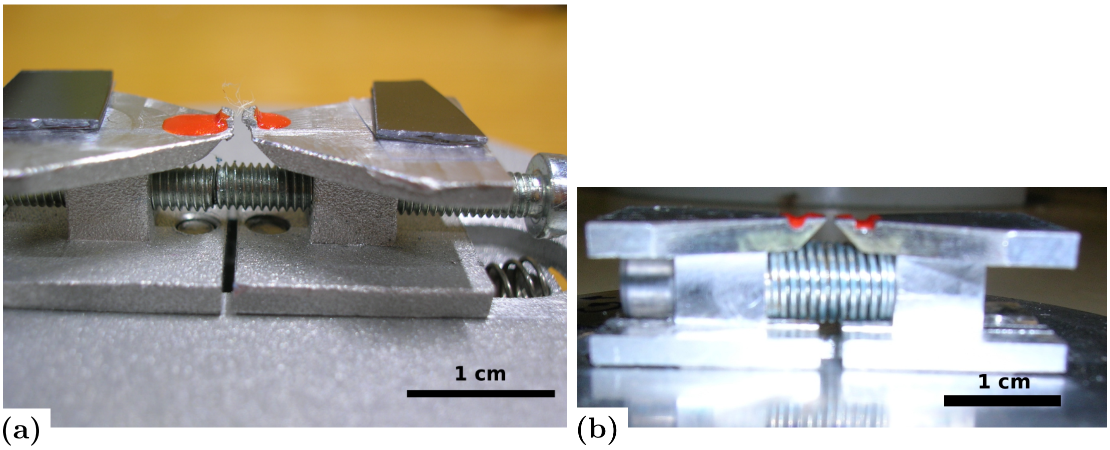

**Figure 3.4:** Photograph of the homebuilt sample holder for force measurements. a) Version I and b) advanced version II.

### Formation of fiber-fiber bonds

First investigations of fiber-fiber bondings were performed with homemade bonds. To form these bonds a droplet of solution of water and pulp was placed between two Teflon foils. To increase the possibility for fiber bonding, the Teflon foils were pressed together by a static load of 30 N. With this setup it was possible to establish first bonds and to test the sample mounting and the developed set-up.

For systematic investigation, sample preparation was carried out by the collaborating partner at the Institute for Paper, Pulp and Fiber Productions in Graz. A dilute suspension with a consistency of 0.01% is put on PTFE foils via a pipette. These foils are covered with another PTFE foil and the whole sandwich was dried in a conventional sheet dryer for 45 min [43].

### Mounting of fiber-fiber bonds into the special sample holder.

After the fiber-fiber bonds have been formed, they are mounted on the sample holder with nail polish (see figure 3.4). To form a sufficient mechanical contact between fiber, sample holder, and nail polish, the system is stored 24 hours under ambient conditions. After this period, the nail polish is cured and the bond strength measurement can start (see section 3.2.1).

To decrease the time prior to measurement and to increase the sample output, the samples were exposed to higher temperatures in an oven. There, the sample was heated between 50 and 60 °C half an hour. After that, the sample cooled down to room temperature and was stored for 3-4 hours under ambient conditions. Unfortunately, most of the fibers start to become brittle and tend to break during pre-straining (see figure 3.5). Therefore, all together 10 sample holders were crafted, to test more fiber-fiber bonds.

One problem of the fiber-fiber bond mounting is that single isolated fiber-fiber bonds are rare. Usually, several fibers form multiple bonds to each other resulting in a fiber

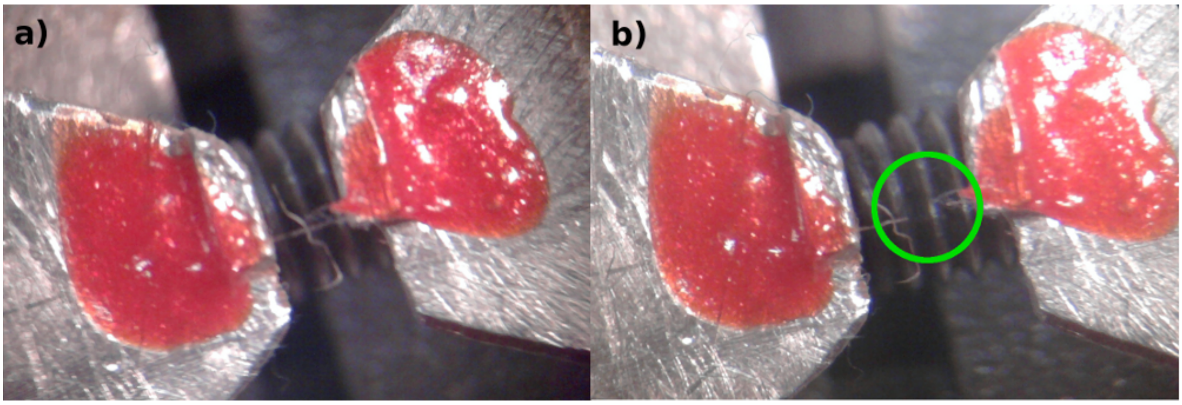

**Figure 3.5:** Fibers after bake out of the nail polish a) before and b) after straining. The broken strained fiber is marked with a green circle.

network (see figure 3.6). Thus, it is difficult to isolate the two fibers making the bond. This leads to additional problems during pre-straining due to uncontrolled force implementation into the fiber-fiber bond which increases bond failure. To overcome this problem, it is important to carefully cut the desired bond free of the fiber network in an unstrained state using a scalpel. This leads to isolated fiber-fiber bonds that are easier to mount and which bear a lower risk for damages while pre-straining.

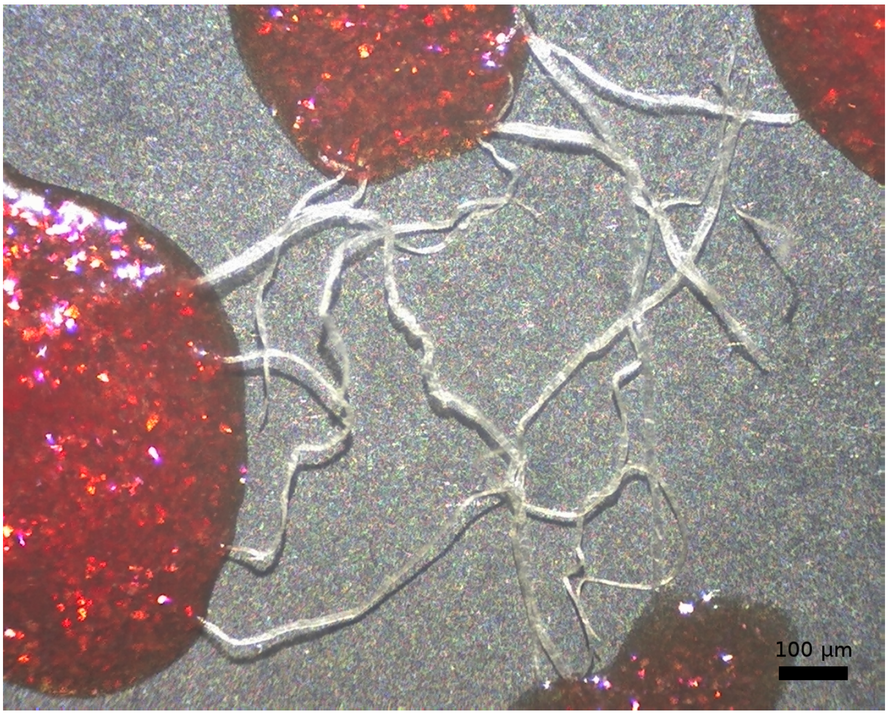

**Figure 3.6:** Typical fiber network between the Teflon foils.

## 3.2 AFM based characterization of paper fibers and fiber bonds.

### 3.2.1 Atomic Force Microscopy

AFM is a derivative of scanning tunneling microscopy [46, 47]. Instead of monitoring the tip-sample distance via tunneling currents, in AFM, the tip is placed at the end of a cantilever and its deflection is recorded with a laser beam deflection detection method. Here, a laser is reflected from the back side of the cantilever to a split four quadrant photodiode. With this detection method, small movements of the cantilever result in a significant change of the signal on the split photodiode. Therefore, it is feasible to measure smallest cantilever deflections with very high accuracy. During scanning of the tip across the surface, this sensor is coupled with the feedback loop, to keep the deflection at a constant value during the contact of tip and surface. The scanning of the sample is realized by a piezo scanner (tube scanner, xy-scanner). Figure 3.7 represent the basic principle of the AFM together with its feedback loop and the signal detection on the split photodiode. The movement of the laser spot on the split photodiode changes the photo current in the individual quadrant and this is used to track the cantilever movement. In contrast to STM, the cantilever principle of AFM allows also the inspection of insulating samples.

#### Tapping Mode

In case of measuring soft samples, like pulp fibers, measurements in contact mode can destroy the sample surface due to the high lateral forces. Therefore, a more gentle method is desirable do prevent sample damage. As method of choice, tapping mode was used [49], where the tip only punctually interacts with the sample which reduces sample damage and increases the lifetime of the tip. Here, the cantilever is externally excited into oscillation by a piezo driver. The tip interacting with the surface causes a damping of the oscillation amplitude ($A_0$) and a phase lag ($\Delta\phi$) between the oscillation driving the cantilever and the cantilever output signal on the split photodiode. The damping is used to obtain the height information. The phase lag corresponds to different material's properties, e.g., stiffness, adhesion, and visco-elasticity. Depending on the amplitude ratio [50, 51], the tip-sample interaction reflects different material's properties. Recording the phase lag is called Phase Imaging [49]. Table 3.1 provides an overview of the amplitude parameters and their influence on the phase signal. The amplitude ratio $r_{sp}$ is calculated by:

$$r_{sp} = \frac{A_{sp}}{A_0} \tag{3.1}$$

where $A_{sp}$ is the amplitude of the cantilever at the set-point value and $A_0$ is the amplitude of the free cantilever oscillation.

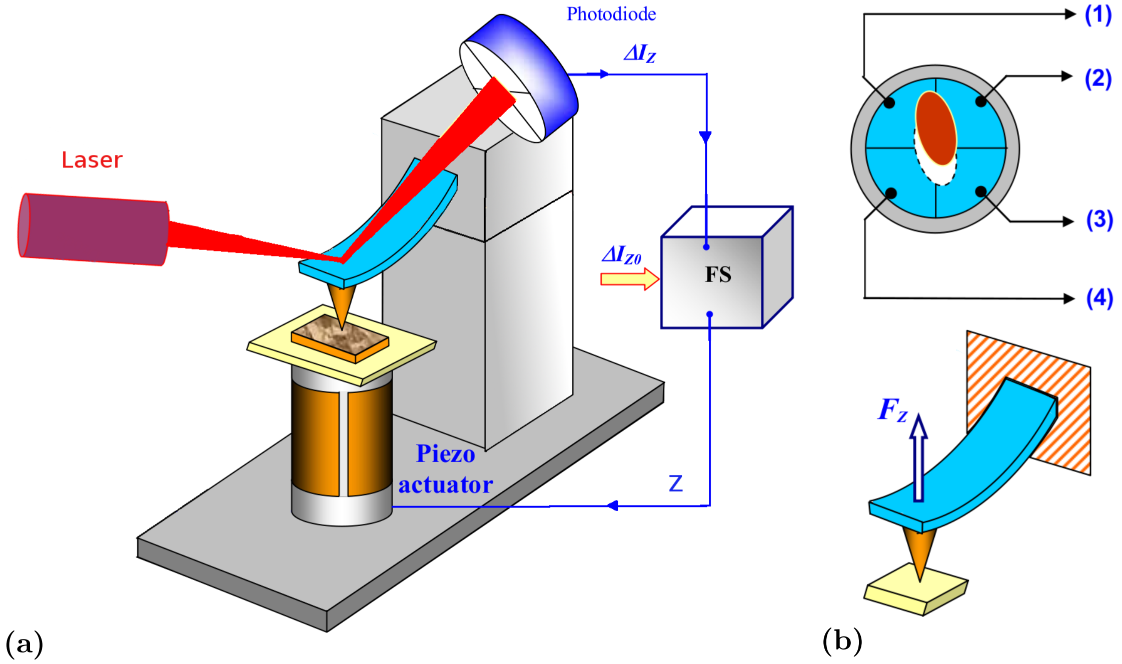

**Figure 3.7:** AFM principle showing a) feedback loop with laser reflected from the cantilever backside to a four quadrant photodiode and b) signal detection on split photodiode. FS - Feedback Signal, Z - voltage applied to piezo actuator, $\Delta I_z$ - measured current signal, and $\Delta I_{z0}$ - current input. (After [48].)

| Interaction Mode | $A_0$ [nm] | $r_{sp}$ | contrast |
|---|---|---|---|
| Light Tapping | 100 | >0.9 | adhesion |
| Moderate Tapping | 100 | 0.7-0.9 | adhesion |
| Hard Tapping | 100 | $< 0.7$ | stiffness |

**Table 3.1:** Tip-sample interaction modes for a constant $A_0$ depending on the ratio $r_{sp}$. (After [50].)

### Bimodal DualAC

Bimodal DualAC is a further development of tapping mode AFM. In tapping mode, the phase signal is locked to the feedback loop and information is lost due to reduced degrees of freedom. In Bimodal DualAC, the cantilever is driven at its first and second flexural harmonics [52–54]. For an AC240 cantilever, the prime resonance frequency is around 70 kHz and the second flexural harmonic is around 440 kHz. Here, the second amplitude and phase signals are considered to be independent of the feedback loop and are therefore more sensitive to material's parameters of the sample. Figure 3.8 summarizes the measurement principle of the technique. The two frequencies are applied to the cantilever with a shake piezo and the resulting cantilever deflection is analyzed with lock-in technique to separate amplitude and phase signals (see figure 3.8a). Figure 3.8b describes the cantilever bending of higher flexural modes.

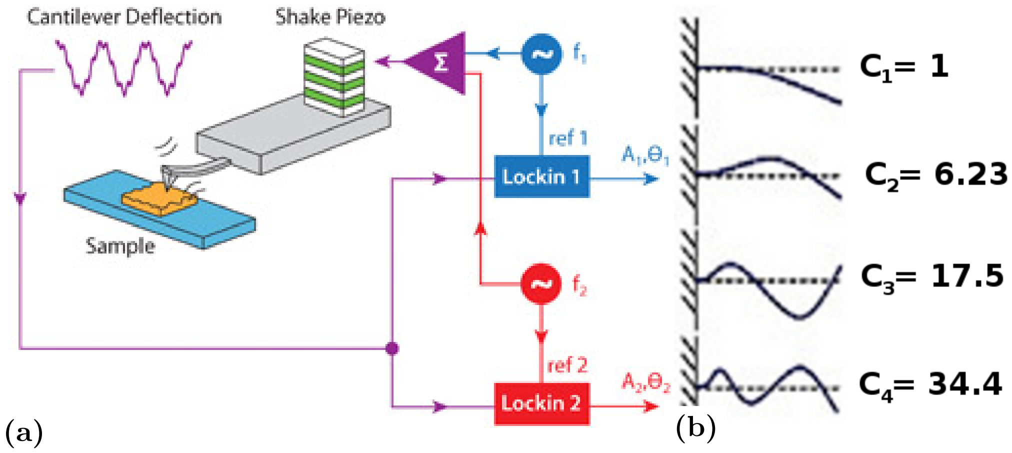

**Figure 3.8:** Bimodal DualAC. a) Measurement principle and b) higher flexural harmonics of the cantilever oscillation. (After [55].)

### Kelvin Probe Force Microscopy

Kelvin Probe Force Microscopy (KPFM) [56] is a derivative of AFM developed to study electrical properties of the sample on the nanometer scale and operates in tapping mode. In comparison to standard tapping mode AFM imaging modes, KPFM is a two pass technique. The commonly used setup for KPFM is illustrated in figure 3.9. In the first cycle, the sample topography is recorded in conventional tapping mode. In a second pass, the tip follows the topography at a certain lift height and the probe is biased with a DC and an AC voltage. This electrical excitation leads to a modulation of electrostatic tip-surface forces.

$$V_{tip} = V_{DC} + V_{AC} sin(\omega t) \tag{3.2}$$

$$F_{cap} = \frac{1}{2}(V_{tip} - \Phi(x))^2 \frac{dC}{dz} \tag{3.3}$$

Varying of the $V_{DC}$ component leads to a change in the tip-sample interaction and can extinguish the capacitive part of the interaction. If the interaction is nullified, the $V_{DC}$ corresponds to the Contact Potential Difference (CPD) between tip and the measured point of the sample. If the work function of the tip $\Phi_{tip}$ is known, one can determine the work function $\Phi(x)$ of the measured point.

$$\Phi(x) = \Phi_{tip} + CPD(x) \tag{3.4}$$

Instead of standard silicon probes, Pt, PtIr or diamond coated silicon probes are used, but also highly doped uncoated Si-tips can be employed.

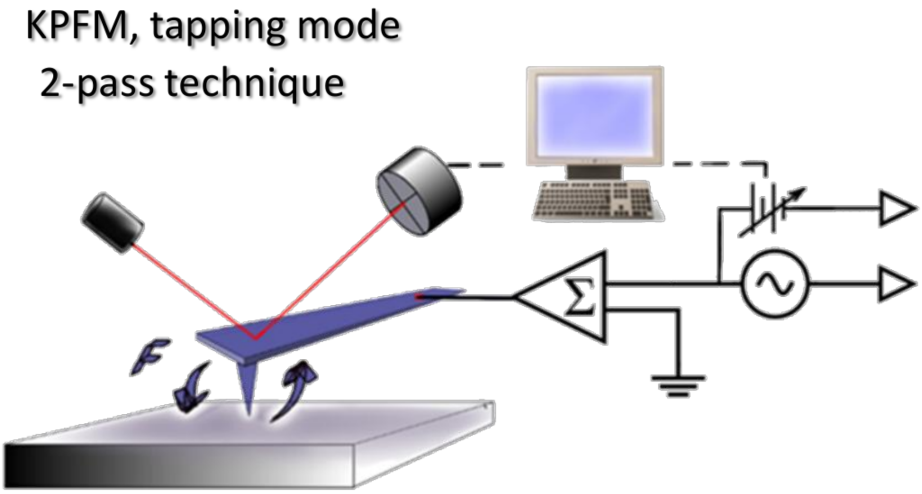

**Figure 3.9:** Measurement scheme of Kelvin Probe Force Microscopy. (From [57].)

### Force calibration of the AFM cantilever

To measure the absolute force applied by the cantilever to the sample it is necessary to calibrate the system to convert the cantilever deflection into the applied force. There are two important parameters concerning the force calibration. The first crucial parameter is the Deflection Invers Optical Lever Sensitivity (DeflInvOLS) which strongly depends on the position of the laser spot on the cantilever backside. Determination of the DeflInvOLS is carried out by pressing the cantilever against a hard surface (e.g. a silicon wafer) and recording a deflection-versus-distance curve. Here, the voltage shift on the split photodiode is correlated with the movement of the z-piezo and converts the measured voltage changes ($\Delta$V) into a cantilever deflection (nm). Regarding the position of the laser spot on the cantilever backside, there is a tremendous influence on the DeflInvOLS. The various laser positions and its influence on the DeflInvOLS are represented in figure 3.10. To achieve the best accuracy, the laser spot should be placed close to the front of the cantilever (figure 3.10c)

The second parameter influencing the applied force is of course the cantilever's spring constant. In order to determine it experimentally, the thermal sweep method [58] is used, which is included in the AFM software (IGOR version 6.12A MFP 090909+0829 of the Asylum Research MFP 3D AFM). Here, the spring constant is calculated from the resonance frequency $\omega_f$ and the quality factor $Q_f$ via recording the deflection of the cantilever as a function of the excitation frequency. Figure 3.11 represents a thermal graph - which is the average of several thermal sweeps - from the AFM software for two cantilevers with different stiffness. Stiffer cantilevers have a higher resonance frequency with a smaller amplitude and therefore a lower signal-to-noise ratio. To tackle that problem, averaging of the sweeping and the frequency resolution need to be increased.

These two parameters strongly depend on the cantilever used and on the position

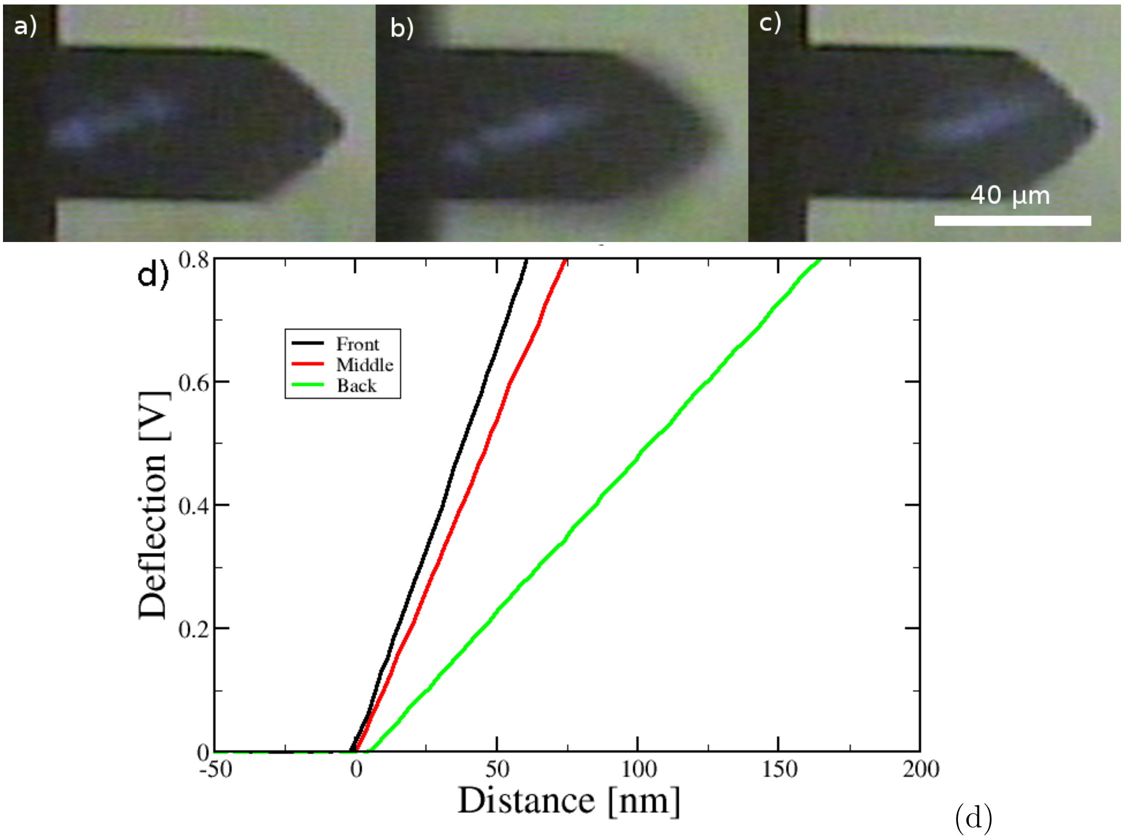

(d)

**Figure 3.10:** Various positions of the reflected laser on the cantilever backside and its influence on the deflection-distance ratio. Laser position on cantilever a) back, b) middle, c) front, and d) corresponding deflection-versus-distance dependencies.

of the laser spot on the cantilever backside. Table 3.2 summarizes important data of cantilevers tested in this work. According to simple beam theory which is neglecting the tip mass at the end of the cantilever, the spring constant (k) of a beam shaped cantilever is

$$k = 3\frac{Ewt^3}{12l^3} \tag{3.5}$$

where E is the Young's modulus, and w, l, and t are the width, length, and thickness of the cantilever, respectively.

Consequently, there are several possibilities to increase the spring constant and therefore the maximum applicable force. The first one is to change the cantilever's material (normally silicon) for instance by diamond, which increases linearly the spring constant due to a higher Young's modulus. More effective changes are expected by increasing the thickness or length of the beam because these parameters increase the spring constant with the power of three. The latter one has the disadvantage that there is a minimum beam length required to gain access to the fiber-fiber bond. Therefore, the most crucial

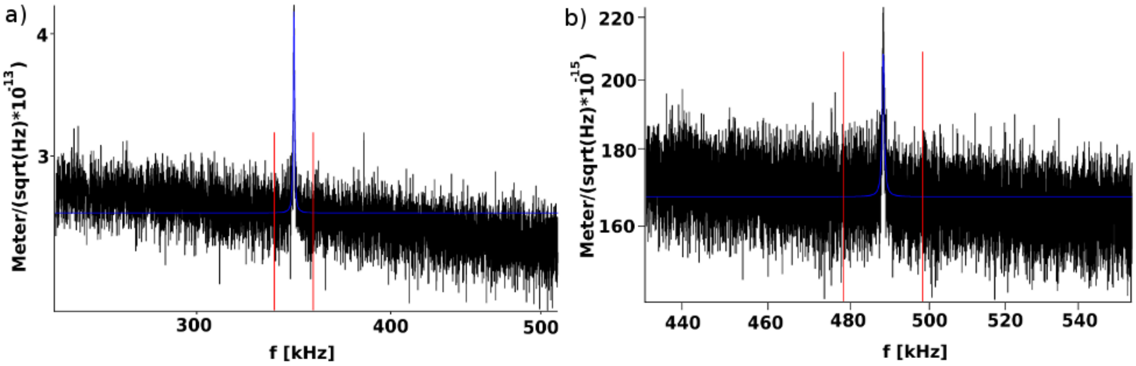

**Figure 3.11:** Thermal graphs of two different cantilevers. a) Olympus AC160 and b) Veeco MPP-13220. Red lines indicate the boundaries of the frequency range to fit the peak (blue line).

parameter affecting the spring constant is the thickness of the cantilever.

### Force measurement

The force measurements were carried out with the Asylum Research MFP 3D with the homebuilt sample holder previously described (see figure 3.4). The fiber-fiber bond is placed over an adjustable gap, and the top fiber is mounted with nail polish at its ends (see figure 3.12). The top fiber is then strained to a straight position and the cantilever is approached close to the fiber-fiber bond. After the automatic approach resulting in contact between tip and sample, there are two possible modes to apply a force. Figure 3.13 presents the two possible experimental modes. The first one is a displacement controlled experiment. Here, the z-piezo is used to increase or decrease the force, via approaching or retracting, respectively. The experiment is controlled with the AFM software and additionally, the deflection of the cantilever and the movement of the z-piezo are recorded externally with a small LabView program during the whole experiment. Due to a cyclic loading, it is possible to calculate the pure elastic energy from the released energy and the dissipated part from the energy loss of the experiment.

The second experiment is force controlled. Here, the applied force is controlled and the deflection of the cantilever is kept constant with the feedback loop set-point. In this experiment, the deflection of the cantilever and the displacement are recorded during the whole experiment externally using LabView. Due to the constant force, it is possible to investigate time dependent mechanisms such as creep and relaxation and finally, to calculate the visco-elastic energy of the single fiber-fiber bond.

During the whole experiment, additionally the OM images are recorded using the free software DScaler [59]. This allows to measure all distances within the experiment for further calculations and simulations and to check if the chip holding the cantilever never touches the sample holder during the experiment.

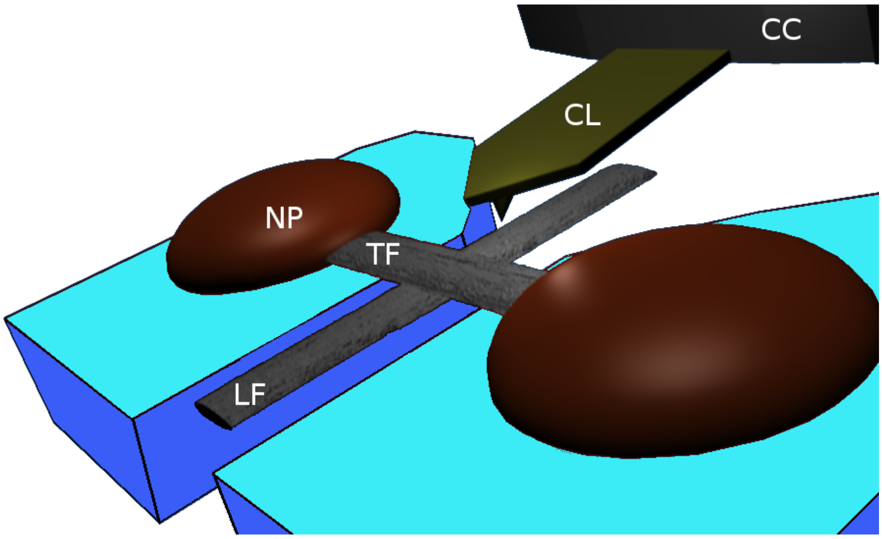

**Figure 3.12:** Scetch of the principle to measure the fiber-fiber bond strength, TF-Top fiber, LF-Lower fiber, NP-Nail polish, CL-Cantilever, and CC - Cantilever chip.

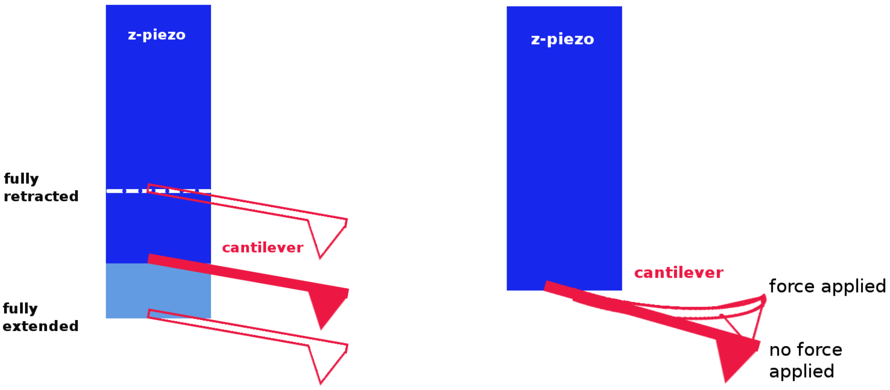

(a) (b)

**Figure 3.13:** Measuring modes: a) Displacement controlled, b) force controlled.

### Nanoindentation

Nanoindentation is a method to determine material's hardness on the nanometer scale [60]. Here, a defined probe - called a nanoindenter - (with known shape and material's properties - normally diamond) is pressed by a transducer against the material under investigation. Normally, a nanoindenter with a Berkovich tip with a three-sided pyramid geometry is used to test materials. On soft samples, a silicon probe is hard enough, to indent samples like pulp fibers and can be used to determine material's hardness. The initial unloading stiffness (S) of the material is determined from the tangent of the unloading curve at maximum force [61]. Figure 3.14 illustrates a schematic representation of a load-versus-indenter displacement curve based on a loading and unloading cycle to the peak load ($P_{max}$) at the indenter displacement ($h_{max}$). The final depth of the contact impression after unloading is marked as $h_f$.

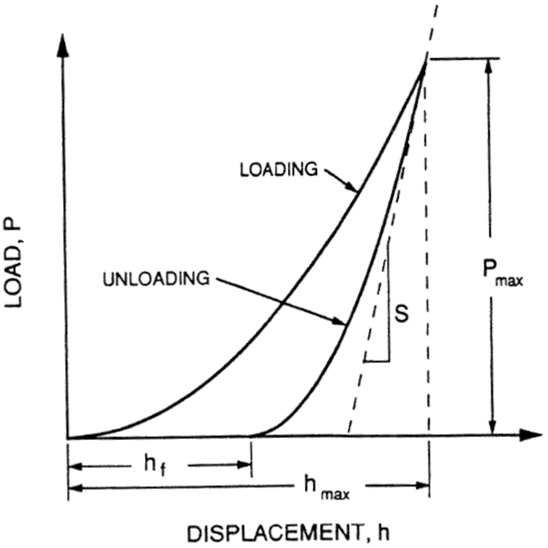

**Figure 3.14:** Schematic representation of load-versus-indenter displacement data. (From [61].)

To determine the area in contact (A), a Hertzian contact model was used [62] and the AFM tip has been approximated as a spherical indenter.

$$A = \pi r^2 \tag{3.6}$$

$$r = \sqrt{R h_{max}} \tag{3.7}$$

According to the indenter's tip geometry, $R$ is defined as the tip radius (which is $< 15$ nm) and $h_{max}$ is the penetration depth. If the area in contact is known, it is possible to calculate the so called indentation hardness H.

$$H = \frac{F}{A} \tag{3.8}$$

## 3.2.2 AFM Probes

There are several commercial suppliers of AFM probes available which are offering different cantilever/chip combinations. **Olympus** probes are the standard silicon probes for the Asylum Research MFP 3D AFM. Two different kind of probes were utilized. For simple tapping mode imaging, AC 160 probes were used. These probes show a robust behavior on the system for surface investigations. To increase the contrast in phase mode imaging, AC 240 probes were utilized. Here, the cantilever has a lower frequency

| Probe type | M | f [kHz] | C [N/m] | r [nm] | w x l x h [$\mu$m] | $F_{max}$ [$\mu$N] | Exp |
|---|---|---|---|---|---|---|---|
| Olympus AC 240 | Si | 70-75 | 2-3 | 7 | 30 x 240 x 2.7 | 1 | I |
| Olympus AC 160 | Si | 310-360 | 35-45 | 7 | 50 x 160 x 4.6 | 100 | I,F |
| NS PPP-NCHR | Si | 260-340 | 40-70 | <7 | 30 x 125 x 4.0 | 100 | I,F |
| ADT ND-DYIRS | UNCD | 240-300 | 32-50 | 15-30 | 33 x 120 x 2.5 | 100 | F |
| Veeco MPP-13220 | Si | 490 | 250-460 | 10 | 40 x 125 x 7.0 | 500 | F |
| Nanotec HSC | Si | 693 | 560-760 | <60 | 35 x 125 x 10 | 1000 | F |

**Table 3.2:** Typical values for used cantilevers. M-Material, f-frequency, C-spring constant, r-tip radius, w-width, l-length, h-height, $F_{max}$-maximum applicable force, Exp - Experiment, F - Force, I - Imaging.

and spring constant than the AC 160 one (see table 3.2). Due to this lower frequency, these cantilevers are best suitable for Bimodal DualAC measurements. First breaking experiments were done using AC 160 cantilevers. Unfortunately the detectable force (maximum force: 100 N) is too low for an instrumented experiment.

Probes from **Nanosensors (NS)** are standard tapping mode tips especially dedicated for the Digital Instruments Multimode IIIa AFM. These tips show a robust measurement performance and were mainly used for surface morphology investigations. The typical specifications are rather similar to the Olympus AC160 probes (see table 3.2).

The probes from **Advanced Diamond Technologies (ADT)** are the only probes presented in this work that are not made of silicon. These probes are made of bulk nanocrystalline diamond - called UNCD. Both - the tip and the cantilever - are made in a monolithic process. Due to the small cantilever thickness, they have a similar spring constant as Olympus AC160 and Nanosensors PPP-NCHR. Thicker cantilever of this material would be desirable but are not yet available from the manufacturer.

The MPP-13220 probes from **Veeco** are probes with a stiffer cantilever. This is achieved due to higher thickness of the Si cantilever. In comparison to the other cantilevers, they are twice to thrice the thickness of the standard cantilevers (see table 3.2). The main advantage of this stiff cantilever is its high spring constant, which leads to a high loading for the force experiments. The drawback of these probes is the small amplitude of the cantilever oscillation for the thermal sweep method to determine the spring constant. Due to the high cantilever stiffness the excitation peak is less pronounced than for the standard cantilever. To achieve a better signal to noise ratio more sweeping cycles (156, default 128) with a higher resolution (3, default 5) need to be acquired.

The **Nanotec** HSC probes are the stiffest cantilevers tested within this work. Additionally, the tip is coated with a tungsten carbide film. Beside the high stiffness of the cantilever, the probes tested here had a larger tip radius compared to standard probes. Due to the high stiffness, it is again very difficult to determine the spring constant of the cantilever. Therefore, more sweeping cycles (256) should be acquired with a frequency resolution of 2-3. The larger tip radius is considered to reduce the tip indentation to the soft sample.

One has to keep in mind that the detection limit of the photodiode is always the same. Therefore, an increased cantilever spring constant results in lower detection limit of force changes. The minimal detectable force (in nN) is approximately the value of the spring constant, i.e., Veeco MPP-13220 (C = 300 $\frac{N}{m}$, $F_{min}$ = 300 nN).

### Modification of the cantilever chips

One of the major problems in fiber handling in the AFM is the small dimension of the single fibers and especially of the fiber-fiber bond samples. After mounting, the top fiber is strained over a gap of approximately one to two millimeters. This gap distance is approximately the typical width of the cantilever chip ($\sim$ 1.6 mm). Therefore, special modifications of the cantilever chip had to be performed to prevent the chip from touching the support of the sample holder before the tip touches the fiber. To solve this problem, the chip has to be narrowed towards the cantilever as it is demonstrated in figure 3.15.

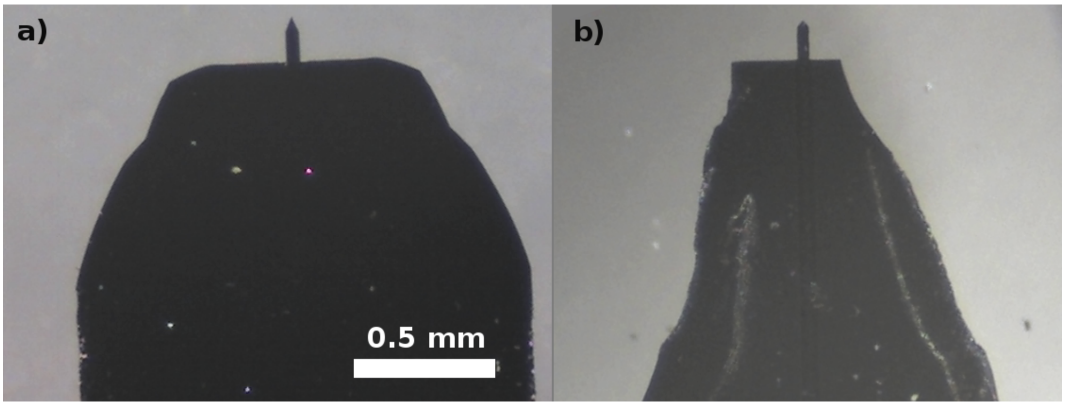

**Figure 3.15:** Optical image of cantilever and chip, a) before and b) after truncation by repeated breaking with tweezers.

For first trials, the silicon chip was gently scratched with a diamond cutter and then broken over an edge. Unfortunately, the amount of surviving cantilevers is very low (less than 50 %) due to positioning problems with the diamond scribe inside the OM. As second method, the cantilevers were modified by continuously breaking off small pieces of the silicon chip with tweezers. This method is more reliable and leads to a yield of more than 80 %.

### Tip geometry

To determine forces on the nanometer scale it is necessary to pay attention to the area of contact, which strongly depends on the tip geometry. The small tip radius of standard probes promotes tip indentation into soft samples. Therefore, other types of tip geometries such as spheres (see figure 3.16b) or truncated pyramids should be used to prevent sample indentation. First tries were performed using probes with a larger tip radius (see table 3.2). The advantage of the sphere geometry would be that the size of the contact area is independent of the cantilever bending. However, these colloidal probes are so far only commercially available on weak cantilevers used for Friction Force Microscopy and are therefore not usable for force experiments.

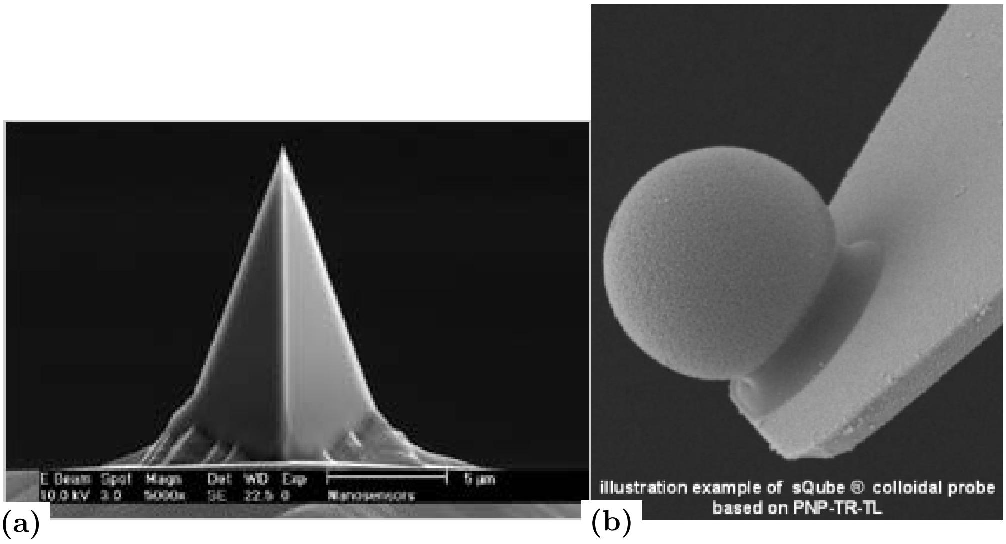

**Figure 3.16:** Different tip geometries. a) Standard tip and b) a colloidal probe. (From [63].)

## 3.3 Scanning Electron Microscopy

Scanning Electron Microscopy (SEM) [64] is a well established method in material's characterization. The images presented in this work were acquired at the Institute for Electron Microscopy and Fine Structure Research (FELMI) and Graz Centre for Electron Microscopy (ZFE Graz). The images were performed as comparative measurements to confirm the AFM data.

In SEM, an electron beam is scanned across the sample. There are two different ways for the electrons to interact with the sample: (i) back scattered electrons, and (ii) secondary electrons. The back scattered electrons give a material's contrast whereas the secondary electron emission yields a material's topographic contrast. However, the contrast depends also on the angle of the areas and the higher emission at the edges. Thus, SEM yields easy material's contrast but no reliable topography information on the nanometer scale [1].

SEM investigation of biological fibers are more difficult due to charging effects of the sample itself. This problem can be overcome by using an Environmental Scanning Electron Microscope (ESEM) [65] or Au coated samples. Both techniques yielded similar lateral resolution. ESEM was used as measurement tool of choice to keep samples under natural conditions. Great effort was undertaken to inspect exactly the same position with both techniques - AFM and SEM - in order to compare these two complementary techniques. Thus, scratches with a diamond scribe were made into the silicon wafer supporting the fiber as individual reference points. To achieve real 3D images with SEM, an image series was recorded with continuous tilting of the sample [66]. The resulting lateral changes in the images are used to calculate stereographic images allowing access to a true height information.

## 3.4 Optical Microscopy

Optical Microscopy (OM) is the standard technique to investigate paper samples. A lot of important parameters, such as width, length, curle and twisting are easily accessed in the bulk or for single fibers on a dark support. More problematic are investigations of single fibers without support due to the semi-transparent optical properties that hinder high resolution optical images.

A more severe problem for force measurements presented in this thesis is the necessity to know which of the two involved fibers is the top fiber of a fiber-fiber bond. Thus, different OM techniques were tested, without finding a proper solution, due to the semi-transparent optical properties of the sample. Unfortunately, the author has to state that - without a supporting material - it is not possible to focus on the fiber surface. This circumstance makes it hard to identify higher and lower parts. The best imaging results were achieved with an Infinite Focus Microscope [67], but even here, a clear determination of the top fiber was not possible, due to a flattening effect of the semi-transparent fibers (see figure 3.17).

## 3.5 Estimation of the area in molecular contact

In tribology research, the area of contact is a very important parameter in order to know the sliding behavior of two bodies. Based on material's properties (M = mass of moving body, $\sigma_c$ = indentation hardness) and fundamental constants, (g = acceleration of gravity: 9.81 $\mathrm{ms}^{-2}$) the area in molecular contact (ΔA) can be estimated [68]:

$$\frac{Mg}{\sigma_c} = \Delta A. \tag{3.9}$$

For instance, calculation of the area of molecular contact of two steel bodies yielded a $10^5$ times smaller area than the corresponding optically determined bonded area. A similar ratio is expected for the area in molecular contact of a fiber-fiber bond.

## 3.6 Analysis

### 3.6.1 Image analysis

The AFM image analysis was done using the free software Gwyddion [69]. Post-processing of topography images was performed with the step-line correction to level

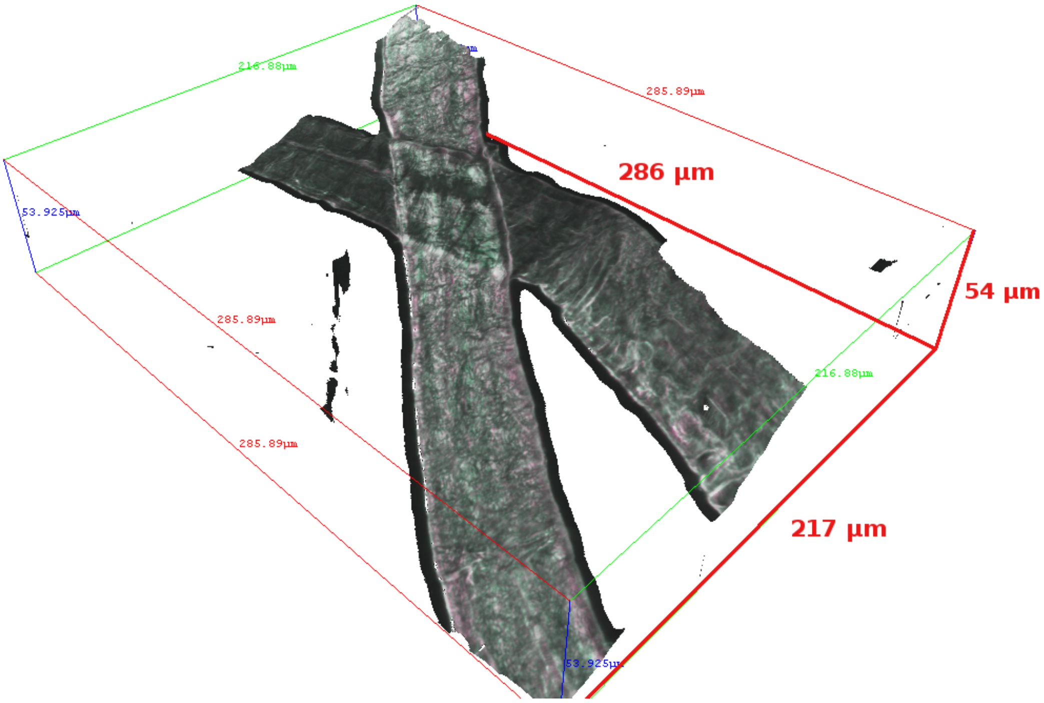

**Figure 3.17:** Infinite Focus Microscopy image of a fiber-fiber bond measured on an Alicona4G. (From [67].)

each scan-line and a first order planefit to remove a tilt of the sample. Phase images and other channels where analyzed without post-processing.

### Roughness

Roughness is a term describing the surface morphology of a sample. To describe a surface in detail, feature fluctuations should be described in z-direction as well as in the xy-plane. In AFM, the height parameters are described as a function of the lateral position $z = f(xy)$. Normally, AFM images are taken with a pixel resolution of 512 pixels in 512 rows, resulting in a 512 x 512 matrix including the height information. A first parameter to describe feature fluctuations in z-direction is the rms-roughness $\sigma$ which is calculated by the following equations:

$$\langle z \rangle = \frac{1}{MN} \sum_{k=0}^{M-1} \sum_{l=0}^{N-1} z(x_k, y_l) \tag{3.10}$$

$$\sigma = \sqrt{\frac{1}{MN}\sum_{k=0}^{M-1}\sum_{l=0}^{N-1}[z(x_k, y_l) - \langle z\rangle]^2} \tag{3.11}$$

where M and N are the number of pixels in a line and the number of lines.

To describe the ratio between the true surface area and the projected area, the so called Wenzel ratio (WR) [70] can be calculated which is defined as the ratio of the true surface area ($A_{true}$) to the projected surface area ($A_{proj}$).

$$WR = \frac{A_{true}}{A_{proj}} \tag{3.12}$$

From a given AFM topography image, the WR can be easily calculated using the Gwyddion software. This value which is very important to evaluate fiber-fiber bonding is a measure for the roughness of the depicted region. It was applied to distinguish between bonded and unbonded areas on the fiber surface.

### Fast Fourier Transformation of AFM images

Analysis of preferred orientation of fibrils from AFM phase images was performed by analyzing the reciprocal space with a two-dimensional Fast-Fourier Transformation (FFT). Here, harmonic components are decomposed from the AFM image and are displayed in the reciprocal space. Due to the finite size of the AFM images, artifacts from boundary conditions are detected and should be excluded from analysis by the use of windowing functions [71]. From a peak splitting in the FFT it is possible to determine a preferential feature-to-feature distance [72]. If the features touch each other, this distance corresponds to the feature size.

### Watershed analysis

To determine the spherical lignin precipitates on the fiber surface, a two step procedure - demonstrated in figure 3.18 - was applied to separate the lignin precipitates from the elongated microfibrils. First, a watershed algorithm [73] was performed to separate all the features. This algorithm detects lower regions that are surrounded by a somewhat higher boundary. Here, small droplets are filling the valleys till two neighboring ones are merging together. This is prevented and defines the border between two features. Second, after the separation of the features an area criterion is used two select the globules. The elongated microfibrils have a larger area than the spherule lignin precipitates. The remaining elongated structures are detected and deleted manually from the mask. This masking procedure is used to generate histograms of the individual precipitation diameter.

### Stitching

Due to the large surface roughness of pulp fibers and fiber curvature, it is only possible to measure areas of approximately 20 x 10 $\mu m^2$ with the long dimension along the

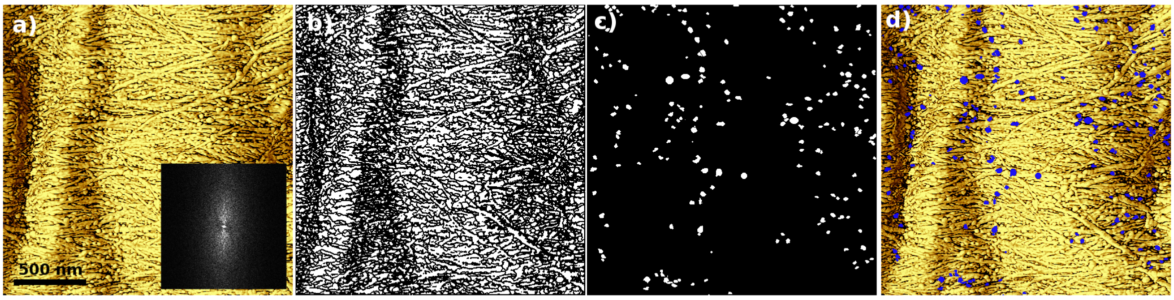

**Figure 3.18:** Watershed analysis of precipitated lignin. a) Phase image ($\phi$-scale=50°), b) watershed algorithm performed on a), c) final mask, and d) final mask overlaying the initial phase image from a).

fiber axis. Interesting areas, like the formerly bonded area of a broken fiber-fiber bond, are significantly larger. Nevertheless, they are worth to be investigated with a sufficient resolution. To extend the instrumental limitations, a measurement series with overlapping areas was performed and manually stitched with the free software Gimp [74]. This allows to present fiber surface images of an area of 100 x 40 $\mu m^2$ where clear differences between bonded and unbonded areas can be investigated.

### 3.6.2 Force-versus-distance curves

The force-versus-distance (F-x) curves, recorded in the bond strength measurements, were analyzed with a program written by the author for the free software Octave [75], which is compatible to Matlab. Here, the conversion from cantilever deflection to force was performed using the determined DeflInvOLS and the spring constant k.

$$F[nN] = Deflection[V] \cdot DeflInvOLS[\frac{nm}{V}] \cdot k[\frac{nN}{nm}] \tag{3.13}$$

The presentation of the data was performed with the free software Grace [76], as well as fitting procedures. Both programs were accessed from a command prompt and allowed a quick presentation of the data.

# 4 Results and discussion

## 4.1 Surface investigations

This section deals with surface morphology investigations of paper fibers and discusses surface features like microfibrils, lignin precipitates, pits, and the process of hornification. Different surface treatments of pulp and their influence on the fiber surface morphology are evaluated. With respect to fiber-fiber bonds, a comparison between previously bonded and unbonded surface areas is presented, showing significant changes on the fiber's surface morphology between the bonded and the unbonded region. All samples were measured under ambient conditions.

Besides the chemical composition and the bonding area, lignin content and the fiber surface morphology influence bonding mechanisms. Lignin on the fiber surface decreases the swelling tendency of the fiber, which changes the flexibility of the fiber and therefore decreases the bonding options. Additionally, surface lignin inhibits the formation of hydrogen bonds, since it has a lower amount of OH- groups than hemicellulose does. Beside this, the fiber surface morphology determines the possible approach of two adjacent fibers and limits the area in molecular contact. Thus, an investigation of pulp fiber surfaces on the nanometer scale is desirable.

In order to get a deeper insight into kraft pulp surfaces we used AFM as a method of choice. Here, we present AFM phase images as it is common practice in AFM investigations of pulp fibers because they reveal usually better contrast than AFM topography images. Furthermore, higher flexural mode AFM images are presented, showing an increased contrast. The latter method was already successfully applied on collagen fibers revealing information of molecules inside the investigated sample [55] but has not yet been applied to pulp fibers. Additionally, SEM images from the same position of the fibers have been recorded and compared to the AFM images confirming findings obtained by these two complementary techniques.

Figure 4.1a shows an optical image of an industrial pulp fiber mounted on a scratched silicon support together with the AFM cantilever. Figures 4.1b,c are representing SEM images of the shaded area in (a). Here, the lower resolved SEM image (b) represents a wrinkled surface on a larger scale. In the higher resolved SEM image (c), indications of smaller features - cellulose microfibrils or fibril bundles - are recognizable. Figures 4.1d,e are the corresponding AFM height and phase images of the marked area in (c), presenting similar features in the height image (d) but revealing clearly additional features in the corresponding phase image (e). Figure 4.1f is a high-resolution AFM phase image from the shaded area in (e). For figure 4.1f, the cell wall is considered to be the S1 with remainders of the primary wall due to the preferred orientation of the microfibrils almost perpendicular to the main fiber axis (top-down). Additionally to these perpendicular microfibrils, some diagonally oriented microfibrils are visible and are attributed to the remainders of the primary wall. The small round shaped features on the fiber surface are considered to be precipitated lignin. The dark surrounding is the hemicellulose matrix.

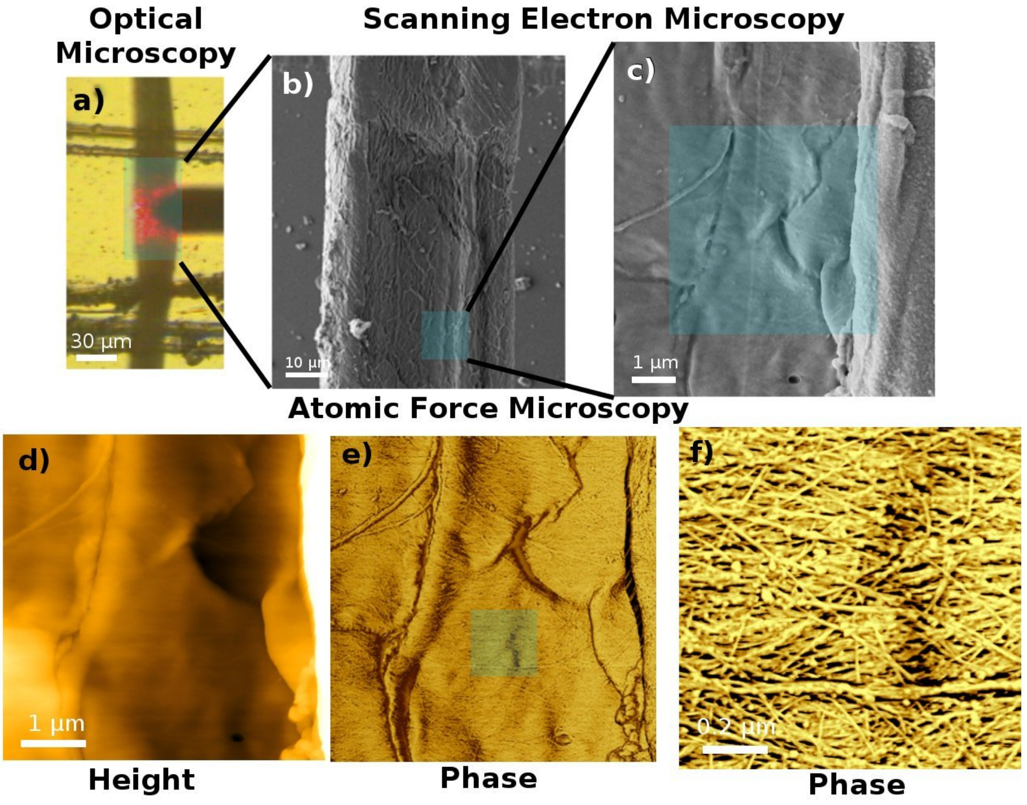

**Figure 4.1:** Different techniques applied on an industrial pulp. a) OM image, b) SEM image from the shaded area in a), c) higher resolved SEM image from the shaded area in c), d) AFM topography image from the shaded area in c), d) corresponding phase image from e), and f) high resolution AFM phase image from shaded area presented in e)

A closer look onto the surface morphology is presented in figure 4.2. Here, 3D plots of the fiber surface are presented which have been recorded by AFM and SEM, respectively. The AFM technique provides 3D information due to its probing principle. For SEM, an eucentric tilting of the stage is utilized to generate a stereoscopic image. Overlay techniques such as red-blue coloring provide an anaglyph viewing and thus depth perception, but again no quantitative height information. The technology of Alicona now automatically identifies points in each of the images that belong to the same point on the specimen. From these so called homologous points, the true three-dimensional coordinates of the observed point can be recovered. This demanding task is robustly solved for each pixel in each of the images and thus a dense 3D model of the specimen is obtained.

Both techniques show a good agreement in visualization of wrinkles and bending of the fiber surface. The presented images demonstrated that AFM phase imaging in tapping mode is suitable to investigate pulp fiber surfaces on the nanometer scale. Because of difficulties with imaging curved surfaces, it is not able to reveal information on a large area. On the other hand, SEM provides information on a large area but does not provide as high resolution as AFM. Therefore a combined investigation with both imaging techniques is desirable.

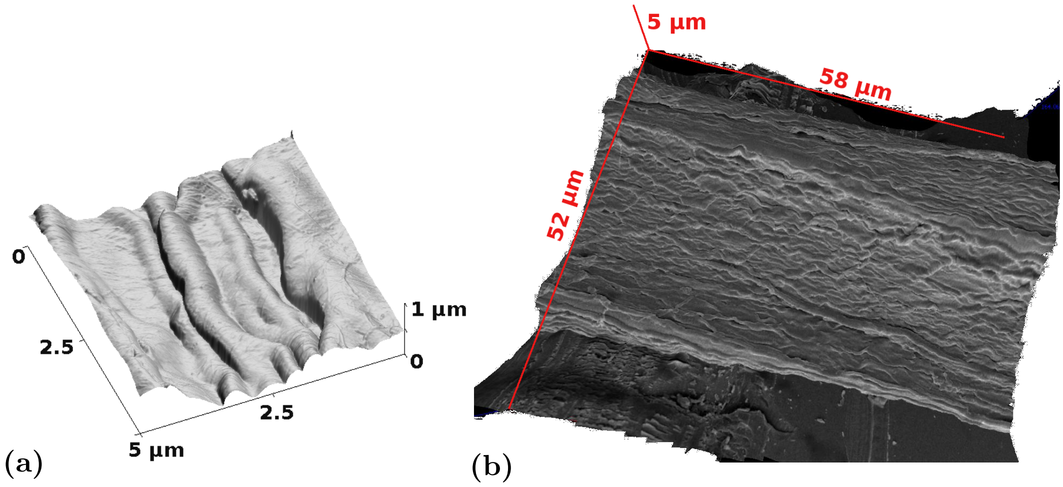

**Figure 4.2:** 3D plots of a) AFM height data and b) SEM data with eucentric tilting.

## 4.1.1 Microfibrils

Analysis concerning microfibrils of an industrial pulp are summarized in figure 4.3. Figure 4.3a represents a high resolution phase image of an untreated and unbleached industrial pulp. The calculated 2D-FFT is presented in (b). The observed split peak indicates a preferred orientation almost perpendicular to the main fiber axis. This finding proves that the surface under investigation represents the S1 wall. From the peak splitting in reciprocal space a center to center distance of the microfibrils of (50 ± 17) nm is determined. From the line section (see figure 4.3c), a mean fibril diameter is estimated to be (31 ± 6) nm. This value is smaller than the center to center distance from the 2D-FFT due to the fact that not all the fibrils touch each other.

The calculated phase distribution of the phase images reveals two clearly separated peaks. The peak between -30° and -40° is attributed to the darker hemicellulose matrix whereas the peak between 0° and 20° corresponds to the bright cellulose microfibrils. To determine the ratio between the cellulose microfibrils and the hemicellulose matrix, a cumulative phase distribution has been derived. Fitting the linear parts and determining the crossing point leads to a separation of the two distinct fractions and reveals

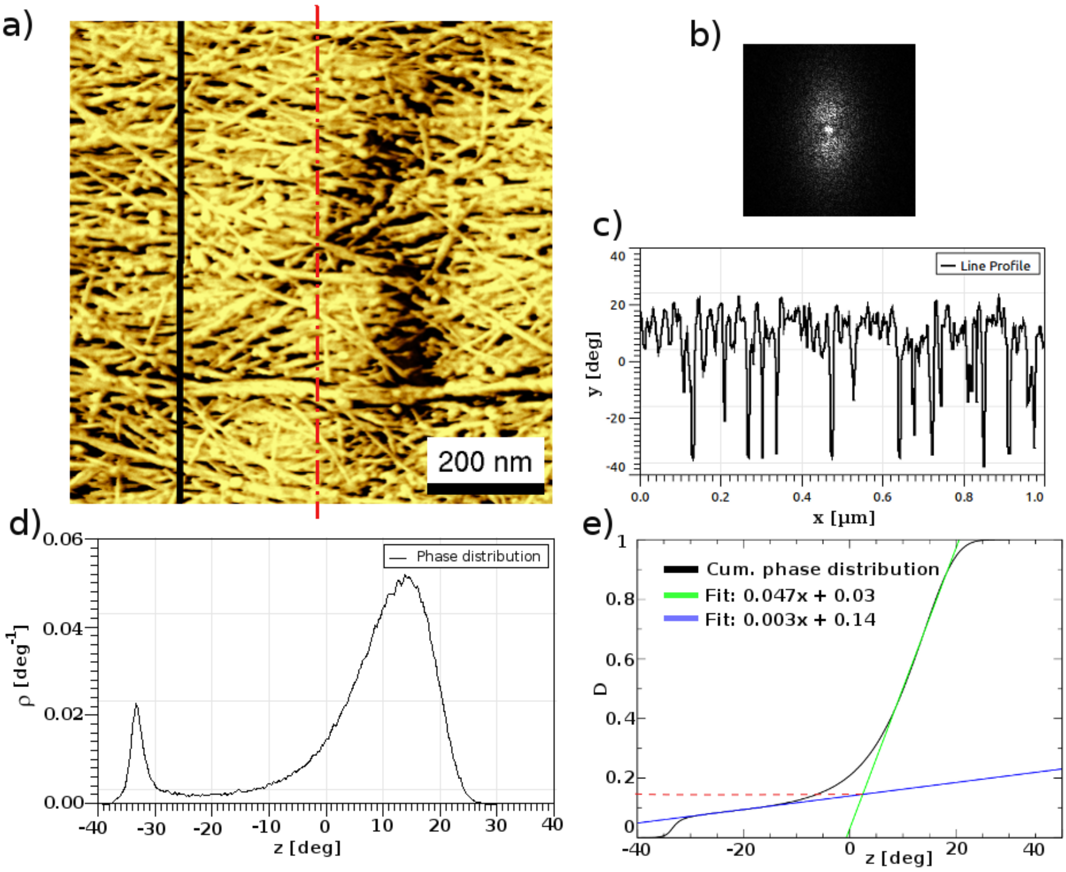

**Figure 4.3:** a) High-resolution phase image of an untreated and unbleached industrial pulp ($\phi$-scale=50°). The red dashed line marks the main fiber axis. b) 2D FFT calculated from a), c) line profile along the marked line in a), d) calculated phase distribution and e) corresponding cumulative phase distribution. Crossing of the blue and green lines revealed 85% of microfibrils on the surface.

a microfibril density of 85% on the fiber surface (see figure 4.3e). Taking into account that precipitates are visible on the surface, approximately 80% of the fiber surface is covered with microfibrils that have access to the bonding area. Counting the individual microfibrils resulted in about 250 microfibrils visible on a 1 $\mu$m x 1 $\mu$m scan. This estimation is just a rough number, because microfibrils that partly hide behind other fibrils might be counted twice.

To get access to the microfibrils on other cell wall layers, an enzymatic peeling experiment was performed. Here, the S1 layer is attacked and removed to reveal the S2 layer. As already mentioned in the introduction, here, the microfibril orientation should be parallel to the main fiber axis with a higher degree of ordering.

Figure 4.4 represents AFM data of an enzymatically attacked industrial pulp for 20 minutes. Here, the microfibril orientation is parallel to the main fiber axis (top-down). This is also reflected in the rotation of the split peak in the 2D-FFT (see figure 4.4b) compared to figure 4.3b which represents the S1 layer. The splitting of the 2D FFT a preferred center to center distance of (47 ± 11) nm is revealed. A manual analysis of the fibril width from line sections (see figure 4.4c) revealed a mean fibril diameter of (30 ± 8) nm. The granular features on the fiber surface are supposed to be remainders from the enzymatic attack with lateral sizes of 40 to 60 nm.

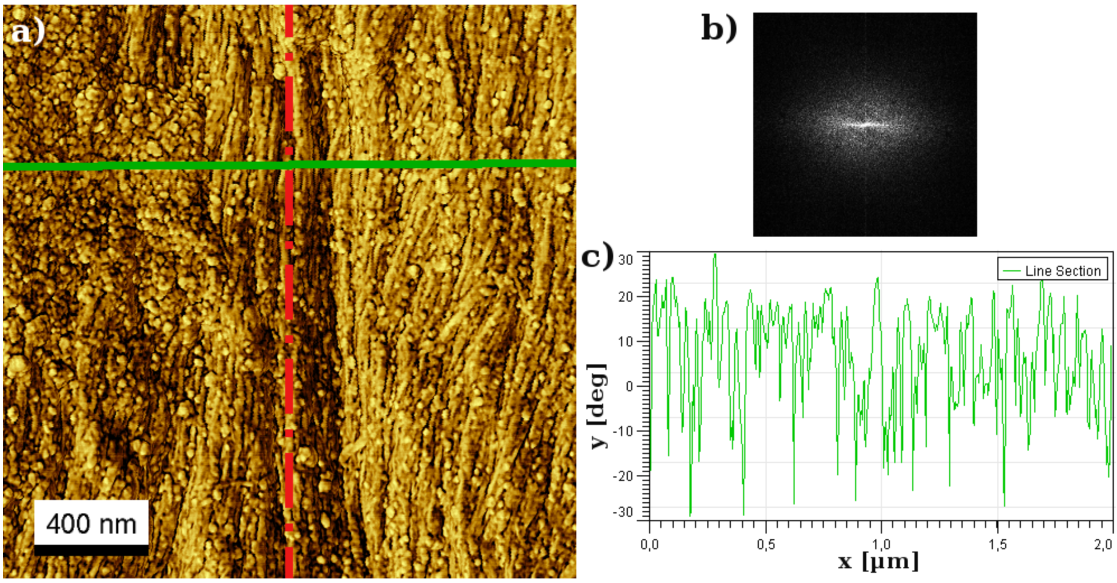

**Figure 4.4:** a) High-resolution phase image of an enzymatically attacked industrial pulp for 20 minutes ($\phi$-scale=50°). The red dashed line indicates the main fiber axis. b) 2D FFT calculated from a), c) line profile presented in a).

## 4.1.2 Lignin precipitates

In the pulping process, lignin is removed to such an extend that the yield is still high enough and hemicellulose is preferably not yet degraded. For comparison, the overall lignin content, given by the $\kappa$-number, of the different pulps is measured. Unfortunately, the $\kappa$-number is only an integral measure of the pulp sample, it does not yield specific information on the shape or distribution of the lignin particles on the fiber surface. In the following, a method for the analysis of precipitated lignin based on AFM phase imaging is introduced. It allows to statistically evaluate structural aspects, like distribution of the diameter of individual lignin spherules.

First, the results of two treated kraft pulp fibers are presented, serving as test samples. The black liquor cook is presented to show the precipitated lignin and to verify the presented method. The next paragraph will deal with the oxidized pulp where the precipitated lignin is removed. Finally, an overview of different treated pulps from $\kappa$-numbers between 8 and 73 summarizes the findings.

Figure 4.5 shows typical AFM phase images of a fiber highly treated by black liquor cook. Figure 4.5a is a 2µm x 2µm image. The shaded area in this image corresponds to the 1µm x 1µm scan, presented in Figure 4.5b with higher resolution. The $\kappa$-number of 73 corresponds to a very high amount of lignin and is approximately 10 % according to equation 2.1. The surface features which are more or less perpendicular to the main fiber axis are the cellulosic microfibrils of the S1 layer. For the image in Figure 4.5a, the fibrillar diameter was determined to be (27 ± 5) nm from the line profile analysis and a preferential center to center distance of the microfibrils of (40 ± 12) nm was obtained from the splitting of the 2D FFT as mentioned previously. The round shaped features - visible in figure 4.5 - are representing the precipitated lignin. This analysis based on watershed algorithm (compare to figure 3.18) of the precipitated lignin (presented in figure 4.6a) leads to an identification of almost 200 individual precipitates. The equivalent disc diameter, obtained by a Gaussian fit, of the precipitated lignin is (26 ± 5) nm.

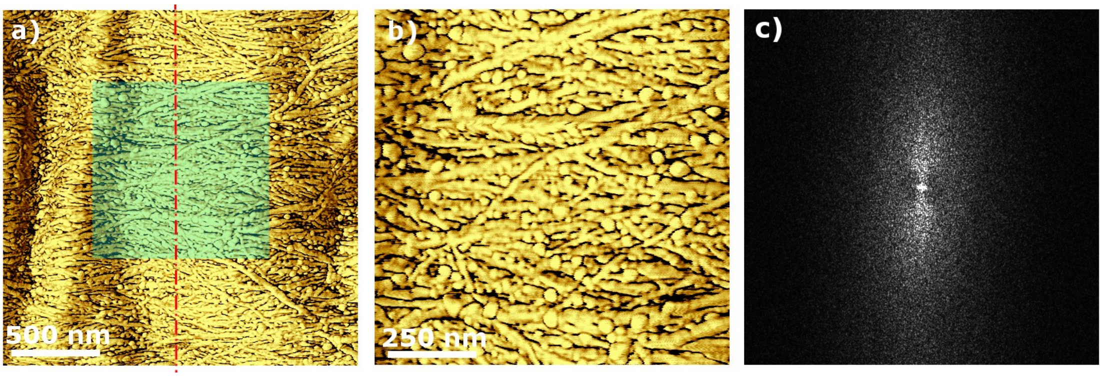

**Figure 4.5:** High-resolution AFM phase image of a black liquor cook treated pulp fiber. The shaded area in a) corresponds to the image presented in b). The red dashed line indicates the main fiber axis. $\phi$-scale=50°. c) 2D FFT calculated from a)

For comparison, a manual analysis of 6 features resulted in a feature diameter of (31 ± 15) nm. Calculating a surface coverage with lignin from the counts and the determined disc diameter leads to a value of 2.4 %. The amount calculated from the macroscopically determined $\kappa$ number is 10 % which is 4 times higher. The main reason for this difference is that only small precipitates on smooth areas are analyzed. Another important factor is the lack of information on the precipitate's thickness in order to calculate the complete volume fraction of the precipitates. Figure 4.6b presents a reference calculation from figure 4.5b which is a phase image of the shaded area in figure 4.5a with higher resolution. The analysis of the plot results in a similar value for the mean disc diameter (24 ± 9) nm and demonstrates that the introduced procedure does not depend on the image resolution. Therefore, in combination with the features measured manually, the procedure can be considered as reliable.

To cross-check the evaluated data, a combined AFM-SEM investigation was per-

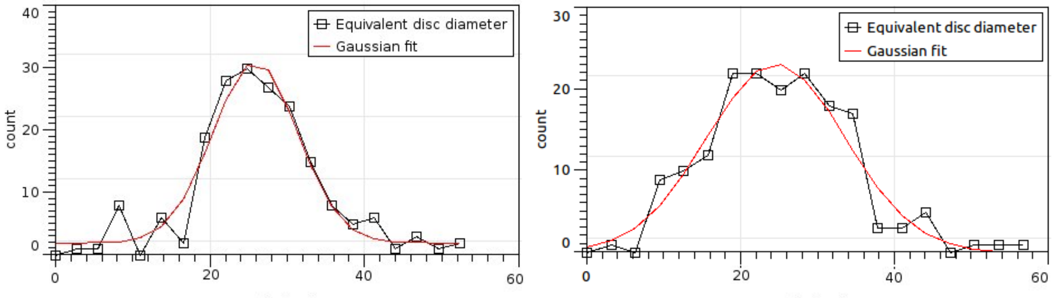

**(a)** **(b)**

**Figure 4.6:** Distribution of disc diameters and corresponding Gaussian fit of a) figure 4.5a and b) figure 4.5b.

formed. In addition to standard tapping mode AFM imaging close to the first resonance frequency, DualAC mode was utilized and higher harmonic images were analyzed. Figure 4.7 summarizes AFM images of a fiber treated with black liquor cook and an SEM image of the same position revealing information on a larger scale. An AFM topography overview image is provided in figure 4.7a. It is used as identification point for the SEM image. The black dashed line indicates the main fiber axis. The shaded area emphasizes the area of the AFM images presented in figure 4.7b-f. Figure 4.7b is a topography image recorded with higher resolution. The feedback signal and first amplitude is presented in figure 4.7c and the corresponding phase image of the prime frequency is presented in 4.7d. The second flexural harmonic images reveal a higher contrast than the images taken from the prime frequency. The phase image of the second frequency (see figure 4.7e) shows the same features as in figure 4.7d, but with a larger $\phi$-scale ($\phi_{1^{st}}$=20°, $\phi_{2^{nd}}$=70°). The second amplitude revealed the best image contrast and is presented in figure 4.7f. Here, both - microfibrils and lignin precipitates - are clearly visible. Figure 4.7g represents an SEM image of the corresponding fiber surface. Besides the small precipitates revealed with AFM also larger precipitates are visible. The typical diameter of these larger lignin precipitates is 100 nm to 1000 nm and are exemplarily marked by red circles in the SEM image (figure 4.7g). Information from the SEM images further reveals a non-homogeneous distribution of the lignin particles in two ways. First, the large particles are irregularly distributed on the fiber surface and are preferentially arranged close to rough surface features - such as wrinkles and pits. Therefore, in high-resolution AFM images - taken from smooth areas - only small precipitates are visible. Second, the SEM images reveal a bimodal distribution of lignin precipitates with a diameter of 0.1-1 µm and lignin particles smaller than 100 nm. The smaller particles are marked by green circles in figure 4.7g.

Analyzing on both length scales with complementary techniques reveals a more comprehensive look on the surface of treated pulp fiber . On the black liquor cook treated pulp, a lot of precipitates are visible on different length scales. In the AFM image, only small precipitates with a diameter of ∼40 nm are detectable. Whereas the SEM image

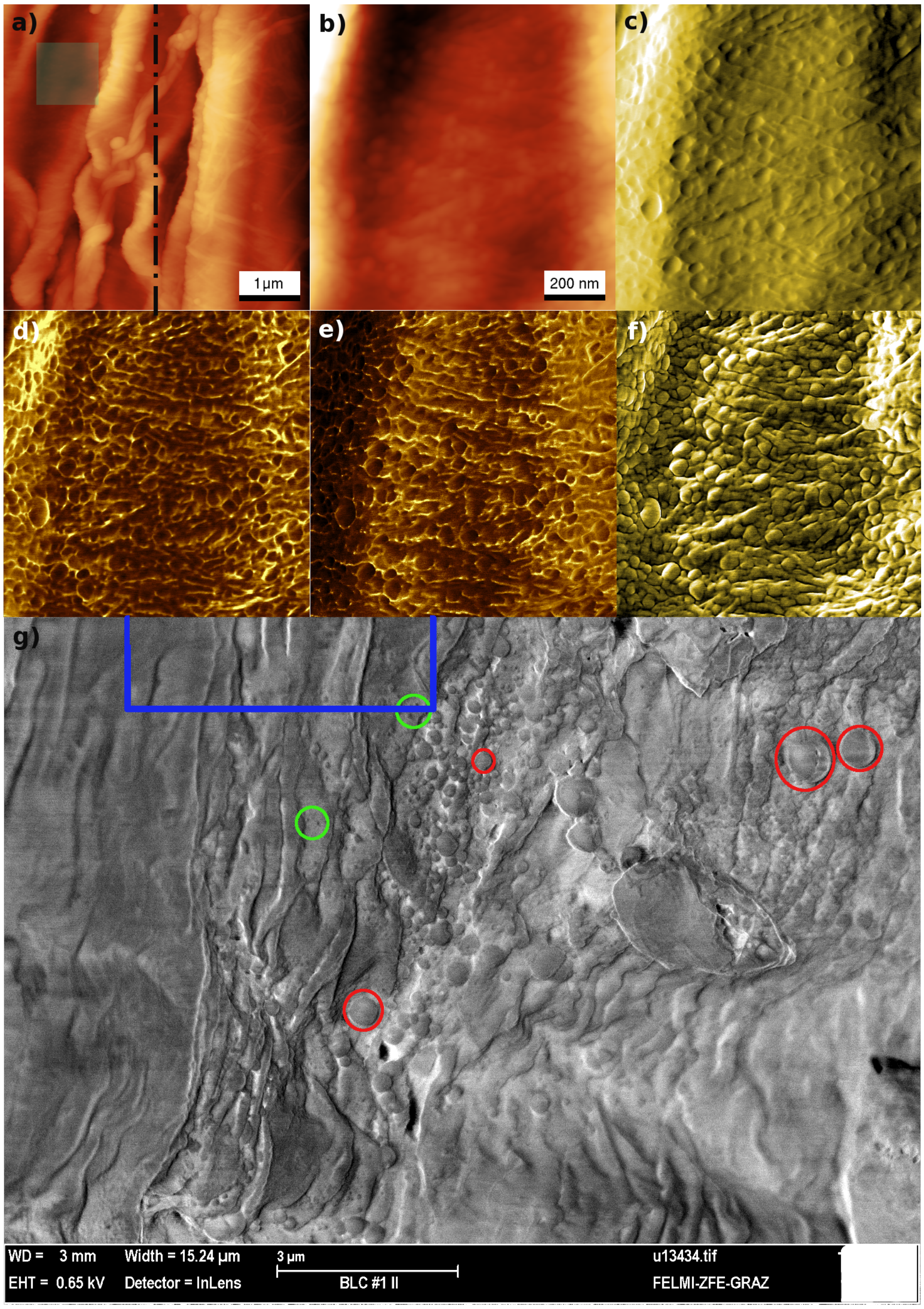

**Figure 4.7:** Black liquor cook treated pulp fiber ($\kappa$ number = 73) measured in DualAC AFM technique and SEM. a) AFM topography image (z=1000nm). The dashed line indicates the main fiber axis. b) High-resolution AFM topography image from the area marked in a) (z=300nm, c) corresponding first amplitude image (z=30nm) of b), d) corresponding first phase image ($\phi$=20°) of b), e) corresponding second phase image ($\phi$=70°) of b), f) corresponding second amplitude image (z=10nm) of b), and g) SEM image (Inlens, 0.65keV, uncoated). The blue frame marks the investigated AFM area. The circles are explained in the text.

exhibits both, larger (∼ 1µm) and smaller precipitates (<100 nm) inhomogeneously distributed all over the fiber surface.

Figure 4.8 represents AFM phase images of a highly oxidized fiber with a $\kappa$-number of 6. The microfibrils have a typical diameter of (32 ± 4) nm and were determined via line profile analysis. From the 2D FFT splitting a value for the center to center distance of (70 ± 30) nm has been obtained. The large error bar is due to the little uniformity of the microfibrils. The preferred orientation of these microfibrils is mostly perpendicular to the main fiber axis and the layer is considered to be the S1 layer. In the 2µm x 2µm (figure 4.8a) image, no precipitated lignin is visible. Even the 1µm x 1µm image (figure 4.8b) shows only a few small precipitates with diameters lower than 15 nm. Due to the small amount of lignin it was not possible to achieve a reasonable statistics with the watershed analysis.

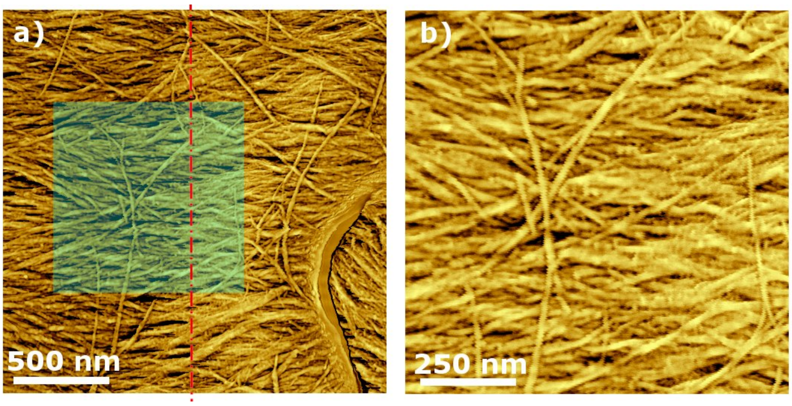

**Figure 4.8:** AFM phase images of an oxidized pulp fiber. The shaded area in a) responds to that of the image presented in b). The red dashed line indicates the main fiber axis. $\phi$-scale=50°.

Figure 4.9 represents AFM investigations in bimodal DualAC mode and a corresponding SEM image including the same surface region. The AFM images represent clearly the microfibrils, but almost no lignin precipitates are visible on the fiber surface. The second amplitude image (see figure 4.9f) is the image with the highest contrast and reveals 4 particles with a diameter of ∼40 nm and the elongated microfibrils. Figure 4.9g presents an SEM image taken including the same position. In contrast to the image presented in figure 4.7g, almost no precipitates are visible on the oxidized pulp (few particles are marked by green circles exemplarily).

Figure 4.10 summarizes statistical data evaluated from pulps with different $\kappa$-numbers ranging from 8 to 73. Typical AFM phase images of the treated pulp fiber surface are presented in figure 4.10a-e. The main fiber axis is always top-down oriented and is indicated by the red dashed line presented in figure 4.10e. For all the phase images, the microfibrils are perpendicular to the main fiber axis except for figure 4.10d. Here, the image position is close to a pit and therefore the microfibrils are circularly arranged (see section 4.1.4). Figure 4.10f represents the calculated diameter of the lignin precipitates

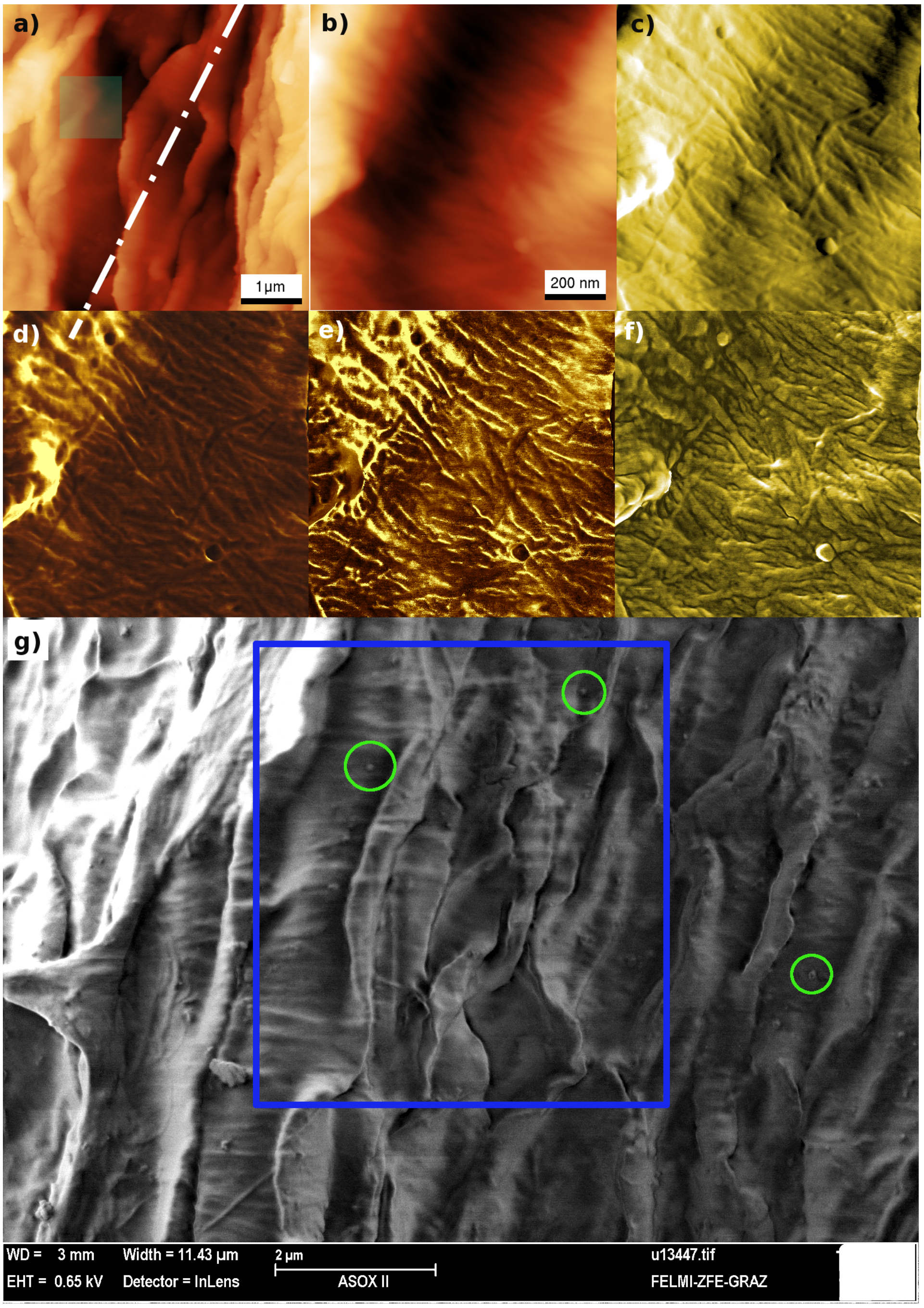

**Figure 4.9:** AFM phase images of an oxidized pulp fiber measured in DualAC technique and corresponding SEM. a) AFM topography image (z=1500nm). The dashed line indicates the main fiber axis. b) AFM topography image from the area marked in a) (z=250nm, c) corresponding first amplitude image (z=20nm) of b), d) corresponding first phase image ($\phi$=20) of b), e) corresponding second phase image ($\phi$=50°) of b), f) corresponding second amplitude image (z=10nm) of b), and g) SEM image (Inlens, 0.65keV). The blue frame marks the investigated AFM area. The green circles mark lignin precipitates.

versus the $\kappa$-number. Here, black liquor cooked fibers show a larger precipitation diameter than oxidized pulps. A closer look on the standard deviation of the corresponding distribution is presented in figure 4.10g and describes a narrower precipitation diameter distribution with an increased treatment for the black liquor cook as well as for the oxidation treatment. For comparison to the data presented by Simola-Gustafsson et al. [27] on delignified kraft pulp, the evaluation of the mean value of the phase lag was plotted versus the $\kappa$-number (see figure 4.10h) and revealed similar mean values of the phase shift. Both data sets presented in figure 4.10h have been measured at nearly the same humidity (18-22%). Comparative measurements at higher humidity in our laboratory show a tremendous influence on the mean value of the phase lag to more positive values. Assuming circular footprints of the lignin precipitates, the surface coverage $\Theta_{surf}$ can be estimated as

$$\Theta_{surf} = \frac{d^2 * \pi}{4} * N * \frac{1}{A} \tag{4.1}$$

where d, N, A are the diameter of the lignin precipitation, the number of identified particles and the scanned area.

Figure 4.10i represents the lignin surface coverage as a function of the $\kappa$-number. Evaluation of the data was performed with a lateral masking procedure and therefore, the height information got lost. Due to a volume increase of the lignin particles on the fiber surface with raising $\kappa$-number and a detection of the particle diameter from a two-dimensional image analysis a non-linear dependency is expected. The power-law fit presented in figure 4.10i predicts an exponent of approximately 1.5. The scattering of the data is attributed to the following missing information. First of all, the determined diameter of the precipitates is only accessed from the smoothest areas to achieve sufficient resolution. As discussed earlier, larger lignin precipitates are preferentially situated close to rough surface features and are thus underrepresented in the AFM phase images recorded on smooth surface regions. Second, not all of the particles are detected by the watershed algorithm resulting also in a lower coverage. Nevertheless, the increase in lignin on the fiber surface with increasing $\kappa$-number is visible. It has to be stated that the determined value of the surface lignin is significantly lower than the expected value from the $\kappa$-number after equation 2.1 due to an incomplete detection of all the precipitates. According to Simola-Gustafsson et al. [27], the amount of surface lignin is considered to be higher than the bulk value represented by the $\kappa$-number which increases even more the discrepancy. Nevertheless, the quantitative analysis of such precipitate size distributions might provide a useful tool to investigate the kinetics and structure of lignin precipitation in different process steps of the kraft pulping process.

### 4.1.3 Hornification

Hornification occurs during the drying process of fibers [77] and is irreproducible, i. e., it is not vanishing after rewetting. It represents a loss of pulp swelling. It has therefore significant influence on fiber-fiber bonding due to the loss of flexibility which is

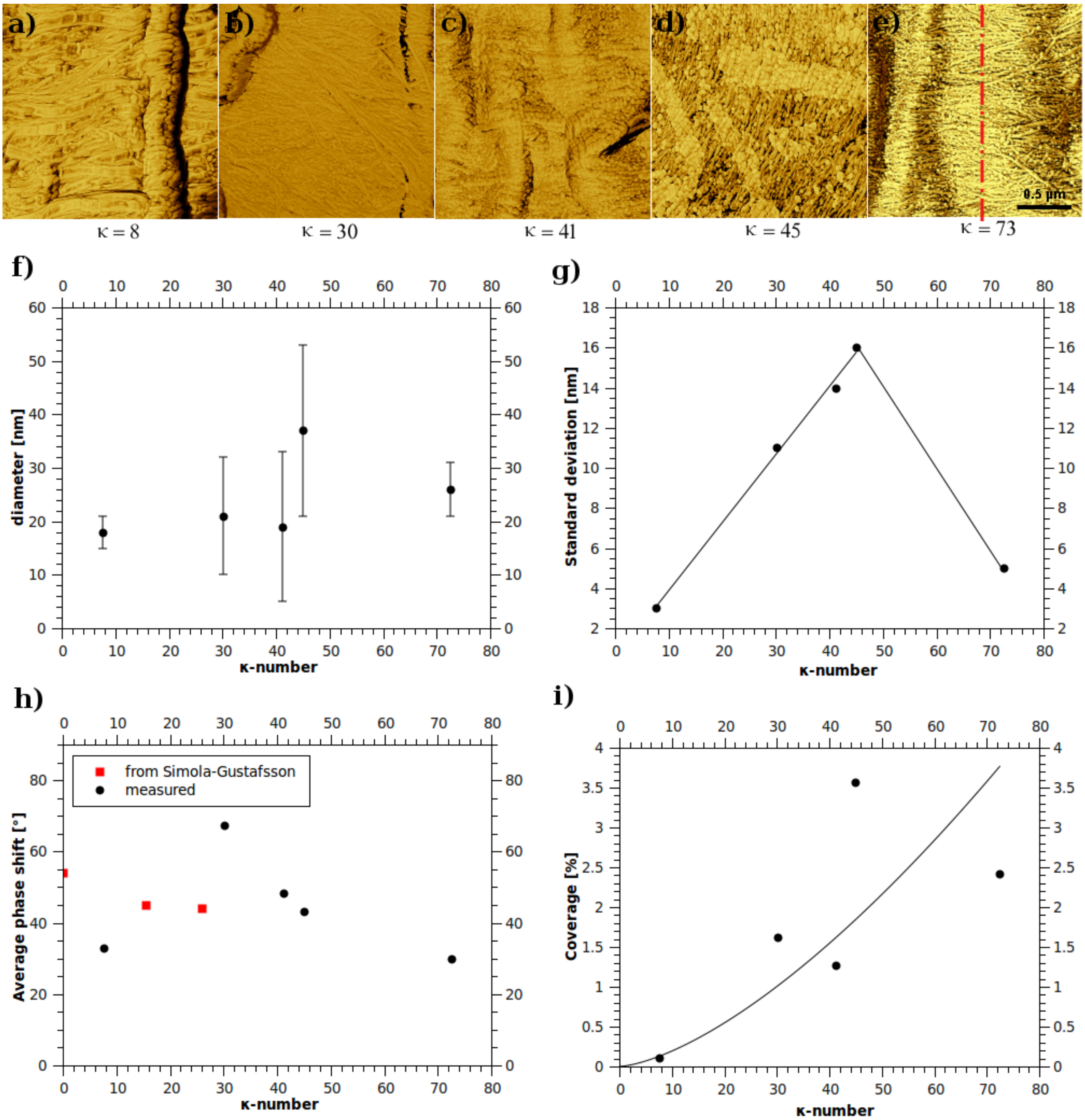

**Figure 4.10:** Summary of precipitation analysis of differently treated pulps with a $\kappa$-number ranging from 8-73. a-e) 2 $\mu$m x 2 $\mu$m AFM phase images of fibers with different $\kappa$-numbers. $\phi$-scale=50°. f) Diameter of precipitation versus $\kappa$-number, g) Standard deviation of precipitation diameter versus $\kappa$-number, h) Mean value of the phase lag versus $\kappa$-number together with data from delignified pulp [27], and i) lignin coverage versus $\kappa$-number.

necessary to approach two fibers close enough to form a bond. Figure 4.11 shows an AFM image of a kraft pulp fiber with a hornification in the highlighted region. A wrinkled surface is visible with a surface area in the lower left corner where material is protruding. Here, a high density of wrinkles is observed, resulting in clear morphological difference to the rest of the fiber surface. These areas are attributed to hinder swelling. Thus, they result in less bonds due to a loss of fiber conformabilty. Besides this physical change, it has been suggested that hornification is an esterification process of interlocking lignocellulosic chains [78].

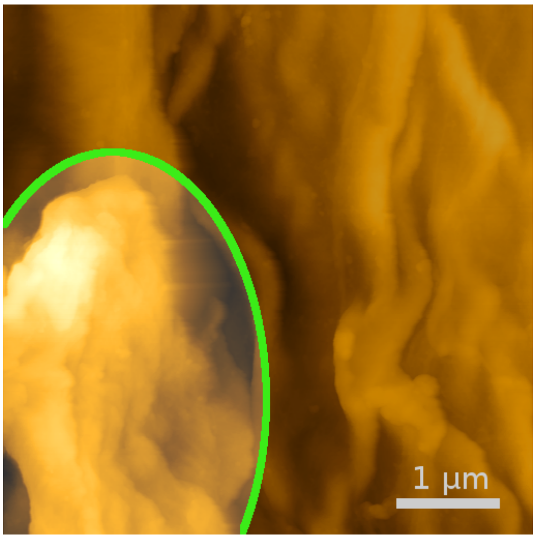

**Figure 4.11:** AFM topography image of a hornification (marked by the green line) on the fiber surface.

## 4.1.4 Pits

Pits are valves connecting two neighboring wood fibers. This connection is necessary to achieve the transport of water and nutrients from the roots to the top of the tree. Figure 4.12 represents a 3D plot of an AFM topography image. The diameter of the more or less circular pit is $\sim 5$ µm and the depth of the pit is $\sim 2$ µm. A closer look into the pit reveals wrinkles on the visible underlaying S1 layer. Another interesting fact is the arrangement of the microfibrils around the pit in the P layer. As can be seen in the 3D plot (figure 4.12b), the microfibrils change their preferred orientation perpendicular to the main fiber axis to a circular orientation around the pit [79]. This is an interesting trick of nature to reduce strain around defects on the fiber surface [80]. On a macroscopic scale, a similar phenomenon is observed around a knothole of a tree.

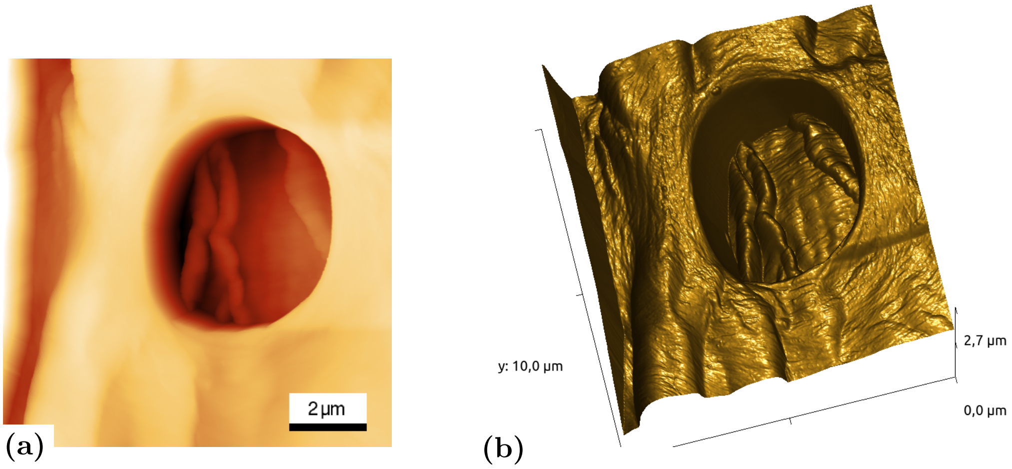

**Figure 4.12:** AFM topography image of a pit in a cellulose fiber. a) Height image (z-scale=2.5 µm), and b) 3D plot of a).

## 4.1.5 Stitched AFM images

As mentioned in the beginning of this section, AFM provides information on the nanoscale but has the drawback to provide this high resolution only on a restricted area. Due to the rough surface of the cellulose fibers and the fiber curvature, the maximum accessible area is 20x10 µm$^2$. SEM, on the other hand, allows scanning of larger areas, but cannot provide this high resolution to visualize the individual microfibrils and lignin precipitates down to the nanometer scale. Therefore, AFM image series were measured and stitched together in a post-processing step with an image manipulation program [74]. This allows to scan larger areas - as the formerly bonded area - with sufficient resolution to observe morphological changes. One has to note that this method unfortunately consumes a lot of time. The effort, however, will yield new insights into the fiber-fiber bonding mechanisms as will be clearly demonstrated in the following.

### Unbonded area

As unbonded area a typical position on the pulp fiber surface has been chosen where no bonding occurred before. A stitched AFM overview is presented in figure 4.13. The first feature that is immediately recognizable, is the wrinkled surface appearance all over the pulp fiber (compare also to figure 4.2). The wrinkles on the fiber surface result from the drying process and are not present on wet fibers. This surface feature leads to a high surface roughness with a typical rms-roughness $\sigma$ of $(280 \pm 120)$ nm for a 20 $\mu$m x 10 $\mu$m scan. From the AFM height images, the true surface area of that unbonded area is calculated to be $(237 \pm 7)$ µm$^2$ for a 20 $\mu$m x 10 $\mu$m scan. According to the projected area of 200 µm$^2$ this leads to a Wenzel ratio of 1.18. With other words, the true surface area of the unbonded region is 18 % larger than the projected surface area. This increased surface area is mainly caused by the wrinkles on the surface and larger lateral height fluctuations as represented in the line profile in figure 4.13b.

An additional increase of the Wenzel ratio is provided by the fiber curvature and is approximately 1 %. The table in figure 4.13c summarizes the data for the stitched AFM topography image presented in figure 4.13a.

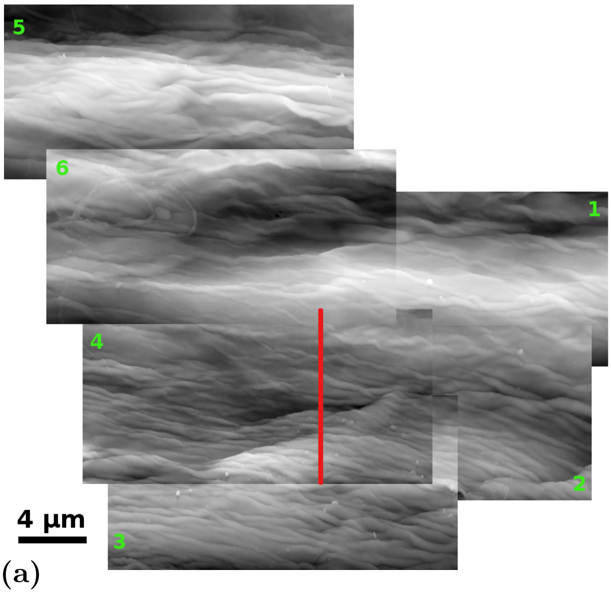

(a)

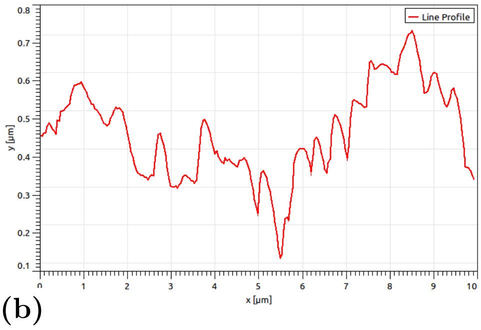

(b)

| Image | rms [nm] | True surface area [$\mu$m$^2$] | Wenzel ratio |
|---|---|---|---|
| 1 | 391 | 236 | 1.17 |
| 2 | 156 | 229 | 1.14 |
| 3 | 276 | 245 | 1.21 |
| 4 | 126 | 230 | 1.14 |
| 5 | 318 | 236 | 1.17 |
| 6 | 417 | 243 | 1.20 |
| Avg | 280 ± 120 | 237 ± 7 | 1.18 ± 0.03 |

(c)

**Figure 4.13:** a) Stitched AFM topography images of an untreated and unbleached industrial pulp on a randomly chosen position of the fiber surface, b) corresponding height profile along the red line presented in a), and c) summary of obtained data from a).

## 4.1.6 Formerly Bonded Area

Figure 4.14 shows two stitched AFM topography images of an unbleached, formerly bonded industrial pulp fiber revealing the formerly bonded area (FBA). The FBA shows a different appearance than the non-bonded area. Comparing figures 4.13 and 4.14 one can clearly distinguish between these two different surfaces. In contrast to the non-bonded area, the FBA reveals a smoother surface which shows barely any wrinkles which are observed on the non-bonded area as discussed in section 4.1.5. This different surface appearance allows distinguishing bonded and unbonded areas in the stitched topography images. In figure 4.14 the transition zones are marked to guide the eyes. In between these marks, the FBA is situated. Beside the smoother surface appearance, dangling microfibrils are visible, especially close to the transition zone. Outside these marks, the image shows the surface of the unbonded region. Figure 4.14b shows pit regions right of the FBA.

After identifying the formerly bonded region it is possible to calculate the FBA either by multiplying the distance of the marks times the fiber width. This is a method based on the geometric parameters fiber width and crossing angle (typically 90°) [43]. A more precise method is counting each pixel inside the marks (see table 4.1). The revealed data are in good agreement with the values determined by microtomy or PLM [81]. In contrast to the projected bonded area determined by these techniques, the AFM data can even provide the true surface area of the FBA. Analysis of the data revealed a Wenzel ratio of 1.06-1.08 for the FBA. This ratio between projected and true FBA is in good agreement with data presented by Swanson and Steber [82]. Here, they determined a 4-5% larger surface area for the bonded region by BET of different pulps. In comparison to the data obtained from the unbonded area, the increased true surface area of the FBA is less than half times larger.

It has to be stated that the true surface area is not the area in molecular contact after a bond is formed. Based on sliding friction theory [68] the area of molecular contact of two steel bodies is $10^5$ times smaller than the projected bonded area. Calculations for a fiber-fiber bond, using standard conditions of a sheet former, lead to an area in molecular contact of 0.5 $\mu m^2$. Compared to the projected bonded area of about 1500 $\mu m^2$ this is 3000 times smaller. According to [83] the area in molecular contact is linked to the optical bonded area.

Besides these differences in surface roughness, the appearance of dangling microfibrils is a striking feature of the FBA. Especially, close to the transition zone, an increased amount of these dangling microfibrils is present. This fact proves that these fibrils act as mechanisms for mechanical interlocking or fibril bridging. Figure 4.15 presents higher resolved AFM images of a single dangling microfibril. The topography image is illustrated in figure 4.15a and shows one single microfibril protruding from the surface. Due to the flexibility of the dangling fibril it is pushed forth and back by the AFM tip. Therefore, the signal for the phase imaging feedback is lost (see figure 4.15b).

Dangling fibrils inside the FBA are considered to be indications for mechanical interlocking or fibril bridging. Since these dangling microfibrils are protruding, easy counting is possible. About 30 protruding fibrils have been found for a bonded industrial pulp analyzing just three bonds. A summary of the acquired data from figure 4.14 and from figure 4.43 is presented in table 4.1.

| Figure | l x w [$\mu$m] | FBA [$\mu m^2$] | Dangling microfibrils | $\frac{\text{Dangling fibrils}}{\text{Bonded Area}}$ |
|---|---|---|---|---|
| 4.14a | 58 x 32 | 1958 | 25 | 0.013 |
| 4.14b | 33 x 42 | 1363 | 32 | 0.023 |
| 4.43a | 13 x 48 | 935 | 28 | 0.030 |

**Table 4.1:** Data acquired from industrial pulp.

Refining or beating is one treatment which significantly influences the paper strength. Figure 4.16 presents literature data for the dependence of tensile strength on the number of revolutions for three different pulps. The reasons for this increase are fibrillation, increase of fiber flexibility, and bonded area. Kappel et al. showed with microtomy that for a highly beaten pulp the bonded area is increased by 45 % [84]. Furthermore, also the degree of bonding is increased from 86% to 98%. This yields to a further increase of paper strength.

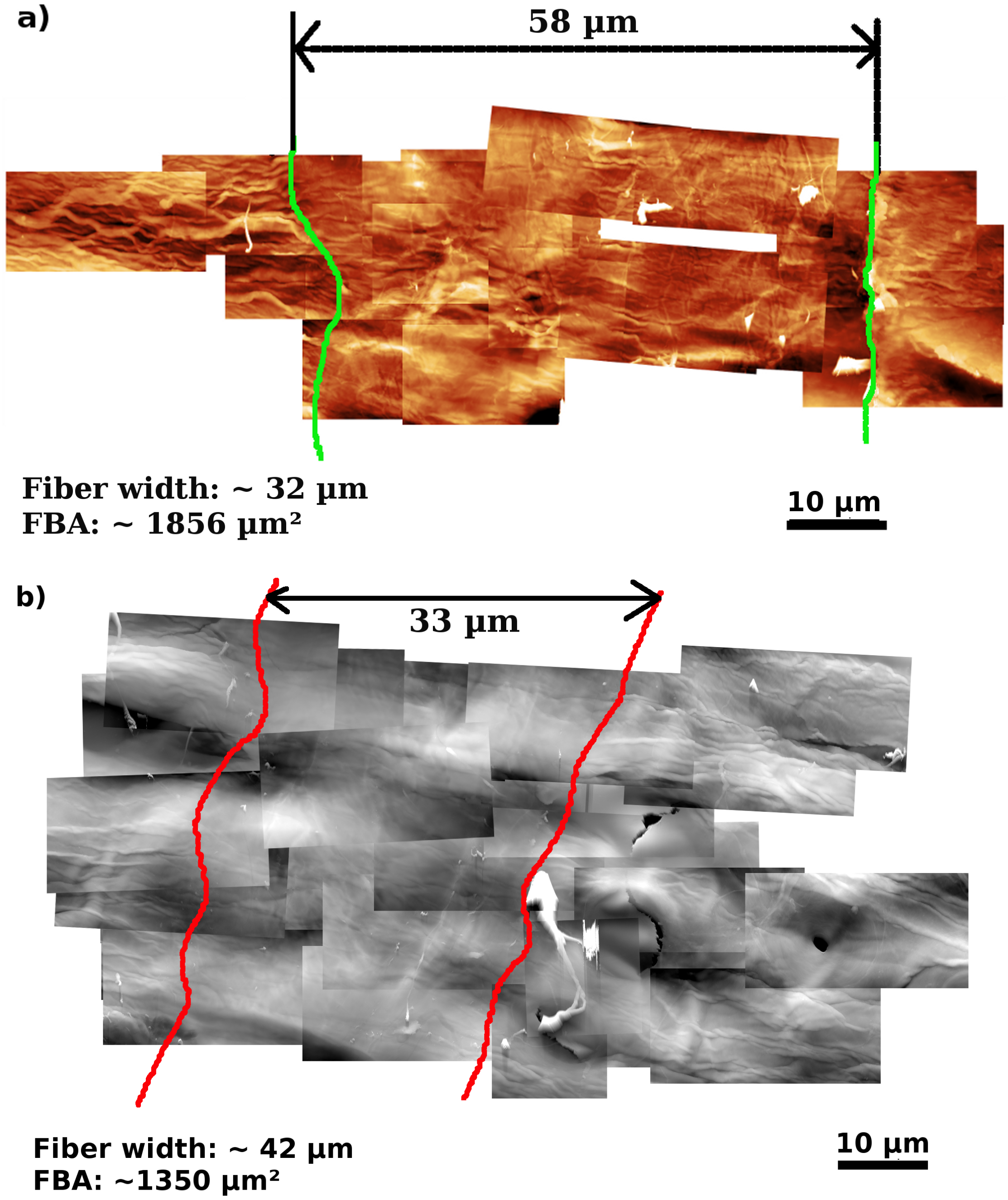

**Figure 4.14:** Stitched and aligned AFM topography image reconstructions of a formerly bonded area of two industrial pulp fibers a) and b). z-scale: 1 µm. The guide lines are marking the transition region between bonded and unbonded area.

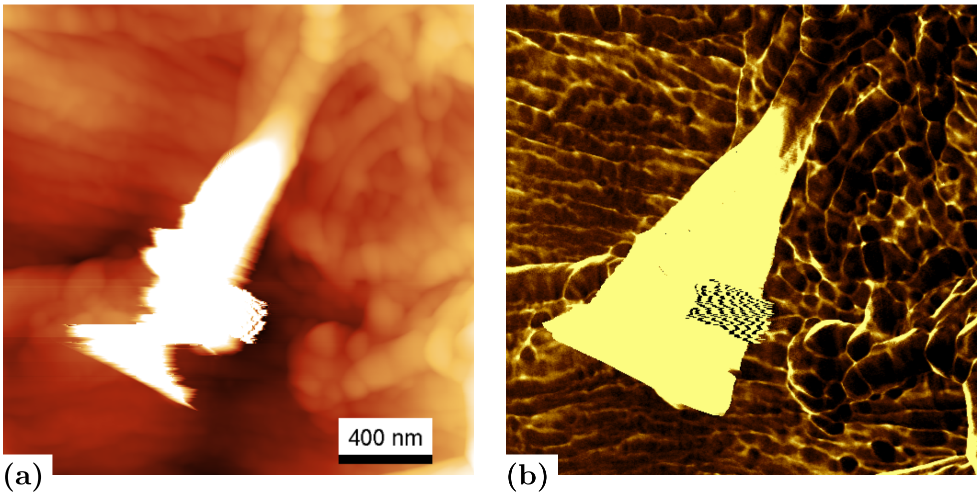

**Figure 4.15:** 2x2 µm AFM image of a single dangling microfibril. a) height image and b) corresponding phase image.

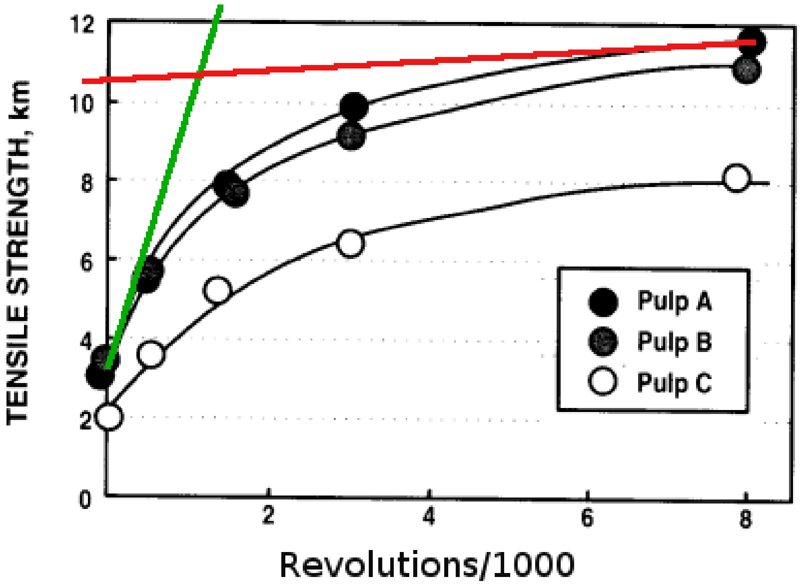

**Figure 4.16:** Influence of beating on the tensile index of three different softwood pulps. Green line: fibril bridging, red line: fiber conformability. A+B: northern species, C: southern species. (After [85].)

Figure 4.17 represents the stitched FBA of an industrial pulp moderately refined by 2000 revolutions in a PFI mill (compare to figure 2.10). Here, the FBA looks completely different than the bonded area of the unrefined pulp. First of all, bridging fibrils connecting two formerly bonded cell walls (see e.g. blue arrows in figure 4.17) are visible. Counting resulted in more than 50 bridging fibrils for figure 4.17. Beside these bridging elements, complete outer layers (P or S1 layers) are delaminated from the fiber surface (see yellow shaded area in figure 4.17). The presence of wall delamination already at moderate beating leads to two competing mechanisms. First, bridging fibrils increase the strength of the fiber-fiber bond itself. After a certain amount of fibril bridges have been formed, the bonding strength between the S1 layers of the different fibers becomes stronger than the bonding strength of the individual layers (S1 to S2) of one fiber. Therefore, the strong increase for lower beating becomes less pronounced for higher degrees of beating. The second mechanism is attributed to the increased fiber conformability. A higher fiber conformability results in a higher degree of bonding and therefore increases the tensile index of a paper sheet [86].

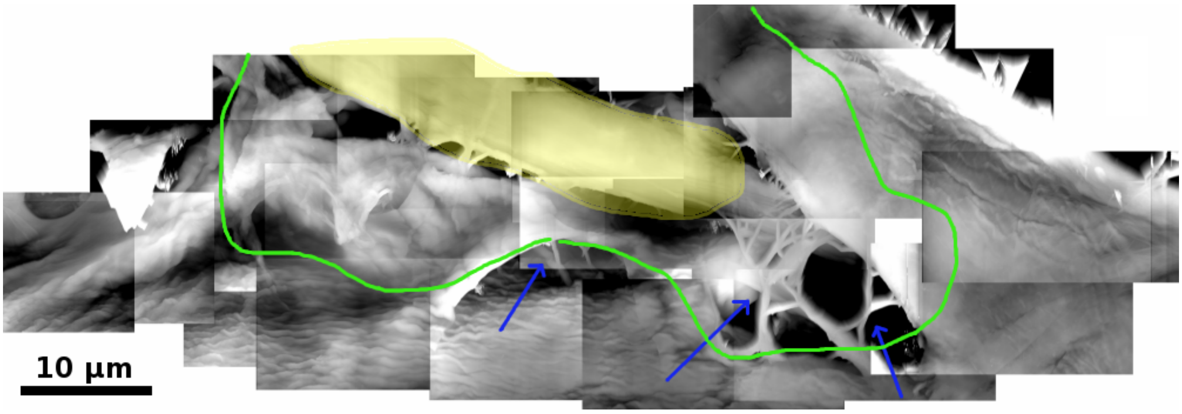

**Figure 4.17:** Stitched AFM topography image of the formerly bonded area of industrial pulp refined by 2000 PFI. The formerly bonded area is emphasized by a green line. The yellow shading marks a delaminated cell wall layer. Blue arrows are pointing to some of the fibril bridges.

## 4.2 Cross-sectional investigations

This section represents AFM investigations of cross-sections of fibers. Beside cross-sections of individual fibers, also those of fiber-fiber bonds, as well as cross-sections through a paper sheet are investigated. Furthermore, first results of KPFM of fiber cross-sections are presented.

### 4.2.1 Single fibers

Figure 4.18 represents an AFM image of a fiber cross-section. Here, the individual cell walls are clearly visible. They are marked in the phase image (figure 4.18b). The thickness of the individual layers are (250 ± 70) nm for P, (250 ± 70) nm for the S1, 4 to 5 $\mu$m for the S2, and (250 ± 70) nm for the S3. This measured data are in good agreement with values found in the literature (P: 0.2 $\mu$m, S1: 0.15 $\mu$m, S2: 5 $\mu$m, S3: 0.15 $\mu$m) [87].

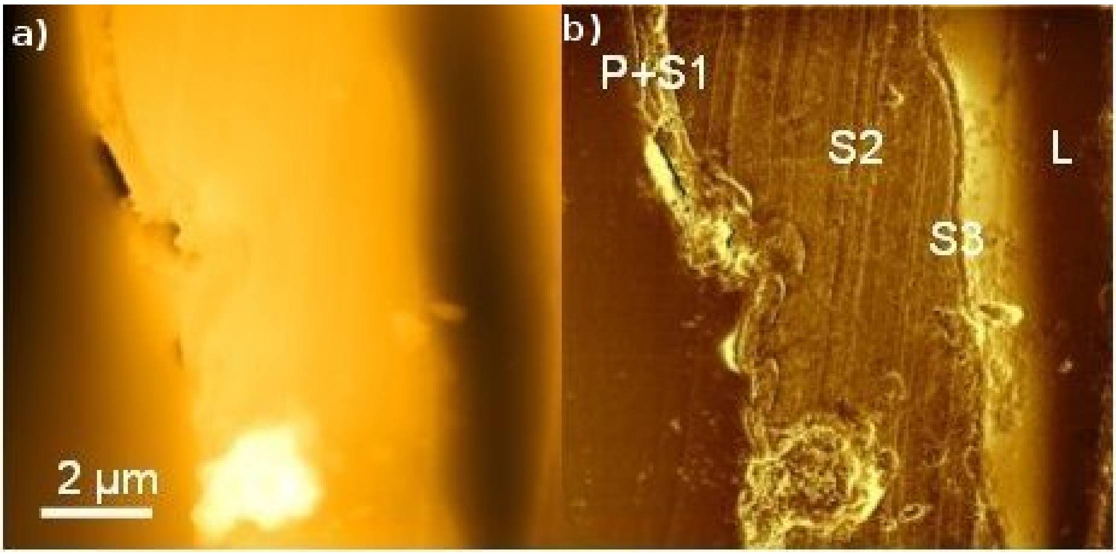

**Figure 4.18:** Cross-sectional sample of a single fiber. a) AFM height image (z-scale: 1.5 $\mu$m) and b) corresponding phase image ($\phi$-scale=20°). P - primary wall, S1 - secondary wall 1, S2 - secondary wall 2, S3 - secondary wall 3, L - lumen.

Further investigation of single fibers were performed in order to study, why some fiber cross-sections appear darker in the OM images and others do not. Figure 4.19 presents a comparison of the OM data with the corresponding AFM topography image. In figure 4.19a, two single fibers are visible (labeled with 1 and 2) and the AFM cantilever is placed on the lower one (fiber marked as 2). The inset represents an OM image taken from the microtomy OM of the lower fiber. The corresponding AFM topography image from the highlighted region in figure 4.19a is presented in figure 4.19b. AFM investigation on these cross-sections revealed that the fibers which are appearing dark are cluttered with cracks. Here, cracks ranging from the outer wall to the collapsed lumen. The clearly visible cracks are perpendicular oriented to the microtomy cutting direction. Further investigation of the phenomena figured out that only fibers which run upwards (see figure 4.19c, fiber 2) are showing this behavior. Fibers, that run downwards (fiber 1 in figure 4.19) or lying horizontally are not showing any cracks. The crack propagation is attributed to induced strain from the microtomy cutting direction which was here a bottom-up movement. This is clearly visible in the AFM images, but is hard to identify this in the OM images. Beside these cracks, a delamination from the resin is observed on the upper fiber part due to an energy release after microtome cutting (see inset in figure 4.19a). Thus, there is an uncertainty in determination of bonded area based on OM.

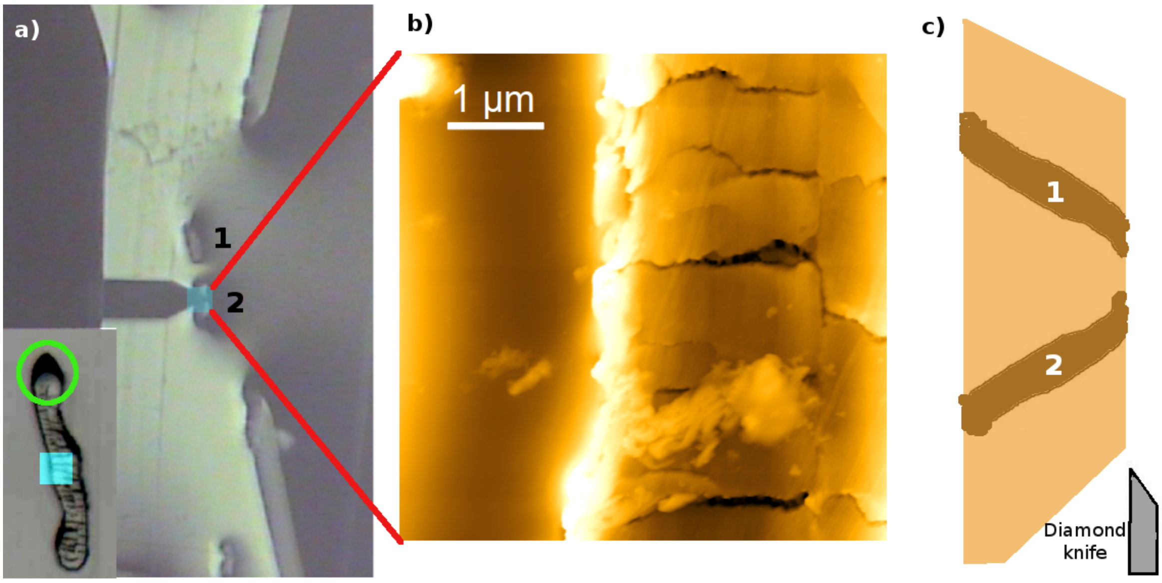

**Figure 4.19:** Cross-section of a single fiber. a) OM image from AFM (Inset: OM image taken in the microtome of the lower fiber highlighting the measured AFM area. The green circle highlights cell wall delamination). b) Corresponding AFM topography image, and c) sketch of fiber direction inside embedding material (side view from a)).

### 4.2.2 Fiber-fiber bonds

Besides studies on single fiber cross-sections, an extended effort was put on the investigation of embedded fiber-fiber bonds. Figure 4.20 represents a stitched AFM topography image of a fiber-fiber bond cross-section in a 90° configuration. The two fibers show an almost completely collapsed fiber. The upper fiber shows the cross-section of the pulp fiber. The typical fiber dimensions are $4-5$ µm for the width, 10 µm for the height, $3-4$ µm for the wall thickness and a thickness of 1 µm for the lumen. The lower fiber represents a longitudinal cross-section with a fiber height of 12 µm, a wall thickness of $5-6$ µm and 2.5 µm for the lumen. The transition zone between these two fibers where the bonding occurs is clearly revealed and marked in figure 4.20.

A very important fact is observable on the left side of the top fiber. Delamination of the S1 layer to the inner S2 layer is visible as it was already mentioned on beated fiber-fiber bonds (see section 4.1.6). Here, the outermost wall (S1) is in contact with the resin, in contrast to the visible gap between the S1 and S2 layer. This fact further supports that bonding between the S1 layer to external bonding partners is stronger than the internal bonding to the S2 layer.

However, it has to be checked if the embedding material is destroying the fiber-fiber bond by penetration or if this transition zone truly presents different features on the nanometer scale as it is proposed from Nanko and Ohsawa [8]. So far, no method was applied, which could solve this problem immediately. For future measurements, Tip-Enhanced Raman Spectroscopy (TERS) measurements are planned to further investigate this problem with high morphological and chemical resolution.

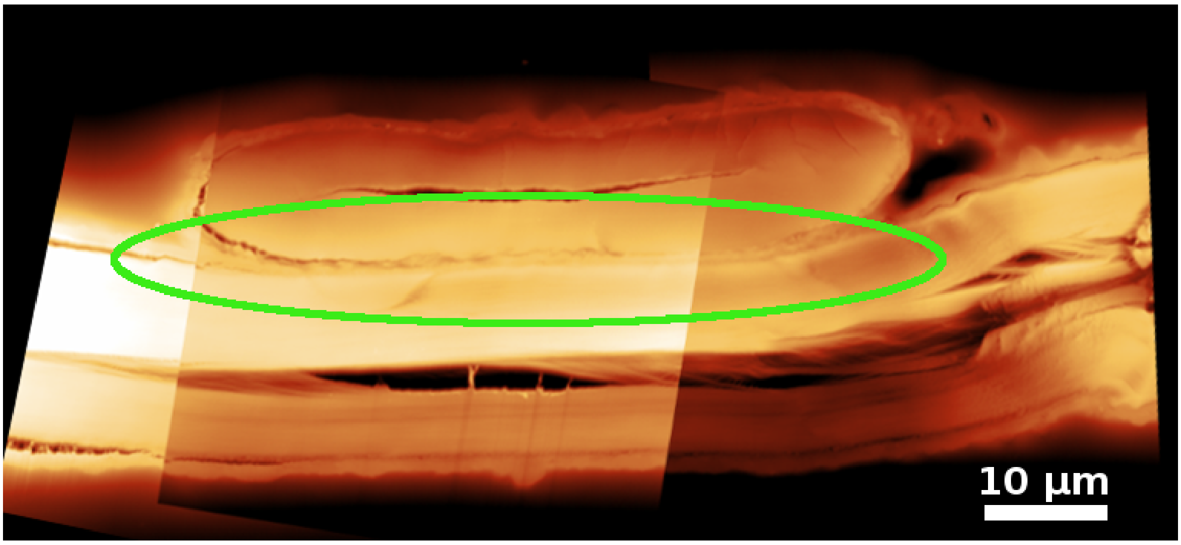

**Figure 4.20:** AFM image of the cross-section of a 90° bond of an industrial pulp. The axis of the top fiber is running out of the plane, whereas the axis of the lower fiber is running from the left to the right side. z-scale: 1 $\mu$m. Green line marks the bonding zone.

### 4.2.3 Paper sheets

As a side investigation the developed AFM procedure to study cross-sectional samples was also employed for additional measurements on embedded paper sheets. To improve image quality, measurements were performed in bimodal DualAC mode, revealing a higher contrast in the $2^{nd}$-Amplitude image. Figure 4.21 represents AFM images recorded from cross-sections of embedded sheets. A large scale AFM topography image (see figure 4.21a) is used to compare the measured position with the OM image (see figure 4.21b) taken priory at the microtomy station. A higher resolved AFM topography is presented in figure 4.21c and corresponds to the shaded area in figure 4.21a. The image in figure 4.21d presents the corresponding $2^{nd}$-Amplitude data, it reveals the highest contrast. The orientation on the different cell wall layers showed long parallel fibrils for the S2 layer, whereas the outer layer presents only short fragments, due to the different angle of the microtome cutting direction and the microfibril axis. The microfibrils on the S1 layer are cut almost perpendicular, whereas the microfibrils of the S2 layer are cut nearly in a longitudinal cross-section. Manual determination of the fibril width from the S2 layer yielded a value of (38 ± 7) nm.

Measurements on embedded sheets are necessary to study bonding conditions close to the productional environment. In contrast to defined fiber-fiber bonds, distinguishing if fibers are really bonded in a sheet or not is not always possible. Besides that, a wide variety of different fiber-fiber bonds with different angles is accessible. DualAC mode measurements revealed again highest contrast in the $2^{nd}$-Amplitude and are best suited for image analysis concerning the determination of microfibril diameters.

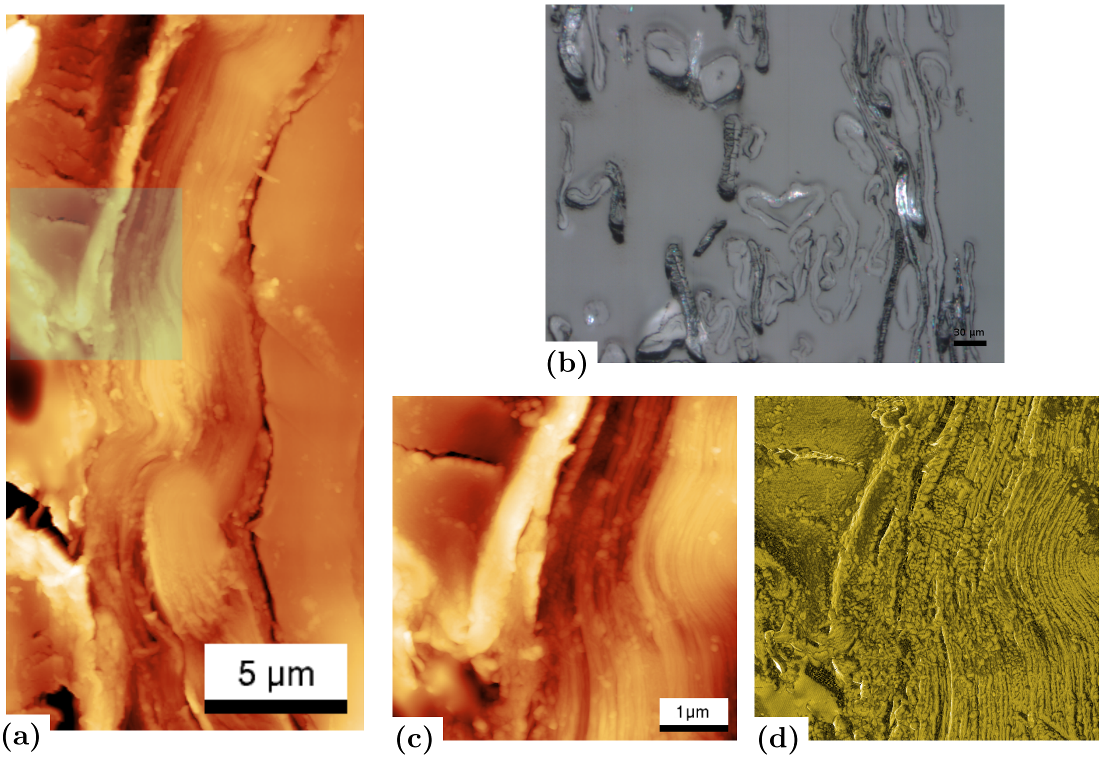

**Figure 4.21:** AFM images of an embedded sheet. a) large scale AFM topography image(z= 1000 nm), b) Optical image taken priorly in the microtome, c) higher resolved AFM topography image of the area emphasized in a), and d) corresponding $2^{nd}$-amplitude image (z= 50 nm).

### 4.2.4 Preliminary KPFM measurements

As a complementary method to achieve better materials contrast between embedding material and fiber cross-section, KPFM measurements were performed. This technique allows to measure simultaneously the topography and the Contact Potential Difference (CPD), which is a measure for the work function of the investigated material. Figure 4.22 represents KPFM measurements on fiber cross-sections. The bright contrast in figure 4.22a clearly separates the single fiber from the embedding material. Additionally, the lumen inside the fiber shows the same CPD signal as the embedding material which confirms the assumption that the embedding material is penetrating the fiber and fills the lumen. Further, different layers are visible close to the resin outside the fiber and to the lumen. Their thickness is in the range of that of P wall or S1 and S3 wall. Due to different orientation of the cellulose microfibrils a different work function is expected. The islands with a lower CPD inside the fiber are attributed to be particles from the embedding material.

Figure 4.22b shows a fiber-fiber bond of an embedded sheet. Unfortunately, due to the rough surface, the contrast in the CPD image is partly lost and therefore not continuous on the right fiber. The left one instead showed a homogeneous CPD signal. Furthermore, a small gap is clearly visible between the two fibers. That means either that there is no bond between these fibers or that the embedding material is penetrating the bonded area.

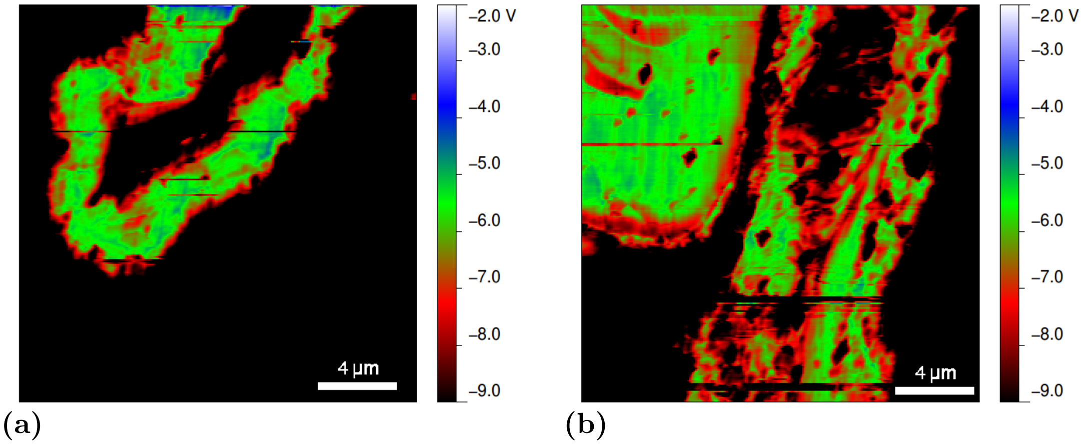

**Figure 4.22:** Contact potential difference maps of cross-sections of pulp fibers obtained by KPFM measurements. a) Single fiber, and b) fiber-fiber bond with the axis of the left fiber pointing out of plane and the right fiber's axis being in the plane.

It has to be summarized that the KPFM technique shows a strong contrast between the fiber and the embedding material. Further investigation based on this technique is desirable and might have the potential to provide additional insights into paper bonding. CPD mapping on the fiber surface might also be possible and could yield information of the charge distribution on the fiber surface as a useful input for calculations of bonding mechanisms based on Coulomb interaction.

## 4.3 Nanoindentation

Nanoindentation was performed with the Asylum Research MFP 3D AFM using a calibrated cantilever to determine the indentation hardness of the tested fiber samples. This is necessary as an input parameter to calculate the area in molecular contact based on sliding friction theory. The detailed instructions for the determination of the indentation hardness have been given in section 3.2.1.

Figure 4.23 represents a retraction curve of a force-versus-distance plot. Here, the cantilever is pressed towards a single industrial pulp fiber and afterwards retracted. Fitting of the two different slopes and solving the linear equation allows the determination of the indentation depth ($h_{max}$) and the corresponding force (F). For the experimental curve presented in figure 4.23, the resulting indentation depth is 215 nm and the corresponding force is F = 2.74 $\mu N$. These values are obtained before the first kink, due to the fact, that this kink is attributed to the response of the silicon support or the other cell wall layers. This data treatment is justified by the fact that for the area in molecular contact, only the first layer has access to the bonding region. Table 4.2 presents data for measurements on different fibers with the same treatment and resulted in an average indentation hardness of 0.19 GPa. The obtained results (R = 15 nm, H = 0.27 GPa) are in a good agreement with literature values using a nanoindenter for Lyocell (0.2 GPa) and Viscose (0.25 GPa) [31], wood tracheids (0.25 - 0.34 GPa) [29], and pulp fiber cell walls (0.2 - 0.45 GPa) [88]. Due to the fact that this was a side investigation, the measured data were only used to cross-check the data found in the literature and were not further supported by statistical analysis of a complete indentation series.

Nevertheless, the following can be stated from these indentation experiments. Investigation of the indentation hardness for pulp fibers revealed that a well calibrated cantilever is a suitable transducer to perform indentation tests on pulp fibers. Data obtained on kraft pulp fiber surfaces are in the range of data obtained by nanoindentation on various cellulose fibers.

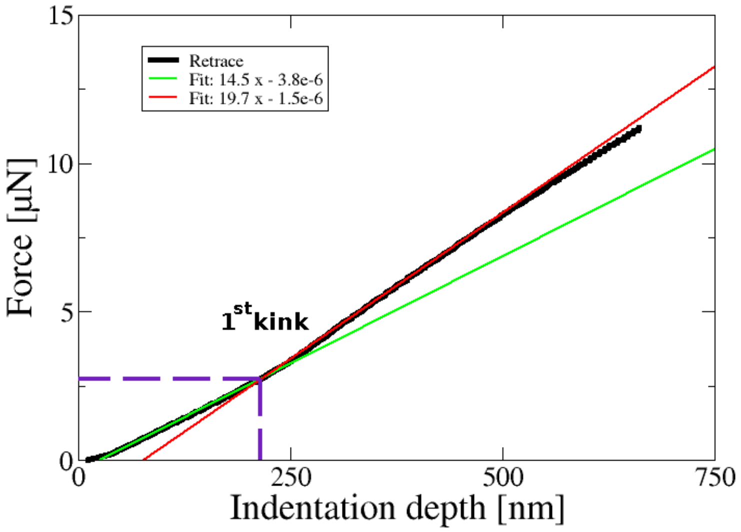

**Figure 4.23:** Retraction curve of a nanoindentation experiment in a single pulp fiber. Red and green lines are fits of the linear regime.

## 4.4 Force measurements to determine bond strength

This section is focused on the measurement of the force to separate two bonded fibers. Here, with the developed technique a mode close to mode I (tensile opening) is pre-

| sample | S [N/m] | h [nm] | F [$\mu$N] | H [GPa] |
|---|---|---|---|---|
| # 1 | 14.5 | 192 | 2.4 | 0.265 |
| # 2 | 8.5 | 300 | 1.5 | 0.108 |
| Average | - | - | 2 | 0.187 |

**Table 4.2:** Nanoindentation data of Monopol E (0 PFI) measured on Asylum Research MFP 3D AFM.

sented based on AFM technique. First of all, it should be mentioned that dealing with biological samples is a difficult task and therefore a large amount of measurements is not possible in a realistic time scale. The problems start already with mounting the fiber in the sample holder. Due to the small mass of fiber-fiber bonds, charging effects of tweezers produce enough Coulomb force that the fiber bonds stick to the tweezers. Air streams in the laboratory may blow fiber bonds away. After successful positioning of the fiber on the sample holder, fixation with the glue bears further risks. Nail polish may drop on the bond, or one of the fiber endings is too short for sufficient mounting. Beside these problems during the mounting process, further difficulties occur after curing of the nail polish. These failures are statistically evaluated in table 4.24. Here, various problems that could occur to a mounted fiber-fiber bond are summarized. These possible failures are wrong top fiber, detwisting of the strained fiber, issues of mounting problems, etc. Therefore, a lot of experimental skills had to be acquired to design an appropriate experimental setup for reproducible measurements.

### 4.4.1 Mechanical considerations

#### Area moment of inertia

The area moment of inertia is necessary to calculate bending and twisting of fibers and is approximated as an elliptical ring. For the two different directions y and z, the moment of inertia is calculated as:

$$I_y = \frac{\pi}{4}(AB^3 - ab^3) \tag{4.2}$$

$$I_z = \frac{\pi}{4}(A^3B - a^3b) \tag{4.3}$$

where A is the fiber width, B is the fiber thickness, a is the width of the lumen, and b is the thickness of the lumen. Since we know from cross-sectional AFM measurements the shape and dimension of the fiber's cross-section, we can estimate $I_y, I_z$ and $I_p$ from equation 4.2 and 4.3. For a collapsed fiber with a fiber width of 30 $\mu$m and a height of 10 $\mu$m with a fiber wall thickness of 4 $\mu$m the area moment of inertia are given in table 4.3.

For comparison with the estimations using the model of an elliptical ring as cross-section, a computer evaluation was performed to determine the area momentum of

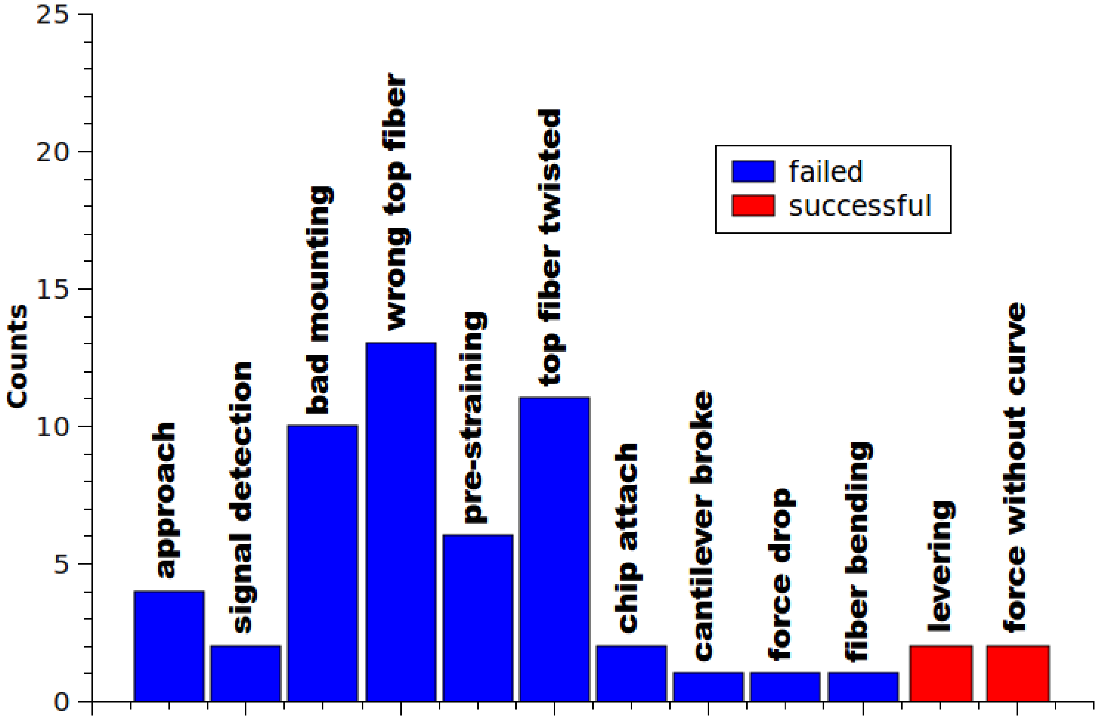

**Figure 4.24:** Statistics of possible failures which occurred during AFM based bond strength measurements.

| | elliptical ring | | fiber cross-section |
|---|---|---|---|
| | mathematical | figure 4.25b | figure 4.25a |
| $I_y$ $[\mu m^4]$ | 1460 | 6823 | 324 |
| $I_z$ $[\mu m^4]$ | 12200 | 21792 | 8015 |
| $I_p$ $[\mu m^4]$ | 13600 | 28616 | 8339 |

**Table 4.3:** Area moment of inertia of pulp fiber cross-section having typical values of common fiber parameters.

inertia from the masked fiber cross-section presented in figure 4.25a. Here, a and b are the image size in pixels, $\Delta z$ is the z-distance of the pixel to the center of gravity, $\Delta y$ is the y-distance of the pixel to the center of gravity, $\Delta r$ is the distance of the pixel to the center of gravity, and $A_{px}$ is the area of a pixel. This image analytical evaluation revealed that for a fully collapsed pulp the area moment of inertia is lower than the one from elliptical rings based on standard fiber parameters. Using equations (4.4-4.6), an elliptical ring with parameters of a fiber width of 28 $\mu$m, a height of 5.7 $\mu$m with a fiber wall thickness of 2.7 $\mu$m yields values of $I_y = 1460 \mu m^4$ and $I_p = 13600 \mu m^4$ which is close to the values determined for the fiber presented in figure 4.25a. Due to complete fiber collapse it is not always wise to approximate the fiber cross-section as elliptical ring which would overestimate the area moment of inertia. Evaluation of the area moment of inertia from AFM cross-sections revealed significantly lower values than approximations from elliptical rings.

$$I_y = \sum_{i=0}^{a}\sum_{j=0}^{b} \Delta z^2 A_{px} \tag{4.4}$$

$$I_z = \sum_{i=0}^{a}\sum_{j=0}^{b} \Delta y^2 A_{px} \tag{4.5}$$

$$I_p = \sum_{i=0}^{a}\sum_{j=0}^{b} \Delta r^2 A_{px} = I_y + I_p \tag{4.6}$$

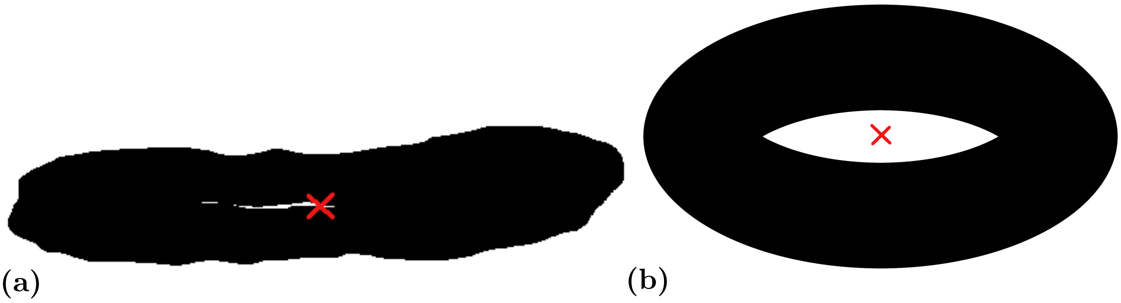

**Figure 4.25:** Mask of fiber cross-sections. The red cross marks the center of rotation. a) Evaluated from a recorded cross-sectional AFM scan, and b) elliptical ring.

### Simulation

Based on material's properties discussed in the previous section, simulations for different fiber loadings were carried out. Here, the simulation of the bending of the strained top fiber, the bending of the lower fiber, and the torsion of the top fiber due to the distance of the tip to the fiber-fiber bond are discussed using simple beam theory [89].

Figure 4.26 describes the dependency of the deflection from the applied force for an endloaded single fiber and a fiber which is fixed at two ends. In figure 4.26a, the lower fiber is described as an end-loaded beam following the given equation:

$$\delta = \frac{Fl^3}{3EI_y} \tag{4.7}$$

where F is the applied force, l is the length of the beam which corresponds to the distance of the AFM tip to the fiber-fiber bond, E is the Young's modulus which was assumed to be 20 GPa, and $I_y$ is the moment of inertia ($I_y = 324\ \mu m^4$). For comparison, the deflection of the strained top fiber is presented in figure 4.26b as a function of the gap between the sample holder benches. This bending characteristic is described as a beam fixed on both ends loaded at half length, following:

$$\delta = \frac{Fl^3}{192EI_y} \tag{4.8}$$

where l is now the distance of the two benches. Due to the low Young's modulus and the small moment of inertia, a too high deflection value is obtained. Nevertheless, the bending of the top fiber is significantly larger, than the buckling of the lower fiber and is attributed as the main contribution to the instantaneous strain.

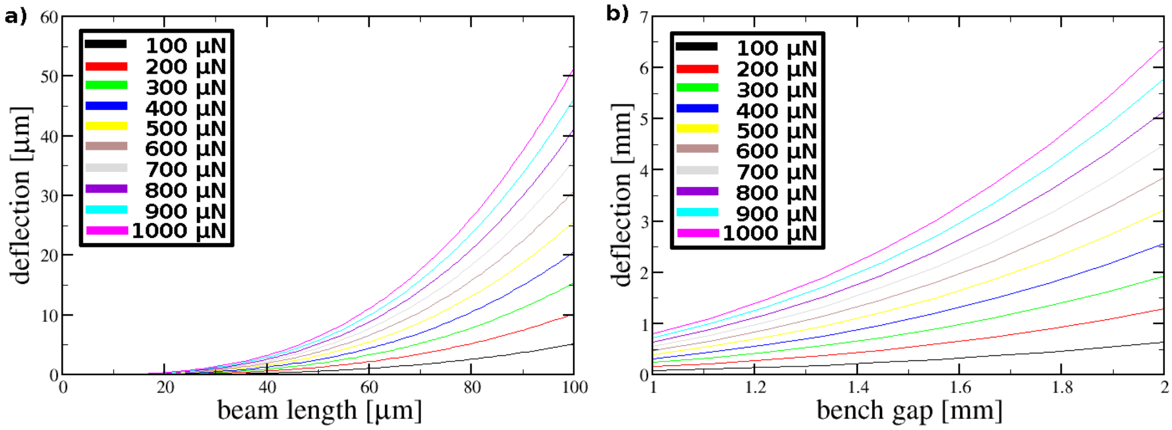

**Figure 4.26:** Deflection with varying force of a) an endloaded single fiber beam, b) a fiber which is fixed at two ends. The force was raised from 100 $\mu N$ to 1000 $\mu N$.

Beside bending of the top fiber, also its torsion due to the applied load is possible. The rotation angle $\theta$ is calculated from the given equation for a beam fixed on both ends:

$$\theta = \frac{FlL}{GI_p}. \tag{4.9}$$

Here, F is the load, l is the distance of the tip from the fiber-fiber bond, L is the distance of the two benches (1.5 mm), G is the shear modulus which is approximated as E/3, and $I_p$ is the area moment of inertia. A summary of the calculations with loadings raised from 100 $\mu N$ to 1000 $\mu N$ is presented in figure 4.27. The calculated values for the deflection of the cantilever due to the rotation of the top fiber of tens of $\mu m$ are in the same order of magnitude as the buckling of the lower fiber. Thus, it can be stated that bending of the top fiber is consuming most of the elastic deformation.

## 4.4.2 Experiments

### Unrefined pulp

As starting point in the CD-Laboratory, the investigation began on unrefined pulps as a model system. These collected data are presented in the following.

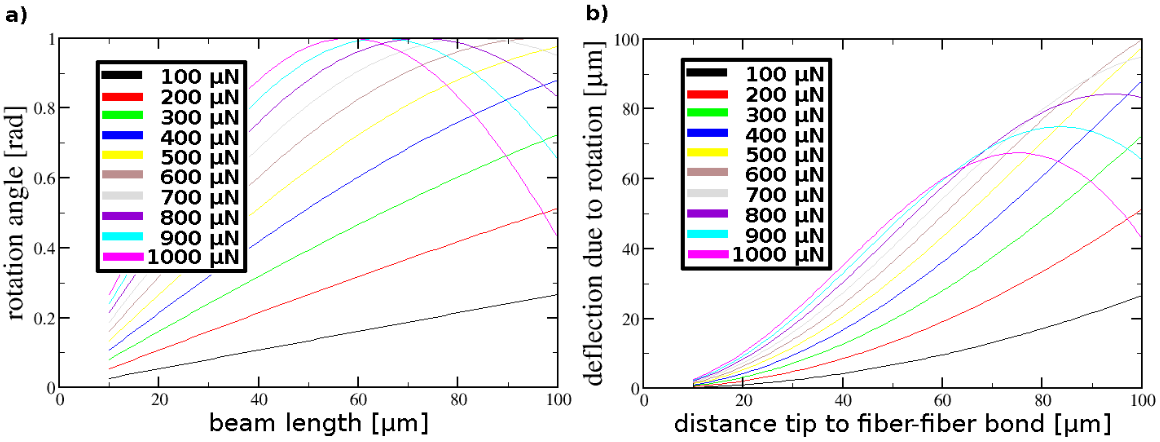

**Figure 4.27:** Moment on single fiber fixed on two ends. a) Rotation angle and b) effect on cantilever deflection as a function of load and distance of the tip to the fiber-fiber bond.

Figure 4.28 presents the OM image of the experimental setup inside the AFM chamber. The top fiber (TF) is the strained fiber and is the fiber from the bottom to the top of the image. The lower fiber (LF) is the floating one from left to right. It is only attached to the top fiber in a single joint, namely the fiber-fiber bond. On the left part of the image, the AFM cantilever (CL) attached to the chip is visible. Figure 4.28a describes the situation before the fiber-fiber bond failure, whereas figure 4.28b represents the situation after the separation. The formerly bonded area is visible as the dark area close to the cantilever in figure 4.28b. From these OM images, the distance from the tip to the fiber-fiber bond can be estimated. The typical distances are ranging from 40 to 60 $\mu m$.

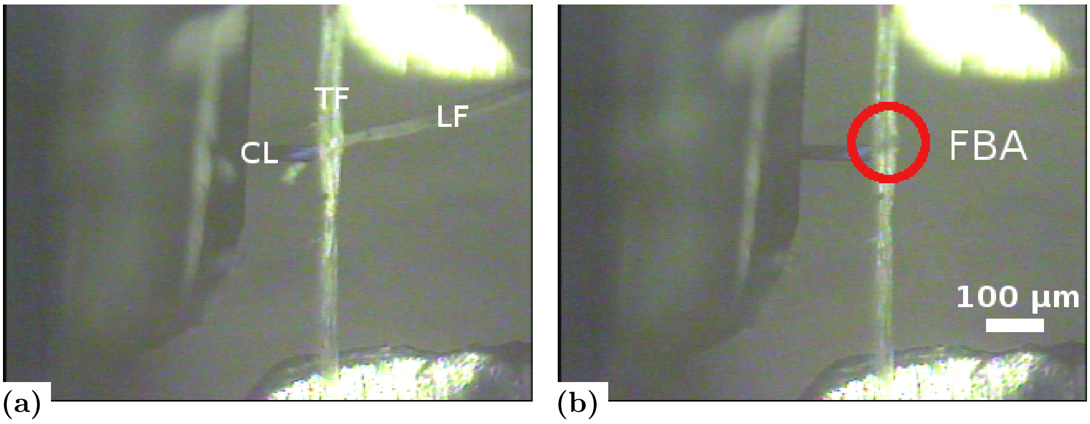

(a) (b)

**Figure 4.28:** Optical microscopy image of the measurement setup before (a) and after (b) fiber-fiber bond failure. The red circle marks the formerly bonded area. TF - Top fiber, LF - Lower Fiber, CL - Cantilever.

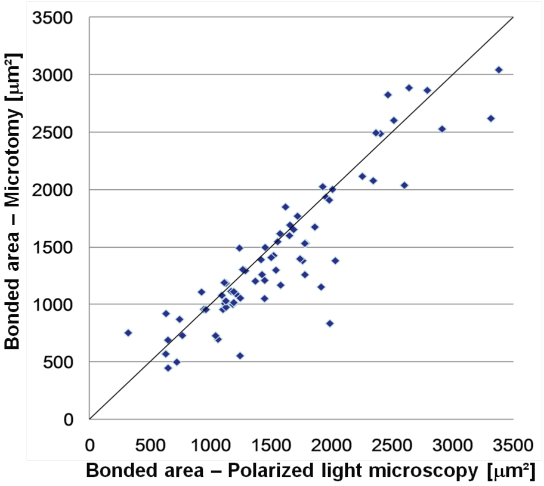

**Figure 4.29:** Distribution of the bonded area determined by microtomy and polarized light microscopy. (From [81, 84].)

According to significant morphological differences between the bonded and unbonded region (compare to section 4.1.5), an effect on the bonding strength is expected. Kappel et al. [81, 84] measured bonded areas with ultramicrotomy and PLM that range from 500 to 3000 $\mu m^2$ and resulted in a mean value of (1433 ± 622) $\mu m^2$ (see figure 4.29). OM measurements performed in our laboratory prior to the breaking experiment (figure 4.30) resulted in (1946 ± 700) $\mu m^2$. Figure 4.30 represents the intact bonded area prior to the bond strength measurement and the corresponding masked bonded area. The bonded area was determined by counting the black pixels of the masked area. The increased value is attributed to the limited optical resolution of the used OM, to the absence of polarized light in the OM with which partly unbonded areas could be detected, and to the lower statistics. In accordance to this large distribution of the bonded area, a wide distribution of fiber-fiber bond strength is expected.

Figure 4.31 represents two exemplarily recorded force-versus-distance curves. If the reflected laser from the cantilever backside is only hitting the top quadrant of the photodiode, the threshold is reached and further force increases are not detected. Also, the lower limit can be reached, if the the laser spot of the measurement was set on the lower quadrant of the photodiode at the beginning. These are measurement artifacts and are the consequences of the measurement limitations. They are clearly visible in figure 4.31a and figure 4.41. Due to this limitations, manual re-adjustment of the reflected laser to the lower quadrant of the split photodiode is necessary to increase the detection of higher forces. Further, after the fiber-fiber bond breaks, a force drop to a zero deflection is reached, which is not consequently zero force, due to re-adjustment of the measurement system. The point before this force drop is the bonding strength. Beside this single quantity, the behavior prior to the breaking is illustrated in figure 4.31b.

Here various force drops with a following force raise are observed. These force discontinuities are attributed to breaking of mechanical interlocks or fibril bridges. This is further supported due to the fact that in consecutive force-versus-distance curves such

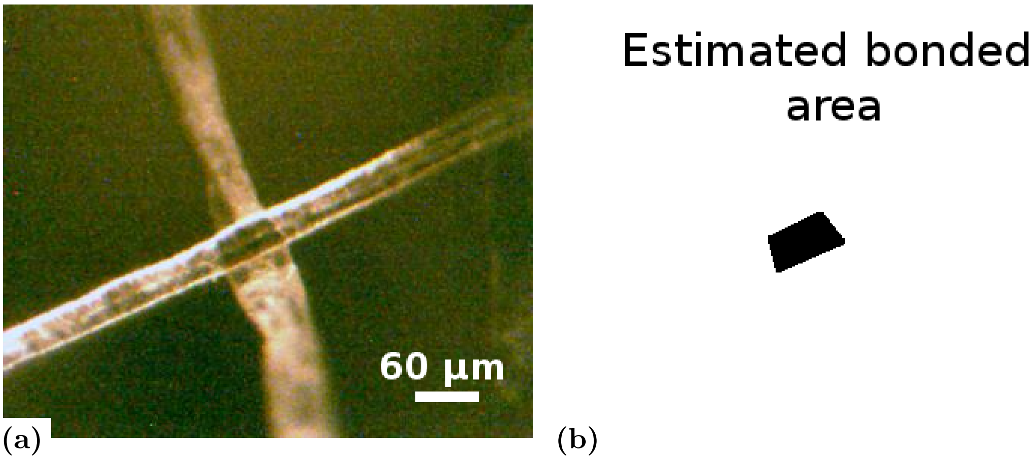

**Figure 4.30:** Determination of the bonded area prior to the breaking. a) OM image, and b) marked bonded area.

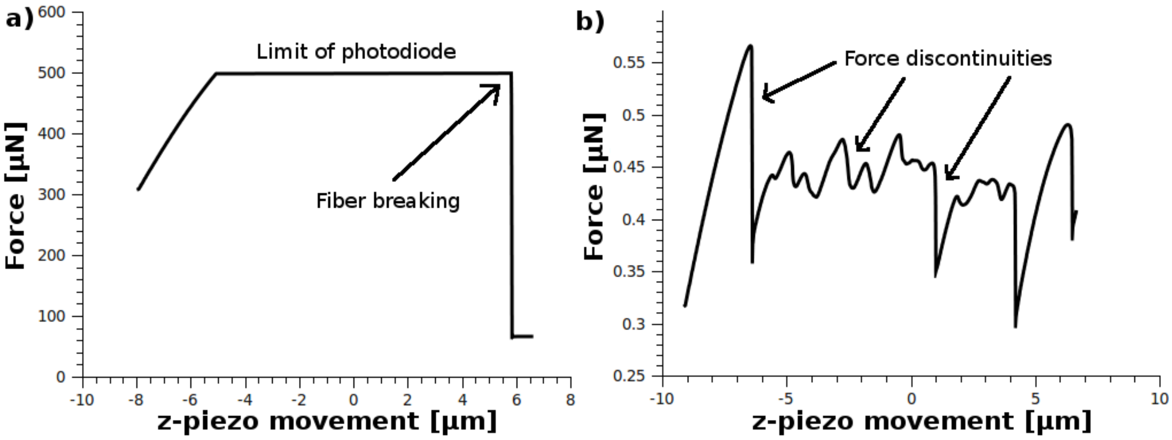

**Figure 4.31:** Exemplarily force versus distance curves to describe interesting features.

a vanishing of the force drop is no longer observed (see figure 4.32). This is another strong hint for breaking of mechanical interlocks as a reason for the observed force discontinuities.

Figure 4.33a summarizes the results of fracture tests of the unrefined pulp. Here, the data obtained from unrefined pulp range from 200 $\mu N$ to 600 $\mu N$. A statistical evaluation of twelve experiments revealed a mean bonding strength of 330 $\mu N$ with a standard deviation of 115 $\mu N$. This value for kraft pulp is significantly lower than the values obtained in previous investigations based on the measurement principle presented in figure 2.6 in section 2.2. In these investigations it was found that the typical value for kraft pulp fiber-fiber bonds is ranging from 1 to 6 mN (see table 2.4). The reason for this gap is the difference in the applied load. Due to the close approach of the cantilever to the fiber-fiber bond, the fracture behavior is close to a mode I (tensile opening mode), whereas the approach of the above mentioned techniques mimics to a

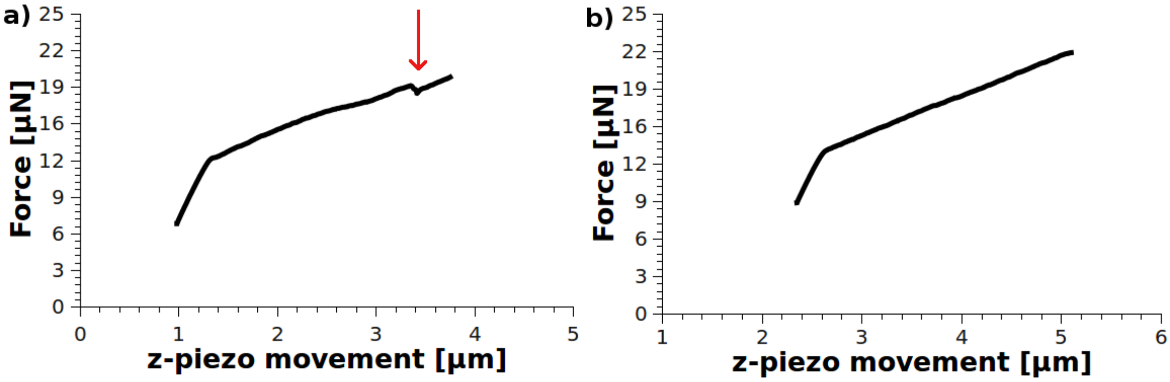

**Figure 4.32:** Vanishing of a force drop (indicated by the arrow in a) in the consecutive force-versus-distance curve (b)).

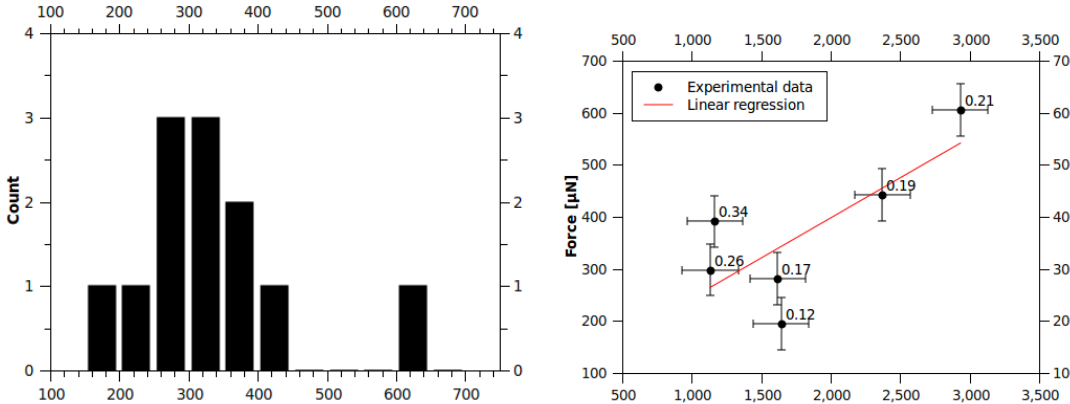

(a) (b)

**Figure 4.33:** Bond strength results of an unrefined pulp. a) Histogram and b) Force versus bonded area. The values next to the data points correspond to the specific bond strength [MPa].

mode II fracture (in-plane sliding mode) [15].

The corresponding bonded areas determined prior to the experiment with OM as one important factor for joint strength are taken into account in figure 4.33b. The figure represents a more or less linear increase of bonding strength with an increase in bonded area, i.e., the bond strength per FBA is constant. The values given for each data point are the calculated specific bond strengths [MPa]. Linear regression (red line) yields an average value of 0.15 MPa for the specific bond strength.

Besides the influence of the bonded area, other mechanism play a significant role in holding two fibers together. These influencing factors are the diversity of the fiber itself, morphological features - like pits - that change the fiber conformability [10], and the difference in residual strain resulting from the pre-straining of the top fiber in our experimental setup. Another important aspect is the difference between the bonded area and the area in molecular contact. The area in molecular contact is considered to be about 1000 times smaller ($< 1\ \mu m^2$) based on sliding friction theory [68] as it was discussed earlier (section 4.1.6). Nevertheless, the area in molecular contact is considered to be proportional to the bonded area. An experimental approach with stitched AFM images from both bonding partners could provide information of the area in molecular contact. Unfortunately, it was only possible to reconstruct the top fiber of the bonding partners so far.

Besides this single quantity - the bond strength - the introduced method provides additional information on the breaking behavior prior to the failure. Figure 4.34 represents a stitched master curve which has been calculated from four consecutive force-versus-distance curves. After the limit of the z-piezo movement is reached, the retraction curve starts. The force of this reversal point is defined as the threshold force. The part of the consecutive force-versus-distance curve after the threshold force is than stitched to the former curve (see figure 4.35).

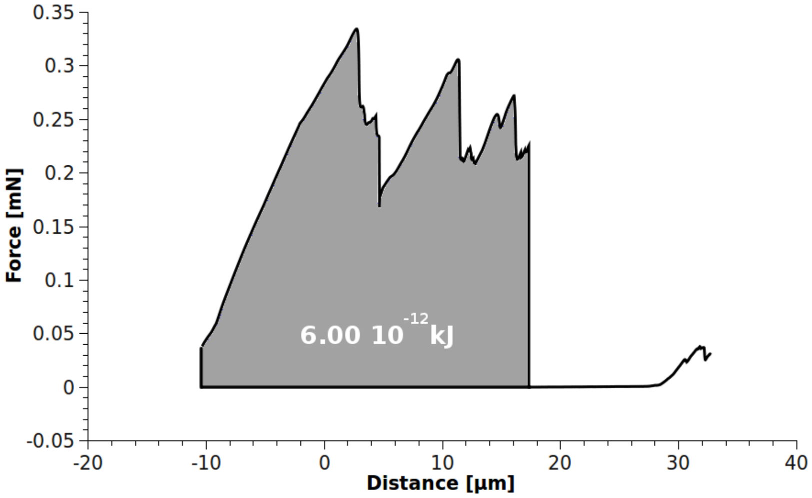

**Figure 4.34:** Master curve to determine the bonding energy.

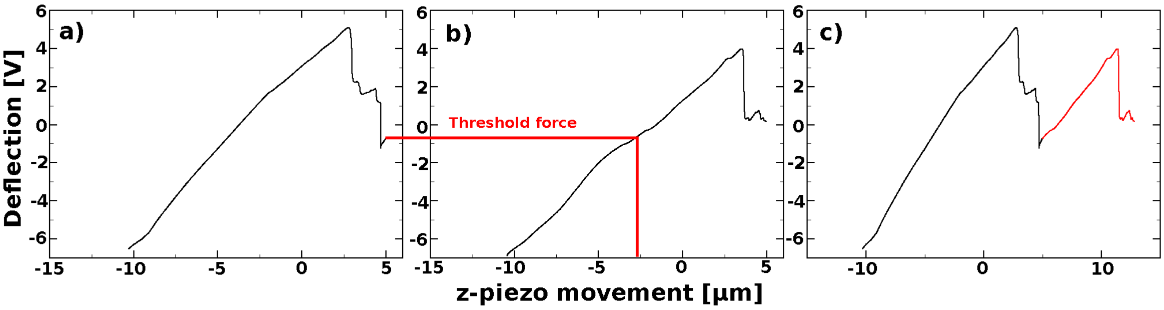

**Figure 4.35:** Generation of a master curve. a) First curve, b) second curve, and c) curve b) added to a).

The stitched master curve describes an increase of the loading force with force discontinuities and a final failure after a distance of 26 µm of z-piezo movement. The force discontinuities are attributed to breaking of mechanical interlocks or fibril bridges and are in the range of 100 $\mu$N. The area underneath the force versus distance curve corresponds to the consumed energy

$$W = \int F(s) \cdot ds. \tag{4.10}$$

For the presented experiment, a total energy of $6.00 \cdot 10^{-12}$ kJ was necessary to break this particular bond.

In order to determine from such a value the energy of the bond, we have to consider all the energy contributions to the bond energy. These contributions are elastic ($W_{el}$) and visco-elastic ($W_{visco}$) energy losses of the fiber-fiber bond, tip indentation into the fiber ($W_{tip}$), and torsion or buckling of the cantilever ($W_{cant}$). So far the last two could not be evaluated in the experiment.

$$W_{tot} = W_{el} + W_{visco} + W_{bond} + W_{tip} + W_{cant} \tag{4.11}$$

Therefore, the next paragraphs will deal with the evaluation of $W_{el}$ and $W_{visco}$ energy parts. So far, elastic and visco-elastic energy contributions have been calculated. The determination of the elastic energy of the measured fiber-fiber bond was performed in a distance controlled experiment as described in chapter 3.2.1.

Figure 4.36 summarizes the results of such a distance controlled experiment. A force versus time (F-t) plot of the experiment is represented in figure 4.36a indicating the exact positioning of the cantilever close to the fiber-fiber bond at the first seconds (320 - 350 s). After these prerequisiting steps, a single displacement cycle was manually carried out at 360s to check the measurement setup. Then 8 displacement cycles have been performed automatically every two seconds till the fiber-fiber bond failure happened. The experiment demonstrates a degradation of the peak force with each displacement cycle from almost 0.8 mN to 0.7 mN and a failure of the bond at 600 $\mu$N for this particular experiment. Figure 4.36d summarizes the corresponding force-versus-distance plot of all the cycles presented in figure 4.36a. The kink in the first cycle (figure 4.36b) is attributed to indentation of the tip into the lower fiber and is only visible in the loading curve due to a permanent contact of tip and sample.

The hysteresis in the individual cycles is a measure for the dissipated energy. The calculated value for each cycle is presented in figure 4.37. In the first cycle, more energy is dissipated due to visco-elastic contributions, tip indentation or slight movement of the top fiber. The complete dissipated energy is approximately 10% of the total energy input calculated from the added dissipated energy of each cycle. The large elastic part of 90% is attributed to deflection and twisting of the top fiber.

$$W_{el} \approx 0.9 \cdot W_{tot} \tag{4.12}$$

A closer insight into the dissipated energy is provided by a modification of the experiment to a load controlled one. Here, the load is kept constant for a certain time and the movement of the cantilever by the z-piezo - necessary to maintain constant cantilever bending - is recorded. Then the force is stepwise increased. Figure 4.38 presents

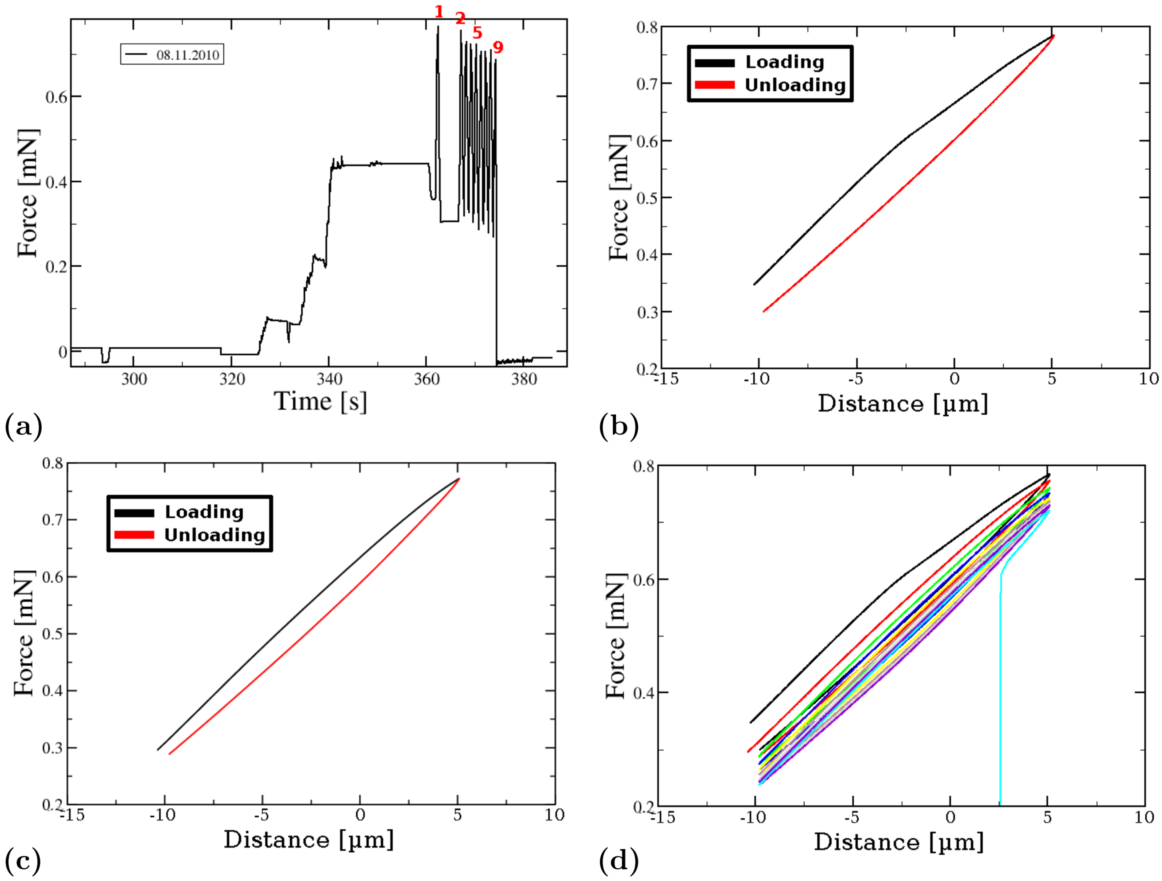

**Figure 4.36:** Dynamically loading of a fiber-fiber bond in a distance controlled experiment. a) Loading cycle, b) corresponding force versus distance of 1st cycle, c) corresponding force versus distance of 2st cycle and d) all corresponding force versus distance curves.

the results of such a force controlled experiment. The applied load onto the fiber-fiber bond as a function of time is shown in Figure 4.38a, whereas the corresponding z-piezo movement is plotted in Figure 4.38b. Due to restrictions of the z-piezo movement manual re-adjustment is a necessity and causing displacement drops at 300 s and 650 s. The first displacement drop at 80 s is attributed to the fine approach of the AFM cantilever to the fiber-fiber bond. The increase in z-piezo movement is ascribed to the instantaneous elastic strain like deflection and twisting of the top fiber. Immediately after this instantaneous strain, an increase in the distance is observed which is attributed to creep inherent to a visco-elastic material as it is described in the literature [90]. Analyzing the steady-state creep rate reveals an increase with raising load as it is found for alumina for instance [91]. To calculate the total amount of visco-elastic energy, the simultaneously recorded data of force and z-piezo movement are plotted in a force-versus-distance plot (figure 4.39a). From this plot, energy contributions due to a movement based on a constant load can be calculated. Figure 4.39b represents the

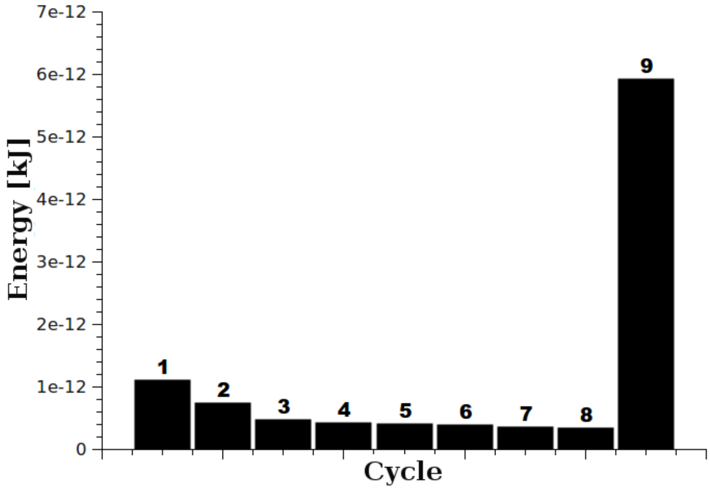

**Figure 4.37:** Dissipated energy calculated from each hysteresis of the cycles presented in figure 4.36a.

data obtained for the individual load states marked in figure 4.38a. The calculated total amount of visco-elastic energy from the force versus distance curve is 1% of the total energy input.

$$W_{visco} \approx 0.01 \cdot W_{tot} \tag{4.13}$$

The final increase in the z-piezo movement corresponds to the fiber-fiber bond failure and a final z-piezo movement to a full extension due to the loss of the feedback signal. Figures 4.38c and 4.38d show the signals of one single loading cycle with higher resolution, revealing an exponential increase after load and an exponential decay after unloading, like it is predicted for visco-elastic materials [90, 91].

Once we have determined the elastic and visco-elastic energy contributions to the total energy the bond energy can be calculated using:

$$W_{bond} = W_{tot} - W_{el} - W_{visco} = 0.09 W_{tot} \tag{4.14}$$

For the unrefined, unbleached pulp the energy input into the fiber-fiber bond is $10^{-13} - 10^{-12}$ kJ/bond. First theoretical calculations [92] predicting bond energies of van der Waals ($10^{-16}$ kJ/bond), hydrogen bonding ($10^{-17}$ kJ/bond), and Coulomb ($10^{-10}$ kJ/bond) interactions. Van der Waals and hydrogen bonding forces are considered to be lower boundaries based on estimations of cellulose I crystals. The calculated Coulomb interaction is an upper boundary and is based on charge measurements of the desired pulp. These estimations are in good agreement with our experimental value ($10^{-13} - 10^{-12}$ kJ/bond) and theoretical literature data (theoretical hydrogen bonding: $10^{-13}$ kJ) [93].

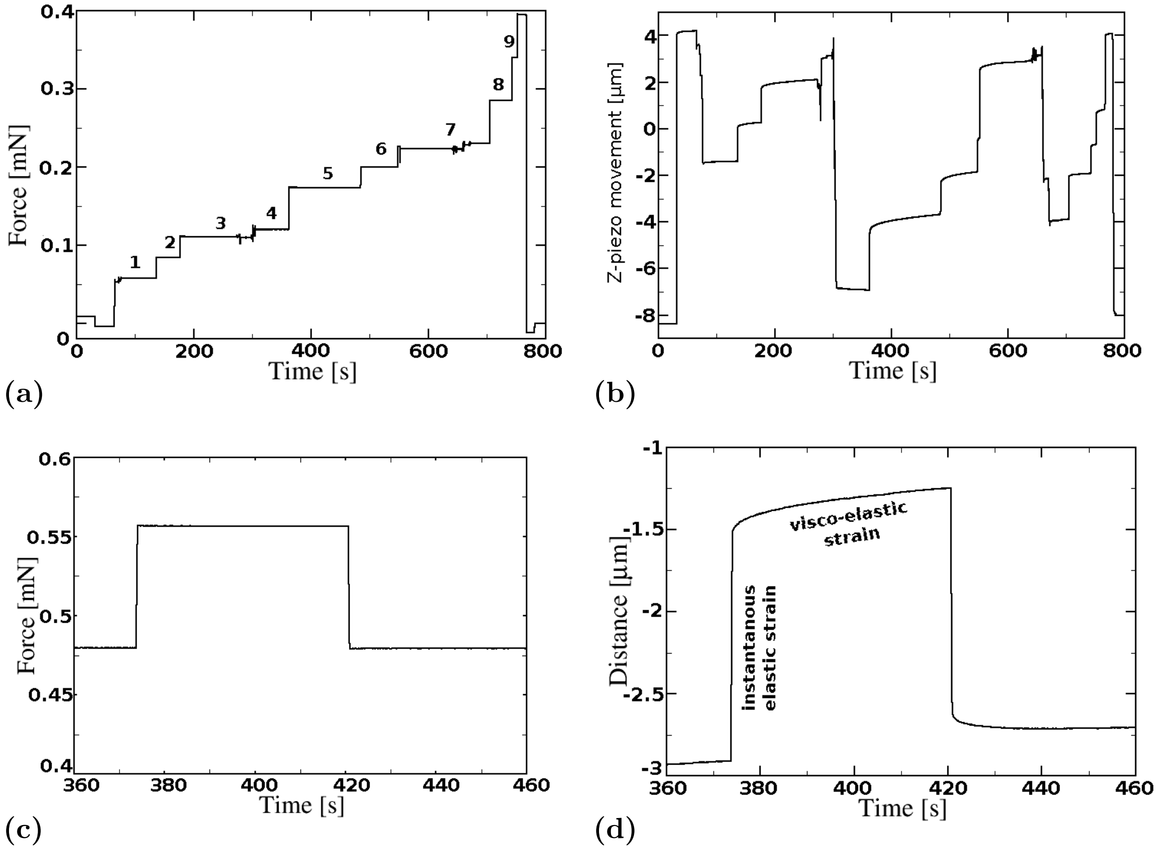

**Figure 4.38:** Visco-elastic behavior of a single fiber-fiber bond in a load controlled experiment. a) Load, b) corresponding z-piezo feedback of a), c) load detail, d) corresponding piezo movement of c).

### Refined pulp

This section deals with the investigation of refined pulp. Due to the fact, that the main focus of the CDL was set on unrefined industrial pulp, this is just a first glance on refined pulp.

**2000 Revolutions** Figure 4.40 summarizes the findings based on moderately beaten pulp. The features visible in stitched AFM topography image (figure 4.40a) are already discussed in section 4.1.6. The force-versus-distance curve presented in figure 4.40b reveals various force discontinuities. A histogram of these force discontinuities is presented in figure 4.40c. Here, a bimodal distribution of the force drops is recognizable. The lower fraction results in a force drop of approximately 20 $\mu$N, whereas the larger force drops are ranging from 60 to 100 $\mu$N. Comparison of the force data with the obtained AFM topography image reconstruction revealed that the higher forces may be correlated to complete wall delaminations (see figure 4.17 and discussion in section 4.1.5). This would fit to the 3 cell wall layer delaminations visible in figure 4.40a and

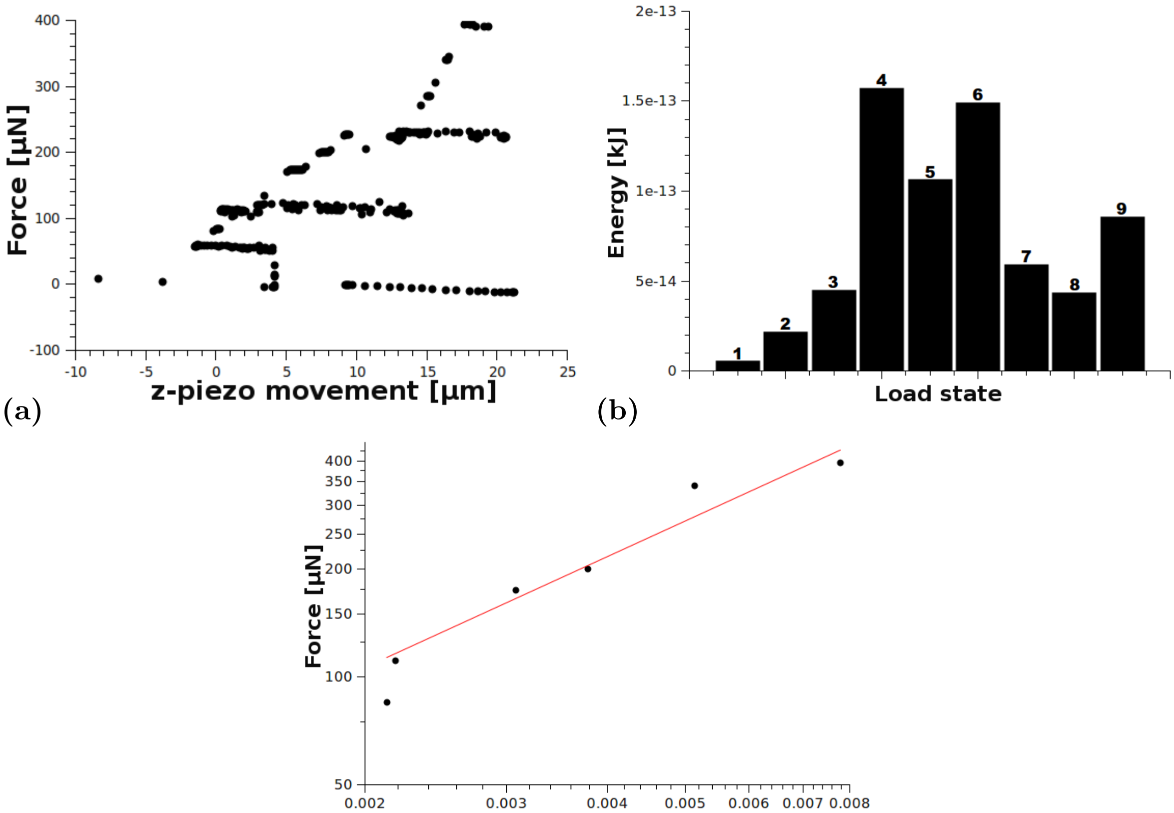

(a) (b)

(c)

**Figure 4.39:** Force-versus-distance plot calculated of figure 4.38a and b, b) determined visco-elastic energy, and c) creep rate as function of load.

the 3-4 large force drops presented in figure 4.40b. Further, the bridging fibrils between the individual layers are everywhere intact and not yet broken. The smaller force drops are attributed to sliding friction forces of microfibrils or fibril bundles or to a rupture of single cellulose fibrils. Analyzing the total energy input resulted in 6.00 $\cdot 10^{-12}$ kJ for this particular bond. This particular energy input is, however, smaller than the one obtained from the unrefined pulp, but it is explainable by the small bonded area of 614 $\mu m^2$.

**9000 Revolutions** Figure 4.41 presents a master curve of a highly refined pulp (9000 PFI). Due to the high degree of beating, the fiber is strongly fibrillated. This circumstance should increase the amount of fibril bridges and mechanical interlocks. In comparison to the master curve presented in figure 4.40b for a moderately beaten pulp, here, an increased amount of force discontinuities is indeed detectable. This observation further supports the concept of mechanical interlocks or fibril bridges observed in the stitched AFM images presented in section 4.1.6. Analysis of the consumed energy input resulted in 2.81 $\cdot 10^{-11}$ kJ for this particular bond which is considered to be a weak bond due to the small bonding area of 350 $\mu m^2$. This value is only slightly higher

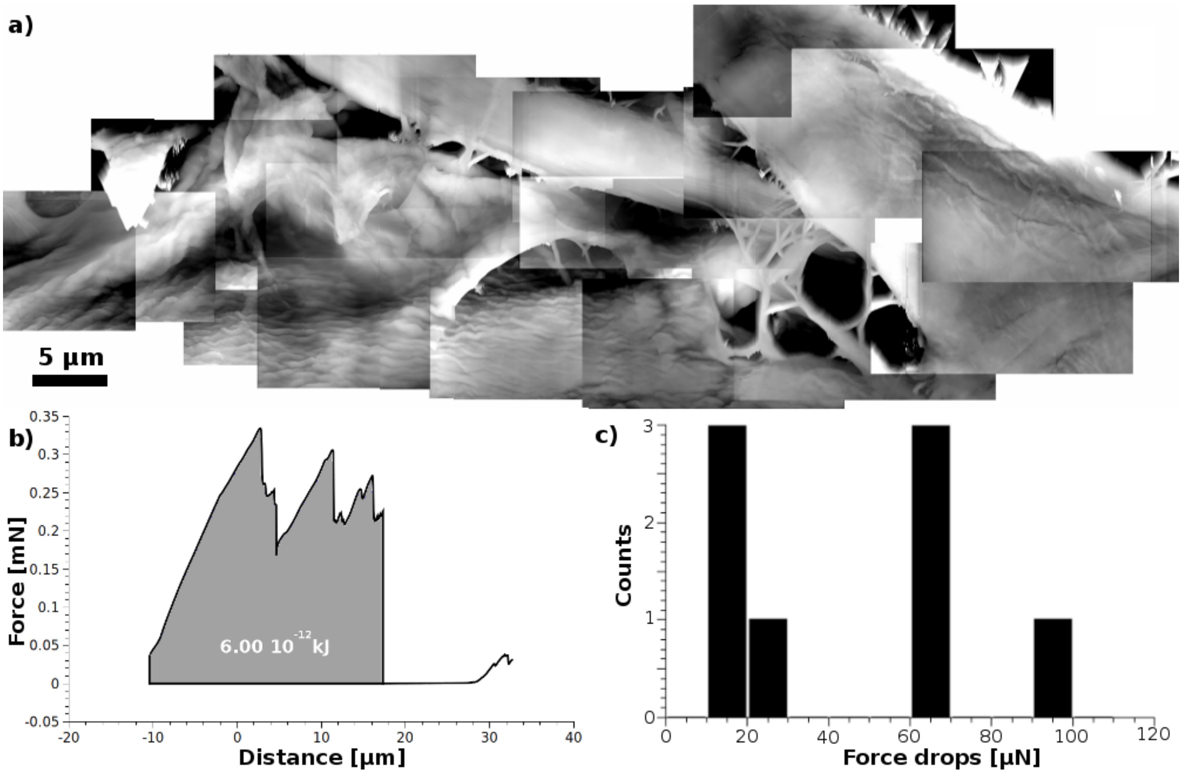

**Figure 4.40:** Summary of the investigation of a moderately beaten pulp (2000 PFI). a) Stitched AFM topography image, b) force-versus-distance master curve, and c) histogram of the force discontinuities.

than values found for the unbeaten pulp, but it is just one value for a weak bond. Due to the rough surface of this highly refined pulp, it was not possible to obtain AFM topography images of the FBA. Therefore, it is not possible to compare the behavior of the force-versus-distance curve with stitched AFM topography images.

Figure 4.42 presents the analysis of the force discontinuities on the highly beaten pulp shortly prior to the bond failure. The force-versus-distance curve (figure 4.42a) shows two different types of force discontinuities. A more detailed look on these discontinuities is presented in figure 4.42b. Here, a bimodal distribution as already mentioned on the moderately refined pulp is recognizable. The small force drops are approximately 25 $\mu$N whereas the large force discontinuities range from 100 $\mu$N to 200 $\mu$N. The larger force drops are twice the value of those found in the moderately beaten pulp. This means that more microfibrils in the fibril bundles are involved. Beside fiber wall delamination also breaking of fibril bundles is possible and maybe attributed to the larger force drops.

The summary of the data obtained on refined pulp are presented in table 4.4 together with data for the unbeaten pulp. Here, the bonding strength of the highly refined pulp is two times larger than the average value of the unrefined pulp. The bonding strength of the moderately beaten pulp is equal to the unbeaten pulp but is explainable due to a small bonding area. Due to the lack of statistics, a detailed description of the bonding dependency from beating is not possible at the moment.

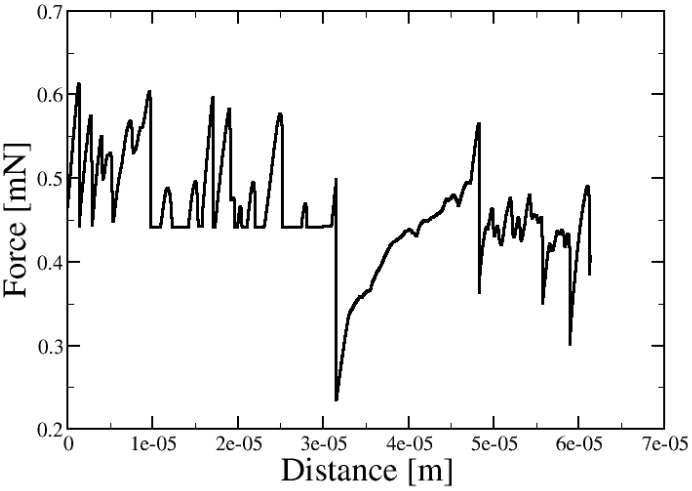

**Figure 4.41:** Stitched master curve of a highly refined pulp (9000 PFI).

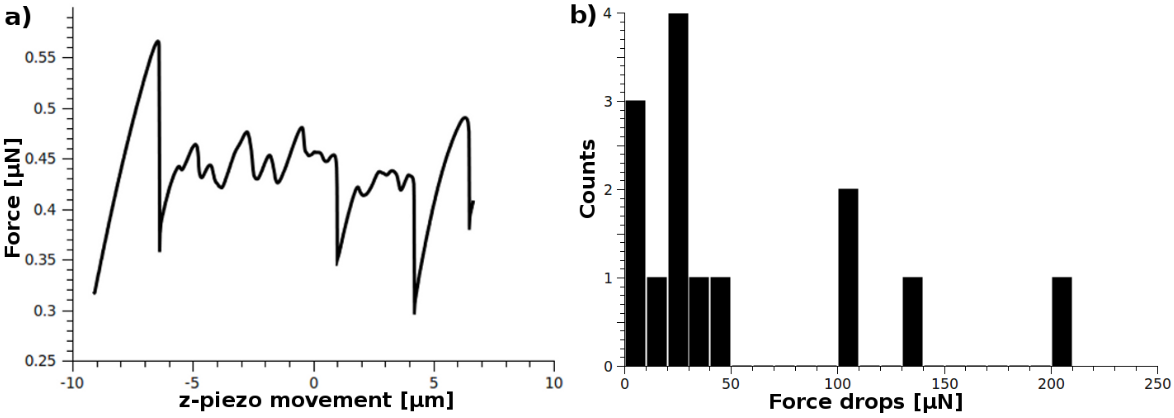

**Figure 4.42:** a) Force-versus-distance curve of a highly beaten pulp (9000 PFI) and b) analysis of the force discontinuities.

| Revolutions | Measurements | Mean value [$\mu$N] | Deviation [$\mu$N] | Energy input [kJ] |
|---|---|---|---|---|
| 0 | 12 | 330 | 115 | $9.50 \pm 0.60 \cdot 10^{-12}$ |
| 2000 | 1 | 320 | - | $6.00 \cdot 10^{-12}$ |
| 9000 | 1 | 620 | - | $2.81 \cdot 10^{-11}$ |

**Table 4.4:** Influence of beating on the fiber bond strength and bond energy.

Table 4.5 summarizes the different regimes of the force drops with their proposed breaking element. The lowest force of about 15-25 $\mu$N is attributed to breaking of individual single microfibrils. The force range from 50 $\mu$N to 100 $\mu$N is described as the cell wall delamination and forces higher than 100 $\mu$N are ascribed as the rupturing of fibril bundles.

| Breaking element | force [$\mu$N] |
|---|---|
| Single fibrils | 15-25 |
| Cell wall delamination | 50-100 |
| Fibril bundles | 100-200 |

**Table 4.5:** Proposed mechanisms for force drops.

### 4.4.3 Conclusions

To conclude the findings in this section, it has to be stated that the presented method to determine the bonding strength based on AFM technique bears great potential in the investigation of fiber-fiber bonds. A combination of determination of the bonding force and the behavior prior to the failure and the investigation of the formerly bonded area reveal new insights into the bonding mechanisms and promotes the concept of mechanical interlocking or fibril bridging. Further, the evaluation of the bonding strength and the determination of the bonded area allow the calculation of a specific bond strength. It has also been demonstrated that the method is capable to investigate higher refined pulps.

In contrast to other methods, mainly based on a setup similar to figure 2.6, the obtained values are lower due to a different applied load mode. The big problem of this method is the necessity of a correct setup, where the strained fiber has to be the top fiber. For a shear loading approach it does not influence the measurement which fiber is the top fiber. Unfortunately, the identification of the top fiber is not possible without an underlying support due to the semi-transparent optical properties of the pulp fibers. Thus, the top fiber issue is only distinguishable after the experiment and a breaking of the fiber-fiber bond.

Figure 4.43 summarizes all information gathered from the developed method to determine the bonding strength based on AFM technique on one single fiber-fiber bond. Figure 4.43a presents the stitched AFM topography image revealing dangling microfibrils inside and close to the transition zone between the bonded and unbonded region. The green guidelines mark the transition zone between the smoother, formerly bonded area and the wrinkled, unbonded region. At the top of the image, a pit is highlighted by a red circle. The FBA determined by pixel counting resulted in 935 $\mu m^2$. The corresponding OM image recorded shortly after the successful separation is presented in figure 4.43b. The red circle marks the formerly bonded area which was determined to be 1167 $\mu m^2$. Figure 4.43c represents the applied force as a function of the measurement time. The inset illustrates the time shortly prior to the bond failure of almost 400 $\mu$N. Together with the FBA, this results in a specific bond strength of 0.43 MPa for this particular bond. The corresponding z-piezo movement is presented in figure 4.43d and visualizes the visco-elastic behavior of the fiber-fiber bond during loading.

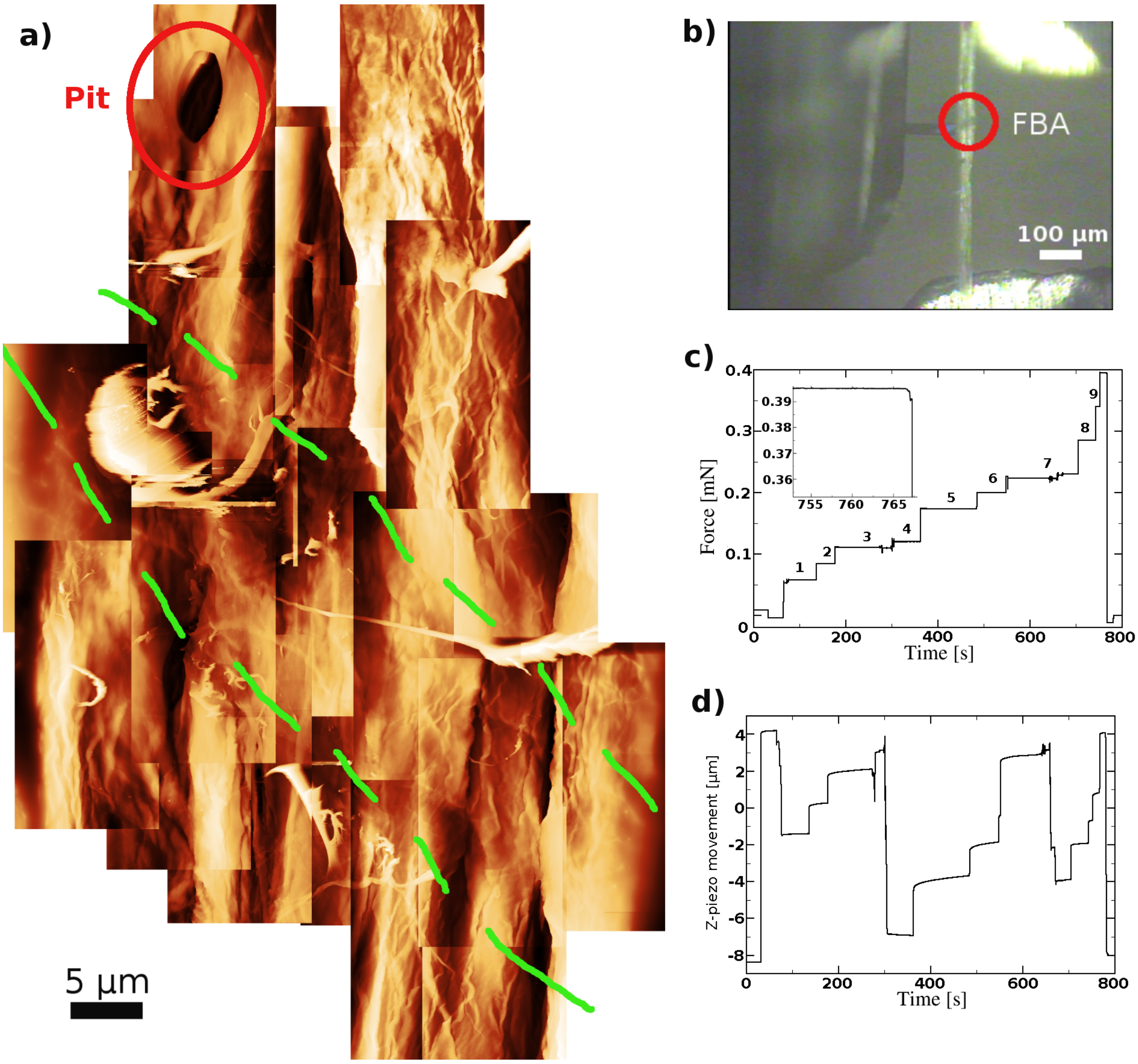

**Figure 4.43:** Summary of fiber-fiber bond investigation. a) Stitched AFM topography (z-scale: 1 $\mu$m), b) OM image of a), c) loading curve (inset: detail of bond failure), and d) corresponding z-piezo movement.

# 5 Conclusions and Outlook

In this thesis, a deeper insight into the mechanisms of fiber-fiber bonding, based on atomic force microscopy (AFM) measurements is presented. First, morphological features on the fiber surface are investigated and discussed. Special focus was put on the separation of elongated mircofibrils and precipitated lignin spherules. A comprehensive study of the diameter of lignin precipitations as a function of the $\kappa$-number is presented. The investigation revealed an increase of the surface coverage of lignin precipitates. Furthermore, the individual lignin precipitates are more uniform in size with an increased treatment of black liquor cook or oxidation. Additional surface features such as pits and hornification and their influence on the bond strength are debated.

Second, morphological differences on bonded and unbonded areas have been studied in detail. Analyzing Wenzel ratios for each area revealed that the bonded area has a smoother surface, where the true surface area is approximately 7 % larger than the projected one. In contrast, the unbonded true surface area is 20 % larger, mainly enhanced by wrinkles appearing during the process of drying. Besides morphological roughness differences, additional surface features are visible on the bonded region. Here, dangling microfibrils - acting as mechanical interlocks or fibril bridges - are observable, which appear especially close to the transition region between bonded and unbonded area. In contrast to unrefined pulp, the formerly bonded area of refined pulp exhibits a different surface appearance, featuring delaminated cell walls and a larger amount of bridging elements.

To obtain a completer insight into the fiber-fiber bond, cross-sectional investigations were performed on embedded samples. Here, it was revealed, that the morphological information alone is not sufficient to identify the gap between the two bonded fibers. The key issue is whether the fibers are actually bonded or the embedding material is penetrating into the bonded area. As a first glance, KPFM images of fiber cross-sections are presented which reveal a strong contrast between the fiber and the embedding material. Besides that, the handling of the embedded samples with the cutting tool in the microtome introduces strain to the fiber cross-section which results in cracks and delamination of inner cell walls.

The main part of the thesis was devoted to the development of a new method to measure the bonding force between two bonded fibers. Here, a calibrated AFM cantilever was utilized to apply a force onto the fiber-fiber bond. With two different control parameters - load and displacement - the method is suitable to determine elastic (90 %) and visco-elastic (1 %) energy contributions of the total energy input ($10^{-11} - 10^{-12} kJ$). Besides the calculation of the energy consumed by the bond ($10^{-12} - 10^{-13} kJ$), the necessary force as well as the mechanisms prior to the failure are described. The performed experiments reveal for unbeaten, unbleached industrial pulp fibers a mean value of the bonding strength of 330 µN. Together with the determined size of the formerly bonded area, a specific bond strength was evaluated to be 0.15 MPa. Further, force discontinuities observed in force-versus-distance curves promote bridging elements and mechanical interlocks. Analysis of the force discontinuities revealed different force regimes for rupturing of single cellulose fibrils (25 $\mu$N), fiber wall delamination (50-100 $\mu$N), and breaking of microfibril bundles ($> 100$ $\mu$N). In combination with the AFM investigation of the formerly bonded area, these mechanisms are considered to play an important role in bonding two fibers together which is essential to form paper.

### Future applications

The introduced method to determine bond strength of paper fibers was successfully applied to fiber-fiber bonds of unbeaten, unbleached fiber-fiber bonds. It should be further applied to these systems in order to increase the statistics. Especially, the combination of bond strength evaluation together with the determined bonded area by AFM will be extended to evaluate the specific bond strength. Besides that, the method can be applied to measure beaten pulp as well as chemically modified pulps. Due to expected higher bond strength, stiffer cantilevers are demanded and might be commercially available in the future.

Furthermore, regenerated cellulose fibers are important design fibers to systematically study the influence of fiber treatments on the bonding properties. Due to different design parameters of the spinning nozzle, various fiber cross-sections are producible. Special focus should be paid on Bellini fibers, which have a similar cross-section as pulp fibers but are flat hollow tubes. In contrast to pulp fibers, the Bellini fibers have a defined, reproducible surface morphology and chemical composition.

Additional measurements on model cellulose films and the influence of hemicellulose and other forms of treatment are ideal test samples to gain knowledge on defined structures on a larger scale. This should further support studies based on the regenerated fibers. Here, AFM based image analysis allows a comprehensive surface characterization. Together with the force measurements influences on the bond strength can be correlated to surface morphological changes.

A combined investigation of both, cellulose model films and regenerated cellulose fibers, bears the opportunity to study defined structures on two length scales. Therefore, scaling laws from areas of square micrometers to square millimeters can be obtained.

Another important aspect for future measurements is the determination and correlation of the bond strength with defined pre-straining of the top fiber. This would also reduce one possible failure prior to the experiment and would define an additional parameter affecting the bonding strength. Additionally, further effort should be put onto the determination of the top fiber with a non-destructive method to decrease the amount of wrong mounting.

A further promising parameter of investigation is the variation of the humidity during the investigation. Here, morphological changes - as a result of drying - will be characterized in-situ. This will allow to measure the generation of hornification which is a non-reversible process that reduces bonding strength. Besides morphological changes, also the effect of the humidity on the bonding strength is a very important issue. Additionally, visco-elastic properties as a function of the humidity can be investigated under a controlled environment [94].

According to fiber-fiber bond cross-sections, new kind of scanning techniques with high lateral and also chemical resolution - such as Tip-enhanced Raman Spectroscopy (TERS) [95] - should reveal new insights into the fiber-fiber bond region. Here, the combination of chemical and morphological information on the nanometer scale should provide information of the material inside the gap between the two bonded fibers. Also, the TERS technique is a tool to investigate strain inside the fiber following Raman shifts. For instance, Eichhorn et al. showed that in coherent Raman spectra, the peak region around 1095 $cm^{-1}$ corresponds to the ring stretching modes of the cellulose structure [96]. They found that the shift rate is proportional to the modulus of the fiber and the applied stress. This could be used to map local fiber stress, for instance in pit regions, and to follow their changes during external loading.

# List of Figures

# List of Tables

# Acknowledgments

First of all I would like to thank my supervisor **Prof. Dr. Christian Teichert**, for advice, motivation and the trust in my person to develop new things.

**Prof. Dr. Friedemar Kuchar, Prof. Dr. Josef Oswald** and **Prof. Dr. Oskar Paris** for giving me the opportunity to write this thesis in the Institute of Physics at the Montanuniversität Leoben.

Furthermore, I have to thank all the members of the Institute of Physics for their support and friendship. Especially **Ing. Heinz Pirker** for his enthusiasm and support solving all kind of computer problems. **Peter Moharitsch** for crafting and improvement of the sample holders. **Heide Kirchberger** and **Magdalena Ottrin** for the help with bureaucracy stuff.

**Dr. Gregor Hlawacek** for his enthusiasm in open source software and fruitful discussions concerning all kind of problems. **Dr. Christian Hofer**, **Dr. Markus Kratzer**, **Dipl.-Phys. Igor Beinik**, **Dipl.-Ing. Stefan Lorbek**, **Dipl.-Ing. Quan Shen**, and **Dipl.-Ing. Andreas Pavitschitz** for a nice time at the institute with endless discussions. **Dr. Oleksandr Gluskho** for sharing an office room with me. **Dipl.-Ing. Nurdogan Gürkan** for the help with contact angle measurements. **Oliver Miskovic** and **Christian Ganser** for their support with AFM measurements.

The next big “thank you” is for the collaboration partners within the CD-Laboratory. Especially the head of the CD-Laboratory **Prof. Dr. Robert Schennach** for his patience and encourage of my work. **Prof. Dr. Wolfgang Bauer**, **Dr. Ulrich Hirn** and **Dipl.-Ing. Eduard Gilli** for lots of encouraging discussions in the meetings. **Dr. Lisbeth Kappel**, and **Dipl.-Ing. Wolfgang Fischer** for fruitful discussions and preparation of embedded samples as well as fiber-fiber bonds. **Barbara Hummer** for preparing fiber-fiber bonds. **Ing. Hartmut Schröttner**, FELMI for performing the ESEM images. **Leo Arpa** and **Walter Rüf**, Mondi Frantschach for their support from the industrial cooperation partner and the opportunity to work within this nice framework. **Esther Schennach** for reminding me of things I forgot to submit in case of financial things. **Prof. DDr. Isabella Pali** for last minute corrections.

The financial support by **Mondi** and the **Federal Ministry of Economy, Family and Youth and the National Foundation for Research, Technology and Development** is gratefully acknowledged.

The open source community for programs like Gwyddion, Qtiplot, and Octave.

Finally, I like to thank all my friends in Leoben that made Leoben a second home for me.

# Bibliography

[1] Schmied, F. J. Master's thesis, Montanuniversität Leoben, (2008).

[2] Rowell, R. *Handbook of wood chemistry and wood composites.* CRC Press Boca Raton, FL, (2005).

[3] Baker, A., Helbert, W., Sugiyama, J., and Miles, M. *Journal of Structural Biology* **119**, 129–138 (1997).

[4] Wikipedia. www.wikipedia.de, January (2011).

[5] Fratzl, P. *Current Opinion in Colloid & Interface Science* **8**, 32–39 (2003).

[6] Niskanen, K. and Yhdistys, S. *Paper physics.* Fapet Oy, Helsinki, (1998).

[7] Campbell, W. *Tappi* **42**, 999–1001 (1959).

[8] Nanko, H. and Ohsawa, J. In *Fundamentals of Papermaking: Transactions of the Ninth Fundamental Research Symposium held at Cambridge*, 783. Published by Mechanical Engineering Publications Limited, (1989).

[9] Lindström, T., Wågberg, L., and Larsson, T. *Advances in Paper Science and Technology* **1**, 457–562 (2005).

[10] Stratton, R. and Colson, N. *Materials Research Society Symposium Proceedings* **197**, 173–181 (1990).

[11] Mayhood Jr, C., Kallmes, O., and Cauley, M. *Tappi* **45**, 69–73 (1962).

[12] Torgnysdotter, A. and Wågberg, L. *Nordic Pulp & Paper Research Journal* **21**, 411–418 (2006).

[13] Forsström, J. and Torgnysdotter, A. *Nordic Pulp & Paper Research Journal* **20**, 186–191 (2005).

[14] Schniewind, A., Nemeth, L., and Brink, D. *Tappi* **47**, 244–248 (1964).

[15] Suresh, S. *Fatigue of materials.* University Press, Cambridge, (1998).

[16] wikipedia. http://en.wikipedia.org/wiki/File:Fourdrinier.svg, February (2011).

[17] Levlin, J., Söderjhelm, L., and Yhdistys, S. *Pulp and Paper Testing.* Fapet Oy, Helsinki, (1999).

[18] Kyrklund, B. and Strandell, G. *Paperi Ja Puu* **49**, 99–106 (1967).

[19] International Organization for Standardization. Geneva. *ISO 302:2004* (1981).

[20] Tasman, J. and Berzins, V. *Tappi* **40**, 699–704 (1957).

[21] Koljonen, K., Österberg, M., Johansson, L. S., and Stenius, P. *Colloids and Surfaces A: Physicochemical and Engineering Aspects* **228**, 143–158 (2003).

[22] Gustafsson, J., Ciovica, L., and Peltonen, J. *Polymer* **44**, 661–670 (2003).

[23] Fardim, P., Gustafsson, J., von Schoultz, S., Peltonen, J., and Holmbom, B. *Colloids and Surfaces A: Physicochemical and Engineering Aspects* **255**, 91–103 (2005).

[24] Xu, Y., Li, K., and Zhang, M. *Colloids and Surfaces A: Physicochemical and Engineering Aspects* **301**, 255–263 (2007).

[25] Piantanida, G., Bicchieri, M., and Coluzza, C. *Polymer* **46**, 12313–12321 (2005).

[26] Poggi, M., Mancosky, D., Bottomley, L., and Lucia, L. *Journal of Microscopy* **220**, 77 (2005).

[27] Simola-Gustafsson, J., Hortling, B., and Peltonen, J. *Colloid & Polymer Science* **279**, 221–231 (2001).

[28] Gindl, W., Reifferscheid, M., Adusumalli, R., Weber, H., Röder, T., Sixta, H., and Schöberl, T. *Polymer* **49**, 792–799 (2008).

[29] Wimmer, R., Lucas, B., Oliver, W., and Tsui, T. *Wood Science and Technology* **31**, 131–141 (1997).

[30] Page, D., El-Hosseiny, F., Winkler, K., and Lancaster, A. *Tappi* **60**, 114–117 (1977).

[31] Gindl, W., Konnerth, J., and Schöberl, T. *Cellulose* **13**, 1–7 (2006).

[32] Gindl, W., Gupta, H., Schöberl, T., Lichtenegger, H., and Fratzl, P. *Applied Physics A: Materials Science & Processing* **79**, 2069–2073 (2004).

[33] Burgert, I., Frühmann, K., Keckes, J., Fratzl, P., and Stanzl-Tschegg, S. *Holzforschung* **57**, 661–664 (2003).

[34] Salmen, L. *Comptes Rendus Biologies* **327**, 873–880 (2004).

[35] Forsström, J., Torgnysdotter, A., and Wågberg, L. *Nordic Pulp & Paper Research Journal* **20**, 186–191 (2005).

[36] Salvetat, J., Bonard, J., Thomson, N., Kulik, A., Forro, L., Benoit, W., and Zuppiroli, L. *Applied Physics A: Materials Science & Processing* **69**, 255–260 (1999).

[37] Demczyk, B., Wang, Y., Cumings, J., Hetman, M., Han, W., Zettl, A., and Ritchie, R. *Materials Science and Engineering A* **334**, 173–178 (2002).

[38] Yu, M., Files, B., Arepalli, S., and Ruoff, R. *Physical Review Letters* **84**, 5552–5555 (2000).

[39] Wang, Z. and Song, J. *Science* **312**, 242 (2006).

[40] Tan, E. and Lim, C. *Composites Science and Technology* **66**, 1102–1111 (2006).

[41] van der Rijt, J., van der Werf, K., Bennink, M., Dijkstra, P., Feijen, J., et al. *Macromolecular Bioscience* **6**, 697–702 (2006).

[42] Cheng, Q. and Wang, S. *Composites Part A: Applied Science and Manufacturing* **39**, 1838–1843 (2008).

[43] Kappel, L., Hirn, U., Bauer, W., and Schennach, R. *Nordic Pulp & Paper Research Journal* **24**, 199–205 (2009).

[44] Leica Microsystems. www.leica-microsystems.com, February (2011).

[45] Diatome Ltd. www.diatome.ch, February (2011).

[46] Binnig, G., Rohrer, H., Gerber, C., and Weibel, E. *Physical Review Letters* **49**, 57–61 (1982).

[47] Binnig, G., Quate, C., and Gerber, C. *Physical Review Letters* **56**, 930–933 (1986).

[48] Mironov, V. *Fundamentals of Scanning Probe Microscopy.* The Russian Academy of Sciences Institute for Physics of Microstructures, Nizhniy Novgorod, (2004).

[49] Magonov, S., Elings, V., and Whangbo, M. *Surface Science* **375**, 385–391 (1997).

[50] Whangbo, M., Bar, G., and Brandsch, R. *Applied Physics A: Materials Science & Processing* **66**, 1267–1270 (1998).

[51] Bar, G., Thomann, Y., Brandsch, R., Cantow, H.-J., and Whangbo, M.-H. *Langmuir* **13**, 3807–3812 (1997).

[52] Martinez, N., Patil, S., Lozano, J., and Garcia, R. *Applied Physics Letters* **89**, 153115 (2006).

[53] Rodrıguez, T. *Applied Physics Letters* **84**, 449–451 (2004).

[54] Proksch, R. *Applied Physics Letters* **89**, 113–121 (2006).

[55] Asylum Research. http://www.asylumresearch.com, January (2011).

[56] Nonnenmacher, M., Oboyle, M., and Wickramasinghe, H. *Applied Physics Letters* **58**, 2921–2923 (1991).

[57] Beinik, I., Galiana, B., Kratzer, M., Teichert, C., Rey-Stolle, I., Algora, C., and Tejedor, P. *Journal of Vacuum Science & Technology B: Microelectronics and Nanometer Structures* **28**, C5G5 (2010).

[58] Sader, J., Chon, J., and Mulvaney, P. *Review of Scientific Instruments* **70**, 3967–3969 (1999).

[59] DScaler. http://deinterlace.sourceforge.net/, Jan. (2011).

[60] Chandler, H. *Hardness testing.* Asm Intl, (1999).

[61] Oliver, W. and Pharr, G. *Journal of materials research* **7**, 1564–1583 (1992).

[62] Hertz, H., Jones, W., Jones, D., Wheeler, B., and Schott, G. *Macmillan* (1896).

[63] Nanoandmore. http://nanoandmore.com/, Jan (2011).

[64] Thornley, R. *New applications of the scanning electron microscope.* Cambridge, (1960).

[65] Danilatos, G. *Advances in Electronics and Electron Physics* **71**, 109–250 (1988).

[66] Alicona. http://www.alicona.com/home/products/Mex/MeX.en.php, February (2011).

[67] Alicona. http://www2.alicona.com/home/products/InfiniteFocus/InfiniteFocus.en.php, February (2011).

[68] Persson, B. *Sliding friction: Physical Principles and Applications.* Springer Verlag, Berlin Heidelberg, (1998).

[69] Gwyddion. www.gwyddion.net, (2011).

[70] Wenzel, R. *Industrial & Engineering Chemistry* **28**, 988–994 (1936).

[71] Klapetek, P., Necas, D., and Anderson, C. *Gwyddion user guide* (2011).

[72] Teichert, C. *Physics Reports* **365**, 335–432 (2002).

[73] Gonzalez, R. and Woods, R. *Digital image processing.* Pearson International Edition, (2008).

[74] The GIMP Team. http://www.gimp.org/, (2011).

[75] Octave. http://www.gnu.org/software/octave/, January (2011).

[76] Grace Team. http://plasma-gate.weizmann.ac.il/Grace/doc/UsersGuide.html, January (2011).

[77] Newman, R. *Cellulose* **11**, 45–52 (2004).

[78] Fernandes Diniz, J., Gil, M., and Castro, J. *Wood Science and Technology* **37**, 489–494 (2004).

[79] Niemi, H., Paulapuro, H., and Mahlberg, R. *Paperi Ja Puu* **84**, 389–406 (2002).

[80] Uehara, K. and Hogetsu, T. *Protoplasma* **172**, 145–153 (1993).

[81] Kappel, L., Hirn, U., Gilli, E., Bauer, W., and Schennach, R. *Nordic Pulp & Paper Research Journal* **25**, 71–75 (2010).

[82] Swanson, J. and Steber, A. *Tappi* **42**, 986–994 (1959).

[83] Haselton, W. *Tappi* **38**, 716–723 (1955).

[84] Kappel, L. *Development and application of a method for Fiber-fiber bonded area measurement.* PhD thesis, Graz University of Technology, (2010).

[85] Cowan, W. *Tappi* **78**, 101–101 (1995).

[86] Torgnysdotter, A., Kulachenko, A., Gradin, P., and Wågberg, L. *Journal of Composite Materials* **41**, 1619 (2007).

[87] Bos, J. H., Veenstra, P., Verhoeven, H., and de Vos, P. D. *Das Papierbuch - Handbuch der Papierherstellung.* ECA Pulp & Paper, Houten, NL, (1999).

[88] Adusumalli, R., Mook, W., Passas, R., Schwaller, P., and Michler, J. *Journal of Materials Science* **45**, 2558–2563 (2010).

[89] Beitz, W. and Grote, K. *Dubbel Taschenbuch für den Maschinenbau, 20 Auflage.* Springer Verlag, Berlin, (2001).

[90] Anderson, T. *Fracture Mechanics: Fundamentals and Applications.* CRC Press Boca Raton, FL, (2005).

[91] Ishikawa, K., Okuda, H., and Kobayashi, Y. *Journal of Materials Science Letters* **17**, 423–424 (1998).

[92] Schennach et al. *, in preparation* (2011).

[93] Stratton, R. *International Paper Physics Conference* **381**, 1–16 (1991).

[94] Habeger, C., Coffin, D., and Hojjatie, B. *Journal of Polymer Science Part B: Polymer Physics* **39**, 2048–2062 (2001).

[95] Deckert, V. *Journal of Raman Spectroscopy* **40**, 1336–1337 (2009).

[96] Eichhorn, S., Baillie, C., Zafeiropoulos, N., Mwaikambo, L., Ansell, M., Dufresne, A., Entwistle, K., Herrera-Franco, P., Escamilla, G., Groom, L., et al. *Journal of Materials Science* **36**, 2107–2131 (2001).